UNIVERSITY OF BELGRADE

FACULTY OF MECHANICAL ENGINEERING

Mahdi M. A. Algool

INITIAL PLASTIC DEFORMATION AND RESIDUAL STRESS INFLUENCING THE WELDING JOINT BEHAVIOR IN THE PRESENCE OF CRACKS

Doctoral Dissertation

Belgrade, 2015

UNIVERZITET U BEOGRADU
MAŠINSKI FAKULTET

Mahdi M.A. Algool

Утицај иницијалне пластичне деформације и заосталих напона на понашање завареног споја у присуству прслине

doktorska disertacija

Beograd, 2015

Dedicated to my wife, parents and teachers

MENTOR:

DR. Aleksander Sedmak, full professor

University of Belgrade, Faculty of Mechanical Engineering

MEMBERS OF COMMISSION:

Dr. Zoran Radaković; associate professor

University of Belgrade,Faculty of mechanical engineering

Dr. Taško Maneski; full professor

University of Belgrade, Faculty of mechanical engineering

Dr.Nenad Gubeljak, full professor
University of Maribor, Slovenia

Dr. Aleksandar Petrović; associate professor

University of Belgrade,Faculty of mechanical engineering

Acknowledgement

I would like to express my special appreciation and thanks to my advisor professor **Dr. Aleksandar Sedmak**, you have been a tremendous mentor for me, I would like to thank you for encouraging my research and for allowing me to grow as a research scientist. Your advice on both research as well as on my career have been priceless.

A special thank is given to the staffs of Mechanical Engineering faculty. I appreciate their help and their kindness.

Abstract

The full-scale model of penstock was produced using weldable high strength low alloyed steel (HSLA) Sumiten 80P (SM 80P). Steel SM 80P belongs to HT80 steel with tensile strength above 800 MPa and yield strength above 700MPa. Tensile properties were achieved by quenching and tempered technology which requires strong obeying of welding procedures. Finite element analysis has been carried out by using ABAQUS software to simulate the hydrostatic test of the full-scale model of penstock. A finite element model of penstock is a little bit different than the experimental test model in welding the shape and geometry (the third segment of the cylindrical mental of the experimental model has been neglected for the finite element model). In the first portion of the analysis the von Misses stress distribution will be investigated in two steps, the first load-unload and the second load-unload, and to focus on where the yielding initiates and spreads. For the second portion of the numerical study, the behavior of the model with initial residual stresses in weld joints have been analyzed for von Misses stresses distribution. The von Misses stress-strain relationship has been calculated in three ways: using linear elastic formulas, when the experimental model was treated as an ideal cylindrical vessel (without a 5º angle). The second relationship is obtained from strain guage measurements, and the third behavior is the stress-strain curve obtained from a numerical calculation (ABAQUS software). For the residual strength prediction and structural integrity assessment of penstock, a study of fracture mechanics behavior of an under-matched weld joints with small and large surface cracks for high strength low alloy steel of penstock structures has been performed by the J-R curve approach. Suminet 80P (SM 80P) grade steel plate was butt welded by submerged arc welding. Three tensile panels with surface cracks positioned in the base metal (BM), weld metal (WM) and the heat affected zone (HAZ) were tested at room temperature. And continuous measurement of force versus crack mouth opening displacement and crack extension was monitored during the test by the compliance method. In addition, J-R curves were built for three parts of the weld joint. Crack driving force is obtained for various values of applied stresses ratio and it plotted as a function of crack depth ratio.

Извод

Модел цевовода пуне размере је произведен од заварљивог нисколегираног челика високе чврстоће Sumiten 80P (SM 80P). Челик SM 80P припада групи HT80 челикакојиимајузатезну чврстоћу изнад 800 MPa и напон течења изнад 700 MPa. Затезне карактеристике су последица каљења и отпуштања, стога се приликом процеса заваривања мора испоштовати одговарајућа процедура. Уз помоћ софтева ABAQUS, методом коначних елемената на моделу је извршена симулација хидростатичког теста. Модел који је коришћен за прорачун методом коначних елемената разликује се од експерименталног модела у изгледу завареног шава и геметрије шава (трећи сегмент цилиндричног екпериментално модела је приликом прорачуна методом коналних елемената занемарен). У првом делу анализе промена вон Мизесових напона ће се испитати у два корака, први корак оптерећења-растерећења и други корак оптерећења-растерећења и фокус ће бити позиције почетка течења материјала и његова ширење. У другом делу нумеричког прорачуна анализирано је понашање модела у коме су генерисани иницијални заостали напони. Релација вон Мизесових напона и деформација је рачуната на три начина: линеарно-еластична анализа, када се модел третира као идеално цилиндрична посуда (без угла од 5º). Друга релација је добијена уз помоћ експерименталног мерења деформација и треће, понашање напон-деформација криве добијене нумеричким прорачуном (ABAQUS софтвер).За претпоставке процене преосталог века и проценеинтегритета конструкције, коришћена је студија механике лома испитивањем J-R криве метала шава ниже чврстоће са малом и великом прслином за нисколегиране челике високе чврстоће. ЕПП поступак је коришћен за чеоно заваривањеSuminet 80P (SM 80P)плоче. Контруално мерење силе и уста отварања као и ширење прслине је посматрано током теста одговарајућим методама. Поред тога, J-R криве су добијене за три различите позиције завареног споја. Сила раста прслине је добијена за различите вредности употребљеног напона и графички је представљен у функцији дубине прслине.

CONTENTS

List of figures

List of tables

Nomenclature

σ_H	Hoop (circumferential) stress
σ_L	Axial (longitudinal) stress
U	Strain energy per unit volume
S	Surface energy
W	Total energy
σ_f	Fracture stress
r_y , r_P	plastic zone size
σ_{ys}	Yield strength
E	Young's modulus
a	Crack length
v	Poisson's ratio
w	Strain energy density
$\mathrm{T_i}$	Components of the traction vector
u_i	Displacement vector components
d_s	Length increment along the contour Γ
Ψ	Strain energy density
Π	Total potential energy

p^v	Body force vector
p^s	Surface force vector
σ_{ij}	Deviatoric stress components
σ	Effective stress
w_p	Plastic work
$d\varepsilon_{ij}^{\ e}$	Elastic component of strain
$d\varepsilon_{ij}^{\ p}$	Plastic component of strain
ε_P	Effective plastic strain
Q	Plastic potential
E_T	Elastic plastic tangent modulus
K	Stress intensity factor
J_{el}	Elastic component of J integral
J_{pl}	Plastic component of J integral

1. INTRODUCTION

Pressure vessels commonly have the form of cylinders, spheres, ellipsoids, or some combination of these. In practice, vessels are usually composed of a pressure-containing shell together with flange rings and fastening devices for connecting and securing mating parts. Their main purpose is to contain a media under pressure and temperature to ensure safe and long life.

The most critical part of a pressure vessel is welded joint, because crack-like defects are inevitable, as stated by [1]. This is also evident from many failures, as illustrated by two examples below.

As the first example, leakage of large spherical tank, used for storage of ammonia, presented in Fig. 1-1, is briefly presented. It was caused by presence of undetected micro-cracks in welded joint, some of which have grown through the thickness during proof testing, as shown in Fig. 1-2, [2].

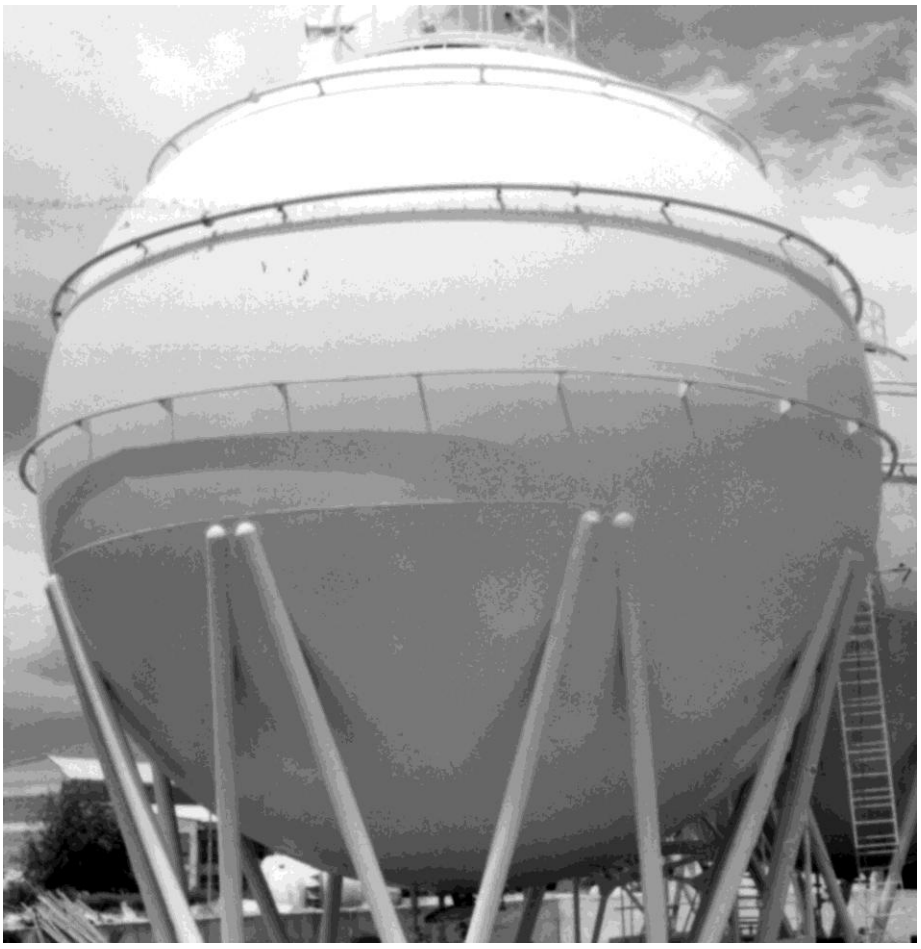

Figure 1-1. Spherical pressure vessel for ammonia, [2]

Figure 1-2. Macro-cracks in HAZ in NIOVAL 47 steel welded joint, [2]

Figure 1-2 shows micro-cracks in the storage tank for liquid carbon dioxide (CO_2), i.e. a vertical, cylindrical, thermally insulated pressure vessel, produced of high strength microalloyed steel, trade mark NIOVAL 47 (Steelworks Jesenice), [2, 3]. Two new connections at the upper lid had been requested in service operation to connect the outer freon unit to the inner built-in heat exchanger. Since no tubes of this steel are available, the storage tank manufacturer applied tubes and flanges of austenitic steel (X7CrNiNb18.10). The gas phase is cooled by the exchanger, located in the upper tank with new connections built-in in the upper lid. The austenitic steel was also used for two new connections, 26.9 mm in diameter, 2.6 mm wall thickness. It was difficult to achieve welded joint quality with so large difference in thicknesses. Therefore, reinforcements of similar thicknesses were welded to the lid, using rutile electrode, alloyed with 29% Cr and 9% Ni, and then the connecting tubes were welded to the reinforcement. Anyhow, due to metallurgical problems with dissimilar base metals, micro-cracking appeared in HAZ, as shown in Fig. 1-3, leading to the leakage of this pressure vessel.

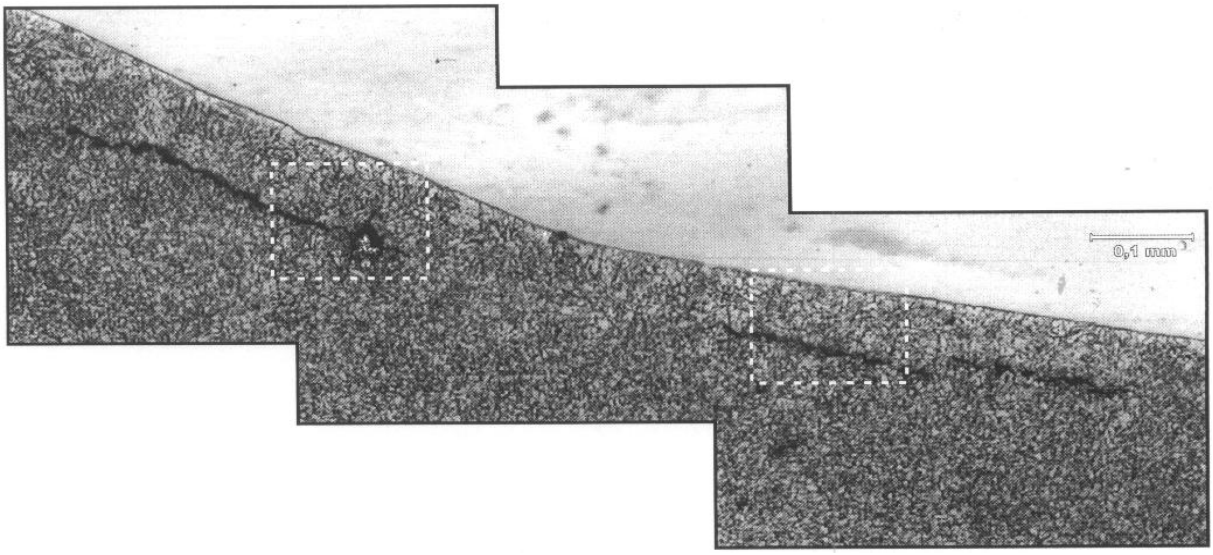

Figure 1-3. Micro-cracks in HAZ in NIOVAL 47 steel welded joint, [2]

Having in mind the complexity of presented problem, the basic aim of this paper is to present different aspects of pressure vessel safety in the scope of industrial safety, focused to the chemical industry.

1-1.QUALITY ASSURANCE - PED 97/23

In order to avoid failure of pressure equipment the defects and heterogeneities have to be under strict control and inspection, especially welded joints, [2]. The first approach is quality assurance system, including many codes and rules defined for that purpose, like Pressure Equipment Directive (PED 97/23/EC), [4-5], but applicable only to new products. The second approach is structural integrity assessment, applicable also in the case of damaged pressure equipment, when the decision of its further exploitation is possible under given condition only after detailed consideration. Finally, risk based approach comprising inspection, maintenance and control, is yet another aspect of this problem, [6-7].

The operational safety of welded pressure vessels primarily depends on weldments behavior. The approach, accepted in standards for weldment design, is to define the acceptable defect size. All efforts in material production and improvements in welding and non-destructive testing techniques, together with strict requirements in quality assurance, can not exclude the appearance of crack-like defects during fabrication, stress relieving, hydrostatic proof tests or operational service. Furthermore, in real welded pressure vessels stress concentrations caused by geometrical changes (including weldment imperfections, such as angular distortion or misalignment) can produce local plastic strains, possibly exhausting a portion of the strain hardening capacity. In these circumstances the question arises of how cracks will behave.

Full scale tests of welded pressurized equipment are known as the most informative when its safety is considered. In some cases they are inevitable despite their high cost because they can give realistic answers relating to the service behavior of welded joints. Hydrostatic pressure proof test can be classified as full scale test.

Directives for technical standards for stationary pressure vessels prescribed that the regular periodic proof pressure test of vessels should be performed before six years in service, if not otherwise required by the regulations on the technical standards for certain type of pressure vessels and stored substances.

Hydrostatic pressure for proof test is often calculated using the formula: $p_i = 1.3\ p_r$, where p_i is proof test and p_r is the design pressure. The logic behind this approach is that once a pressure vessel has withstood proof test, it will be safe in the exploitation under design pressure. Nevertheless, experience indicates more complex situation, as was the case with number of large pressure vessels, used in chemical industry (CO_2 or ammonia storage). As an example, already mention here, the proof test of the spherical storage tanks has provoked cracking and leakage, [2].

1-2.PROCEDURES FOR STRUCTURAL INTEGRITY ASSESSMENT

In-service behavior of many structural components revealed that cracks lead to the fatal failure. One possibility to prevent such a scenario is to use quality assurance system. However, it can not cover all situations in which pressure equipment can operate, and this system is not applicable completely for pressure equipment in operation. Problem might be solved by applying fitness-for-purpose approach and fracture mechanics analysis for a cracked component, in the scope of its structural integrity assessment.

This approach was first used in Alaska pipeline in U.S.A. After final NDI before pipeline introduction in exploitation a great number of shallow cracks had been detected, not acceptable according to standards. The repair of defective pipeline would have been too expensive, so additional investigation has been performed by the National Institute of Standards and Technology (NIST) to assess cracks significance by fracture mechanics approach. It was found that less than 5% of detected cracks had to be repaired according to structural integrity approach, and 95% of them were accepted without affecting structural integrity and in-service safety, [8]. The second case is typical for older equipment. Non-acceptable crack-like defects have been detected in pressure vessels after almost 30 years of service, [1]. It was unexpected, since during service life vessels were under strict inspection, including proof tests with pressure 50% higher than the design pressure, indicating no defects. Crack-like defects detection was attributed to the application of new NDT device with higher sensitivity. Fracture mechanics analysis, clearly demonstrated that crack-like defects, treated in conservative way regarding shape and size, could not jeopardize structural integrity of these vessels. So, the inspection authority and owner accepted to continue the exploitation of vessels with reduced inspection period, [9].

The practical application of fracture mechanics is from the very beginning based on twofold interpretation of its parameters: they represent loading and structural geometry, including a crack, on one hand side, whereas their critical values represent material properties and crack resistance, on the other hand side. Engineering practice had been changed adopting fracture mechanics criteria instead of traditional and rigorous standards on admissible defects regarding necessity of repair. This enabled acceptance of fracture mechanics analysis as a sound base for allowable exclusions from existing standards under certain circumstances, i.e. if such analysis results in justified and conservative (safe) assessment of the integrity of a structure.

Fracture mechanics has connected three variables (stress, defect dimensions, and fracture toughness), as shown in Fig. 1-4, enabling evaluation of the third value, based on two known variables. Based on this, several procedures were developed in order to assess structural integrity. Here, the comparison of material crack resistance (expressed by J integral in experimentally obtained J-R curve) and Crack Driving Force (CDF), obtained by analytical or numerical model, will be used.

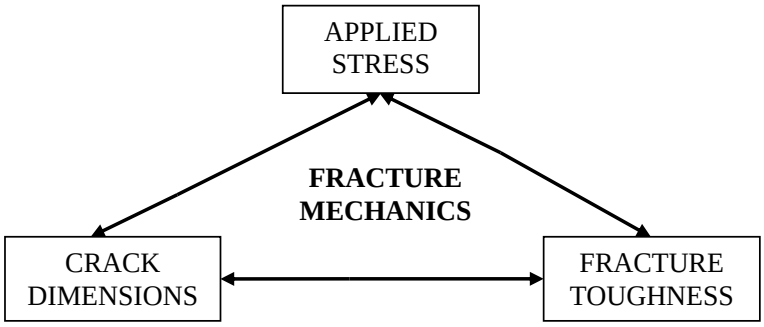

Figure 1-4. Fracture Mechanics triangle

1-3.The application of J integral to crack growth analysis

It is possible to establish criterion for fracture prediction, applying crack growth resistance curve, expressed by J-R curve, and CDFs, as shown in Fig. 1-5 for five different levels of load (stress). The simple explanation of this approach is that crack of length a_0 will grow in stable manner under certain load, in the case presented in Fig. 1-5 it is stress σ_4, until it reaches its critical value (point A), i.e. length $a_0+\Delta a$, when the growth will become unstable, leading to the fracture of a component. It is very important to understand fully such a behavior and eventual consequences of stable to unstable crack growth for the safe exploitation of a pressure vessel.

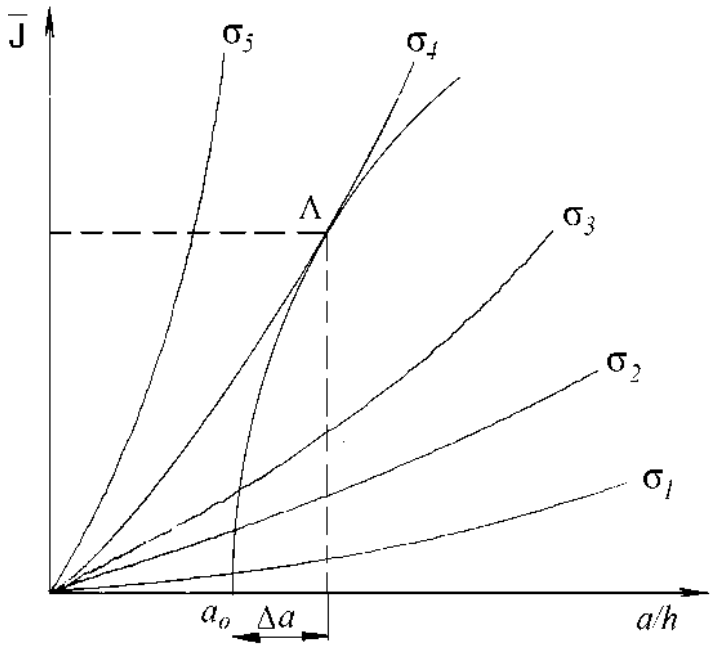

Figure 1-5. Procedure for fracture prediction based on crack resistance J-R curve

1-4.RISK BASED APPROACH

The Extensive European project RIMAP, from 2001 until 2004, was introduced to offer a European standard for risk based management (RBM), [7]. It has produced four industry specific workbooks (petrochemical, chemical, steel and power generation industries), aimed to provide more specific guidance on how to apply the RIMAP approach in these sectors. However, this approach is to complex, and will not be considered here. Instead, we present here only the risk matrix approach, as illustrated in Tab. 1-1. This approach uses well-known definition of risk being the product of the probability and the consequence, [7].

Table 1-1. Scheme for risk-based qualitative evaluation of maintenance

		Consequence category				
		A	B	C	D	E
Probability category	5					Very high
	4				High	risk
	3			Medium	risk	
	2		Low risk	risk		
	1	Very low risk				

In the matrix shown in Tab. 1-1, consequences are categorized, based on several parameters (health, safety, environment, business, security) as A to E; A indicates low, almost negligible consequences, and E refers to fatal and serious consequences. Probability categories are graduated 1 to 5, category 1 representing a very unlikely detrimental event, once in over a 100 years (1×10^{-4}), and category 5 representing a very probable event occurring at least once in a year (1×10^{-1}).

It is self-evident that consequences of failure of pressure vessels used in chemical industry can be extremely serious, even catastrophic, as in the case of Bopal disaster, indicating category E, as the rule. For safe and reliable use of pressure vessel in chemical industry it is of utmost importance to assure extremely low frequency of such events, classified as probability category 1, since only in this case risk is not bigger than medium. This can be achieved by special measures in all steps of design, construction and operation, including structural integrity assessment. The application of risk matrix is illustrated and explained in more details in [7].

It is also interesting to note that pressure vessels are treated in somewhat similar way by PED 97/23, since they have to be categorized from 0 to 4, according to p·V value (p stands for pressure, V for volume). Although this looks like risk-based approach, one should notice that consequence and probability can not be separated in this approach, making it one-dimensional, or let say risk vector approach.

One should notice that the probability of event can be increased by water proof test, “pushing up” risk along the vertical axis of the risk matrix. Thus, this approach clearly, even graphically, indicates possible problems with water proof testing.

1-5.CASE STUDY - LEAKAGE OF CO_2 STORAGE TANK

As already mentioned in the introduction, during the water proof testing of storage tank for liquefied carbon dioxide droplets of water had been revealed on the outer wall of its manhole, [2, 3]. The storage tank is of cylindrical form, thermally insulated, 12.5 m^3 in volume. The mantle and tank lids are produced of high strength micro-alloyed steel, 14 mm in thickness. The lowest operating temperature of the tank is –55 °C, the highest operating pressure 30 bar, the proof pressure test 39 bar. The storage tank is classified as II class of pressure vessels, according to p·V criterion. A general view of tank and position of a manhole is presented in Fig. 1-6.

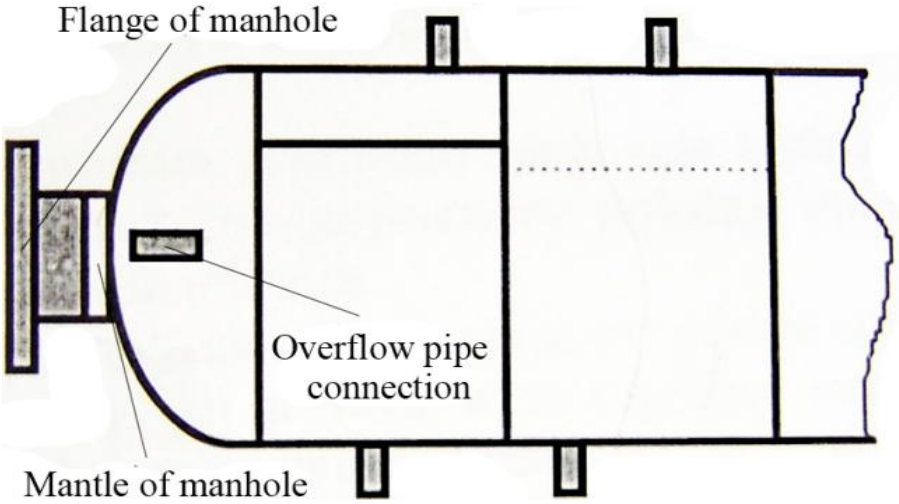

Figure 1-6. General view of tank for liquefied CO_2 storage with the position of the manhole

After removing the thermal insulation from the manhole, the moisture is located around the welded joint between the mantle and flange neck. The manhole consisted of mantle, produced of the same high strength micro-alloyed steel, 10 mm thick, and a flange casting of high alloyed austenitic steel X10CrNi18.10. The flange and the manhole are welded by shielded manual arc welding (SMAW), using high alloyed austenitic consumable INOX 29/9.

The welded joint between the flange and manhole mantle had been performed as a butt joint. Flange necking towards the welded joint ended by a cylindrical part of diameter and thickness that are equal to the diameter and thickness of the manhole mantle, of width 30 mm. The cracking network has been detected in this cylindrical part of the flange neck in a limited zone, with crack lengths typically between 25 and 27 mm. In the zone of individual cracks, only short cracks, 1 to 2 mm long, are detected.

After emptying the tank and opening the manhole, its inner side was tested. On the inner side two larger pores are found and also individual cracks, 1 to 2 mm in length. Figure 1-7 present the cross section through the centre of cylindrical part of flange neck, with the zone with the highest cracking density shown in Fig. 1-7a, and pores in Fig. 1-7b. A large number of cracks, approximately perpendicular to the flange surface, are visible. Testing by dye penetrants indicated a large number of cracks penetrating to different depths, some of them through the thickness.

Figure 1-7. Cross section views: a) network of cracks, b) pores on inner side

In Fig. 1- 7b the cross section close to the pores detected on the inner side of a manhole is presented. Two pores, which are in fact the continuation of pores detected on the inner side of the manhole, can be clearly recognised. Most intensive leakage on the outer side of the manhole is revealed just opposite of these pores, since they are followed by cracks, penetrating to the outer surface of the tank.

It is concluded that the detected cracks affect the safety operation of the tank, and hence retrofitting is required, unless the complete structural integrity assessment is performed, which has been done, as follows.

Standard ASTM E1820 was used, SEN(B) specimen had been tested as relationship *J* vs. crack opening displacement, CTOD, by unloading compliance method, at 20 °C and at -60 °C. The goal of testing was to define crack resistance curve (*J-R* curve), the relationship between *J* integral value and crack extension, Δa. From this curve it is possible to determine critical J_{Ic}, a measure of fracture toughness, convert it to plane strain fracture toughness K_{Ic} and verify crack significance in regard brittle fracture. The complete *J-R* curve is more useful, enabling the determination of stress level for initiation of stable crack growth.

For the same specimens *J-R* curves are presented in Fig. 1-8, and structural integrity assessment for cracked storage tank is shown in Fig. 1-9.

Obtained values of K_{Ic} show the effects of testing temperature on welded joint components. Highest K_{Ic} values belong to specimens notched in HAZ, that notched in WM have 50% lower values. This is not important for static loading, but can be critical at variable loading, and critical crack size a_c.

One can see from Fig. 1-9 (the critical point) that the crack can grow from 0.4x14 (5.76 mm) up to 7.7 mm in stable manner under the pressure 306 MPa (72% of Yield Strength), but once it has reached the critical value, the conditions for unstable crack growth, i.e. brittle fracture are fulfilled. One should notice that such a scenario is also possible in full-scale pressure vessel, especially if maximum stress approaches the Yield Stress, as it could be the case during water proof test. From Fig. 1-9, it is

clearly visible that stresses less than 72% of Yield Strength will not provoke unstable crack growth. Using this example, one can easily think of situation in which the design stress is safely below the critical one, let say 60% of Yield Strength, but 30% of additional water proof stress will not be, since it would reach 78% of Yield Strength.

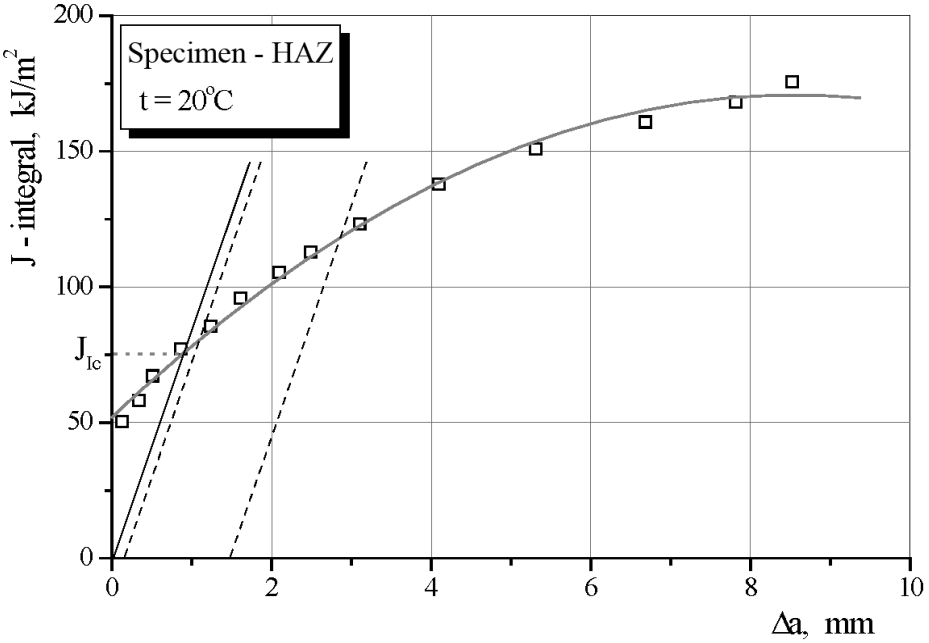

Figure 1-8. J-R curve and determined value of J_{Ic}, for specimen in HAZ

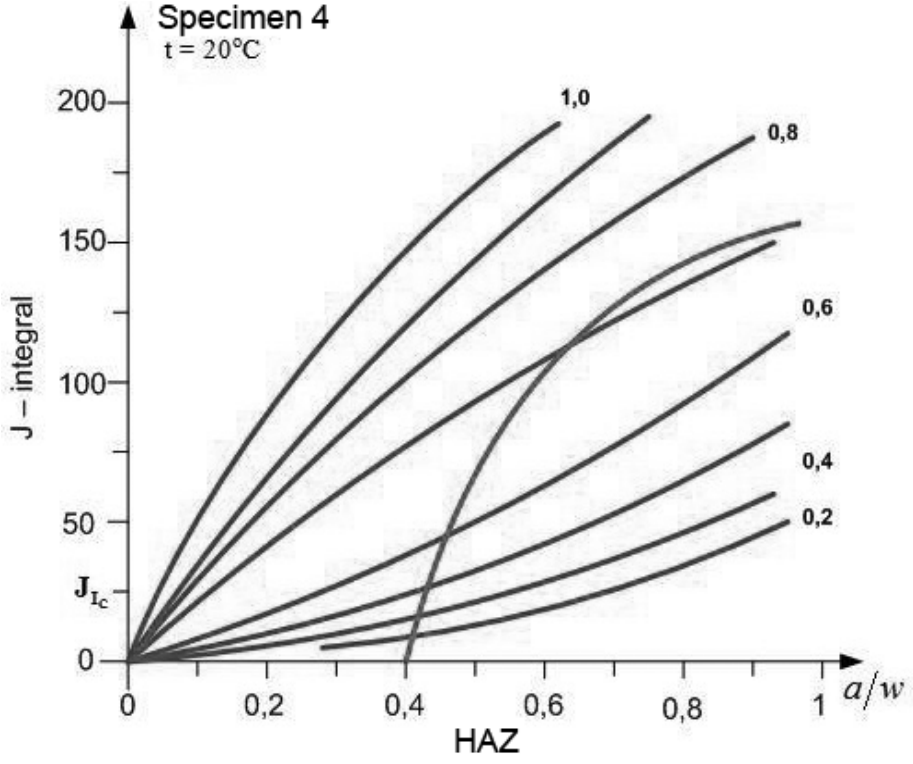

Figure 1-9. Structural integrity assessment for cracked components of storage tank

Having in mind problems described in the introduction, the aim of this thesis was to evaluate effects of initial plastic deformations and residual stresses on welded joint behaviour in presence of cracks.

2. INTRODUCTION TO PRESSURE VESSELS – LITERATURE OVERVIEW

Vessels, tanks, and pipelines that carry, store or receive fluids are called pressure vessels. The pressure vessel often has a combination of a high pressure together with high temperature, and in some cases flammable fluid or highly radioactive materials. The size and geometric form of pressure vessels vary greatly from large cylindrical vessels used for high-pressure gas storage to the small sized ones, used as hydraulic units for aircrafts.

It is important for a pressure vessel designer to understand the nature of loading that acting on the pressure vessel and the structural response to the loading. Generally the loads acting on a structure can be classified as:

- Sustained,
- Deformation controlled,
- Thermal.

Figure 2-1. Horizontal cylindrical pressure vessel in steel

These three loads types may be applied in a steady or cyclic manner. The structure under the action of these loads may respond in a number of ways, [10]:

- When the response is elastic, the structure is safe from collapse when the applied loading is steady. If the applied loading is cyclic a failure due to fatigue is possible, (high cycle fatigue).

- When the response is elastic in some regions and plastic in others, produced by sustained and deformation controlled loads, there is potential to have an unacceptably large deformation.

- Cyclic loads or cyclic temperature distribution can produce plastic deformation and cause fatigue failure (low cycle fatigue).

- Sustained loads in brittle materials or in ductile materials at low temperatures could result in fatigue failure (low cycle fatigue).

The failure that pressure vessel are to be designed against are generally stress dependent. For this reason it becomes necessary to obtain the stress distribution in pressure vessel.

Material of construction of pressure vessel most often used:

- Steels
- Non-ferrous materials such as aluminum and copper.
- Specially metals such as titanium and zirconium
- Non-metallic materials such as plastic composites and concrete.
- Metallic and non-metallic protective coating.

Mechanical properties that generally are of interest are:

- Yield strength.
- Ultimate strength.
- Reduction of area.
- Fracture toughness.
- Resistance to corrosion.

Two common pressure vessel geometries are cylindrical and spherical. The thickness of a vessel wall is often small compared to its diameter, the outward pressure of the contained gas or liquid is resisted by tensile strength in the walls of the pressure vessel.

2-1.Cylindrical pressure vessel

A thin-walled cylindrical vessel has outer radius R, wall thickness t, and contains pressure P. the walls of pressure vessel are subjected to a biaxial state of stresses figure 2-2.

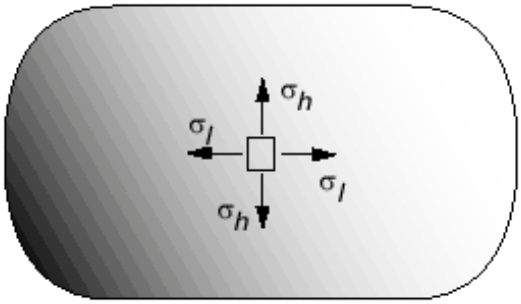

Figure 2-2. The biaxial state of stresses,(hoop stresses and axial stresses)

Hoop (Circumferential) stress:

The hoop stress σ_H is caused by the pressure acting to expand the circumference of the vessel. The hoop stress is calculated by taking a horizontal cut through the diametrical plane figure 2-3. The pressure force is counteracted by hoop stress in pressure vessel wall. The corresponding force F_W in the walls:

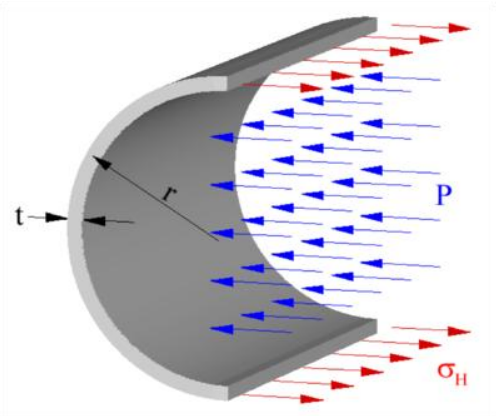

Figure 2-3. Determination of hoop stress, at the diametrical cut

$$F_{W=}\,\sigma_H[2tL] \tag{2-1}$$

Equating the two forces to satisfy equilibrium:

$$P\ 2\ R-t\ L\ =\sigma_H[2tL] \tag{2-2}$$

$$\sigma_H = \frac{PR}{t}\left[1 - \frac{t}{R}\right] \quad (2\text{-}3)$$

Since t is small compared to R the hoop stress:

$$\sigma_H = \frac{PR}{t} \quad (2\text{-}4)$$

Axial (Longitudinal) stress:

The longitudinal stress σ_l is caused by pressure acting against the cylinder end caps. The longitudinal stress is calculated by considering the forces on the cross-section of the cylinder figure 2-4:

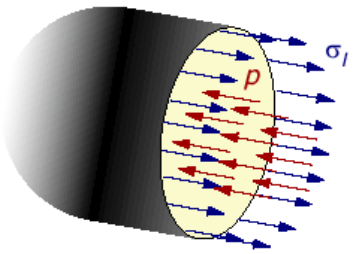

Figure 2-4. Determination of longitudinal stress at vertical cut

$$F_P = P\pi(R-t)^2 = P\pi R^2\left[1 - \frac{t}{R}\right]^2 \quad (2\text{-}5)$$

$$P\pi R^2\left[1 - \frac{t}{R}\right]^2 = \sigma_l 2\pi R t \quad (2\text{-}6)$$

$$\sigma_l = \frac{PR}{2t} \quad (2\text{-}7)$$

Hoop stress equal two times of axial stress in cylindrical pressure vessel.

2-2. Stress and strain distribution in elastic range

The ratio between the mantel thickness (t =47 mm) and inner diameter (d=4200 mm) is 0.01 so the model can be treated as a thin shelled pressure vessel with similar strain values on the inner and outer surface. Strain measurement on the outer surface is much easier than on the inner where strain gauges have to be properly protected against the pressure.

On the outer surface on the model for linear elastic behavior are the following valid formulas for stress and strains:

a) Stress

Hoop stress $\sigma_t = p\frac{2d^2}{D^2 - d^2}$

Axial stress $\sigma_z = p\frac{d^2}{D^2 - d^2}$ (2-8)

Radial stress $\sigma_r = 0$

Hoop strain $\varepsilon_t = \frac{1}{E}(\sigma_t - \nu\sigma_z)$, Axial strain $\varepsilon_z = \frac{1}{E}(\sigma_z - \nu\sigma_t)$ (2-9)

Radial strain $\varepsilon_r = \frac{1}{E}\nu(\sigma_t + \sigma_z)$

where D=4294 mm – outer diameter, d=4200 mm – inner diameter, E=210 GPa - modulus of elasticity, $\nu = 0.3$ - Poison ratio.

By replacement of upper values stress and strain values are dependent on inner pressure given as:

$$\sigma_t = 44.186\,p\,.\,\sigma_z = 22.093\,p\,,\sigma_r = 0\;\varepsilon_t = 178{,}85\cdot 10^{-12}\,p \quad (2\text{-}10)$$

All formulas are valid for isotropic material without taking into account the residual stresses, stress concentration, presence of welded joints, and deviation of ideal geometric shape.

According to Misses hypothesis ideal stress σ_i can be calculated as

$$\sigma_i = \sqrt{\frac{1}{2}\left[(\sigma_t - \sigma_r)^2 + (\sigma_r - \sigma_z)^2 + (\sigma_z - \sigma_t)^2\right]} \quad (2\text{-}11)$$

By replacing for $\sigma_r = 0$ final expression for ideal stress will be as

$$\sigma_i = \sqrt{\sigma_t^2 - \sigma_t\sigma_z + \sigma_z^2} = 38.266p \quad (2\text{-}12)$$

Ideal strain can be calculated according to the well-known expression as

$$\varepsilon_i = \frac{\sqrt{2}}{2(1+\nu)}\sqrt{(\varepsilon_t - \varepsilon_z)^2 + (\varepsilon_z - \varepsilon_r)^2 + (\varepsilon_r - \varepsilon_t)^2} = 182.22\text{p} \qquad (2\text{-}13)$$

Taking inner pressure *p* as a parameter into the expression (2-10) one can obtain the following relationships between stress and strain I hoop and axial direction

$$\sigma_t = 247.05 \cdot 10^9 \varepsilon_t ; \sigma_z = 525.02 \cdot 10^9 \varepsilon_z ; \sigma_i = 210 \cdot 10^9 \varepsilon_i \qquad (2\text{-}14)$$

By solving expressions (2-12) it is possible to calculate stresses in hoop and axial direction from measured strain gages strains ε_t and ε_z as

$$\sigma_t = \frac{E}{1-\nu^2}(\varepsilon_t + \nu\varepsilon_z)$$

$$\sigma_z = \frac{E}{1-\nu^2}(\varepsilon_z + \nu\varepsilon_t) \qquad (2\text{-}15)$$

which are valid for plain stress condition ($\sigma_r = 0$).

Using expressions (2-15) it is possible to calculate the stresses in hoop and axial direction for measured strains ε_t and ε_z. Ideal strain ε_i can be calculated after simplifying the expression (2-13) to:

$$\varepsilon_i = \frac{E}{1-\nu^2}\sqrt{(1-\nu+\nu^2)\cdot(\varepsilon_t^2 + \varepsilon_z^2) - (1-4\nu+\nu^2)\varepsilon_t\varepsilon_z} \qquad (2\text{-}16)$$

Using above equations it is possible to have the following stress – strain distributions: $\sigma_t - \varepsilon_t$; $\sigma_z - \varepsilon_z$ and $\sigma_i - \varepsilon_i$.

2-3. Stress and strain distribution in plastic range

During the hydrostatic model test there are on some places total strains for which the stresses will be out of linear elastic stress – strain distribution. For such cases we need the relationships taking into account the plastic deformation and strain hardening effect where the ideal stress can be expressed using the Romberg – Osgood as

$$\sigma_i = A\varepsilon_{ipl}^{n} \tag{2-17}$$

Where *A* and *n* are the strength and strain hardening coefficients obtained from uniaxial tensile tests of the tensile specimens representing the observed place usually the weld metal. Ramberg - Osgood coefficients for all welded joints on the penstock model are presented in Table (2-1).

Table 2-1. Romberg – Osgood coefficients for plastic deformation

Weld joint on the Penstock model	Weld designation	Strength coefficient A, MPa	Strain hardening, n
Longitudinal SAW	L-SAW	1217.2	0.076
Longitudinal MAW	L-MAW	1041.8	0.044
Circular SAW	C-SAW	1232	0.079
Circular MAW	C-MAW	1029.8	0.047

In order to use the equation (2-17), one needs to express the total ideal strain ε_i as the sum of elastic and plastic part as

$$\varepsilon_{i-total} = \varepsilon_{ielastic} + \varepsilon_{iplastic} \tag{2-18}$$

In order to simplify the procedure for cylindrical pressure vessel it is valid ratio

$$m = \frac{\sigma_z}{\sigma_t} = 0.5 \tag{2-19}$$

Expression (2-12) can be written in simple form using the parameter *m* as

$$\sigma_i = \sigma_t \sqrt{1 - m + m^2} \tag{2-20}$$

For plastic deformation Poisson's coefficient ($\nu = 0.5$), ideal plastic deformation can be expressed as:

$$\varepsilon_{iplastic} \cong \frac{\sigma_i}{E} = \frac{\sigma_t}{E}\sqrt{1 - m + m^2} \tag{2-21}$$

And hoop plastic strain is

$$\varepsilon_{tplastic} \cong \frac{1}{E}(\sigma_t - 0.5\sigma_z) = \frac{\sigma_t}{2E}(2-m) \tag{2-22}$$

Combining the expressions (2-19) and (2-20) it is possible to correlate the ideal plastic hoop strain and hoop plastic strain as

$$\varepsilon_{iplastic} = \frac{2}{2-m}\sqrt{1-m+m^2}\cdot\varepsilon_{tplastic} \tag{2-23}$$

Hoop plastic strain is

$$\varepsilon_{tplastic} = \varepsilon_{ttotal} - \varepsilon_{telastic} \tag{2-24}$$

At the end the equation (4-10) can be expressed as

$$\sigma_t = A\left(\frac{2}{2-m}\right)^n \left(\sqrt{1-m+m^2}\right)^{n-1} \varepsilon_{tplastic}^n \tag{2-25}$$

2-4. Experimental work of hydrostatic test of a full-scale model of penstock, [2]

2-4. Introduction

The application of High Strength Low Alloyed (HSLA) steels for production of pressure vessels is achieved by development of weld consumables (electrodes, wires and flax) with lower strength and higher plasticity compared with Base Metal (BM). The combination of such tensile properties is known as the under matching (UM) effect. Plastic deformations during the testing and exploitation procedures will be concentrated in Weld Metal (WM) leaving the BM with elastic deformations. The applied stress level, which will produce plastic deformations, is lower than the yield strength of BM. Welded joints are places with non-uniform stress distribution because of stress concentration and residual stresses introduced by the welding procedure. Simultaneously introducing different influencing factors will produce difficulties by stress calculation of welded joints. The calculation and design of pressure vessels have to take into account all influencing factors on stress distribution in order to achieve good use of materials and needed safety. On the produced pressure vessels there are possible deformation measure-

ments, using different techniques and needed for stress calculations and assessment of welded joints behavior under different service conditions.

The prototype, Fig. 2-5, was produced using weldable high strength low alloyed steel (HSLA) Sumiten 80P (SM 80P) produced in the Japanese steel factory Sumitomo. Steel SM 80P belongs to HT80 steel with tensile strength above 800 MPa and yield strength above 700MPa. Tensile properties were achieved by quenching and tempered technology which requires strong obeying of welding procedures. The MAW weldments were made using basic low hydrogen electrode LB118, and SAW by using core wire U8013 plus M38F flux, “Cobe Steel”, Japan. Certified welders were used to weld the prototype and later, the penstock. Trial samples for additional investigation were welded parallel with a prototype and were tested after hydraulic testing of the model.

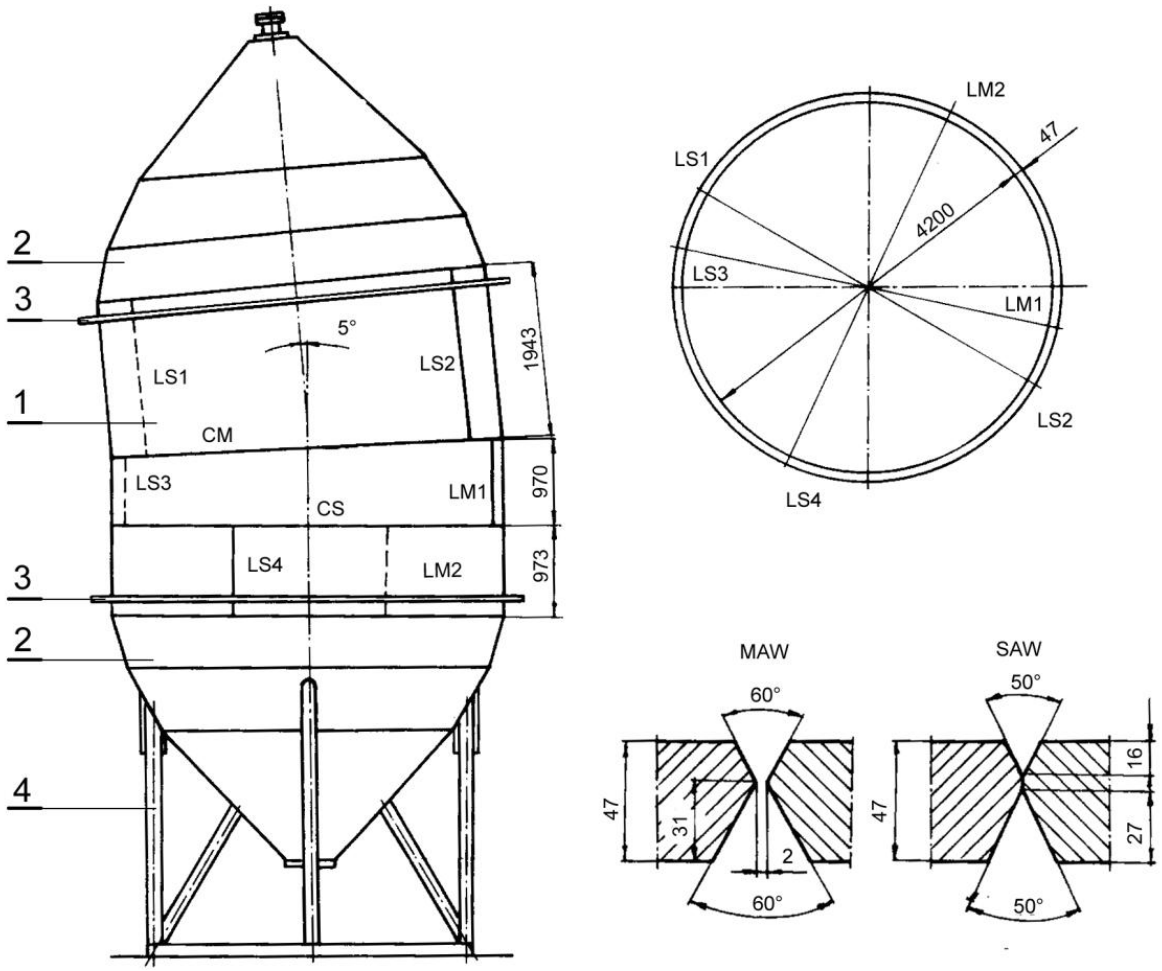

Figure 2-5. Design of penstock segment full-scale model: 1 - mantle; 2 - lid; 3 - stiffener; 4 - supports, L - Longitudinal, C - Circular; MAW – shielded manual arc welding (M); SAW - submerged arc welding, [2]

Typical chemical composition of SM 80P steel plates and its weld metals is presented in Table 2-2, and mechanical properties in Table 2-3.

Table 2-2. Chemical composition of SM 80Psteel and of MAW and SAW weld metals

Element		C	Si	Mn	P	S	Cu	Cr	Ni	Mo	V	Ceq
SM 80P		0.10	0.30	0.90	0.01	0.008	0.24	0.48	1.01	0.47	0.03	0.5
Weld metal	MAW	0.06	0.53	1.48	0.011	0.005	-	0.24	1.80	0.43	-	-
	SAW	0.07	0.37	1.87	0.01	0.011	-	0.44	0.13	0.73	-	-

Table 2-3. Mechanical properties of SM 80P steel and of MAW and SAW weld metals

Material	Direction	Tensile test			Charpy impact test	
		Y.S., MPa	U.T.S., MPa	Elongation, %	vE_{-40}, J	vT_{rs}, °C
SM 80P	rolling	755 - 794	804 - 834	24 - 29	156 - 224	-92
	cross rolling	755 - 794	795 - 834	22 – 23	60 - 147	-58
Weld metal	MAW	722	810	22	99	-5
	SAW	687	804	23	78	-18

Hydrostatic testing of the model was done in three stages as follows:

1. Checking of measuring system, increasing the inner pressure from 0 to 30 Bars
2. The first loading and unloading - Increasing the inner pressure from 0 to 92 Bars in order to produce the hoop stress into the mantel which corresponds to the service stress and unloading
3. The second loading and unloading Overloading of the model with 30% in correspondence with mantel service stress by increasing the inner pressure from 0 to 123 Bars.

Strain Gauges (SG) and Moiré grids measured the deformations of the model. On the outer side of the model 51 strain gauges with different characteristics were placed. Figure 4-7 presents the instrumentation on the developed model mantle with the scheme of cut samples for specimens planned for testing after the hydrostatic test.

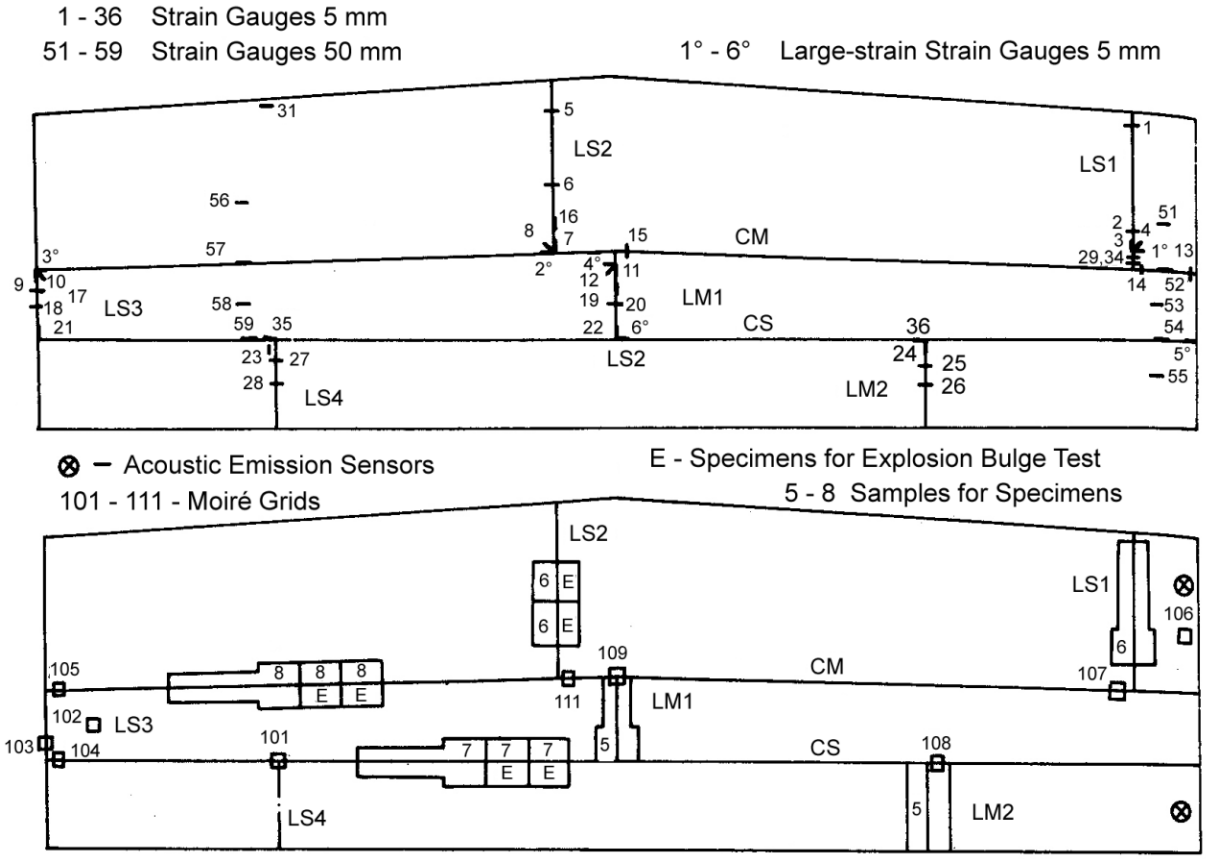

Figure 2-6. Instrumentation and specimens sampling in penstock model static pressure test

The most important sesults of these experiments are shown here, whereas the complete [2]. As already explained, pressurizing of the model had been performed in two stages. In the first stage the pressure reached 90.2 bar (σ_t =399 MPa), corresponding to working pressure, meanwhile model was held under pressure of 73.5 bar for two hours. After unloading, model was tested by the pressure of 120.6 bar (σ_t =533 MPa) in the second stage, that is close to the total working and water hammer load. For selected location and strain gauges, given in Fig. 2-6, the measures of developed strain are presented. The level b corresponds to maximum strain achieved in first pressure stage, and level a indicates residual strain after unloading; level d is maximum strain achieved in the second stage, and level c indicates total residual strains.

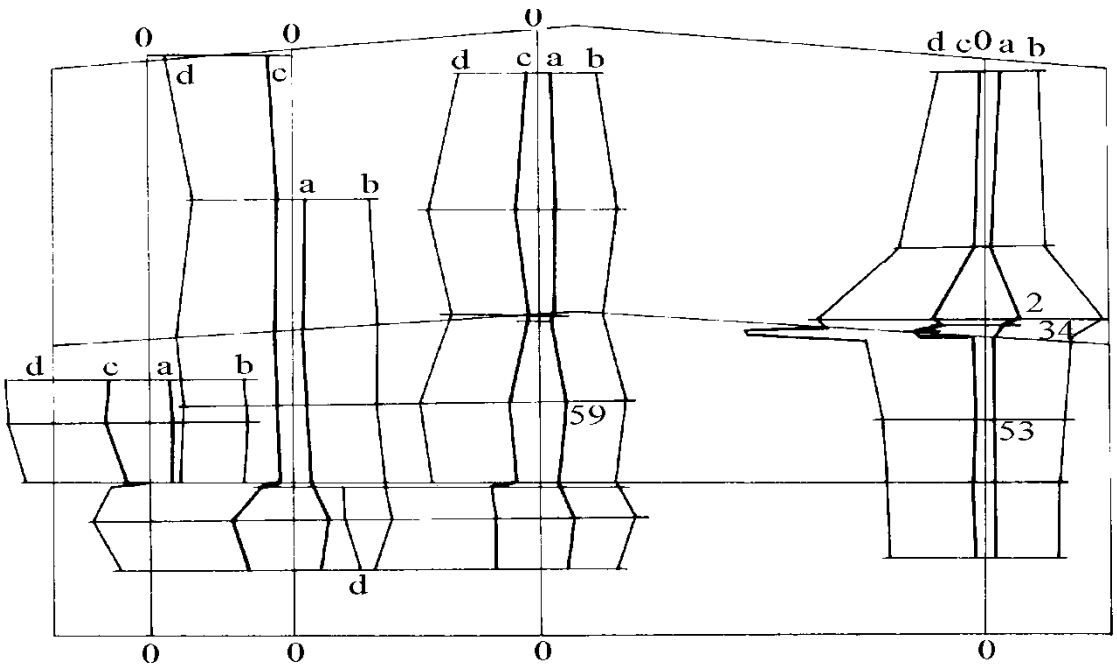

Figure 2-7. Distribution of strains in weldments after pressurizing

After hydro-pressure testing the specimens for mechanical tests were cut out of the mantle. The mechanical properties, tested for MAW and SAW, longitudinal and circular welded joints, with the corresponding trial sample weldments are given in Table 2-4.

Table 2-4. Results of tensile tests and hardness of welded joints

Welded joint	Specimen		Welded joint		Weld metal tensile properties			Hardness of welded joint HV		
			Y.S.	U.T.S	Y.S	U.T.S	Elongation	HAZ		Weld metal
			MPa	MPa	MPa	MPa	%	min	max	mean
MAW-L	1		761	825	796	848	22.1	330	225	265
	5		739	825	783	811	22.2	385	228	260
		ε_{pl}, %	0.09		0.10-0.14					
SAW-L	2		761	793	672	767	22	335	222	242
	6		759	786	693	749	23.3	325	230	240
		ε_{pl}, %	0.16		0.12-0.14					
SAW-C	3		774	804	6333	762	23.5	335	232	240
	7		754	795	722	778	24	330	220	258
		ε_{pl}, %	0.12		0.12-0.14					
MAW-C	4		782	822	757	796	21.8	335	220	265
	8		769	800	781	814	20	325	225	255
		ε_{pl}, %	0.085		0.07-0.11					

Y.S. - yield strength; U.T.S.- ultimate tensile strength; ε_{pl}, % - plastic strain; L – longitudinal; C – circular

There are two basic reasons for differences in mechanical properties in tested prototype. The first one is stress concentration. The highest strains are the consequence of stress concentration, global, due to 5° knee, and local, due to weldment shape. affecting strain distribution. The second reason is level of undermatching, which is different for SAW and MAW welded joints. Longitudinal welded joints and positions are more stressed then circular, and this produces more pronounced difference in stress and strain distribution. It is also necessary to take into account the tendency of pressure vessel to take under pressure simplest form approaching to sphere or cylinder to achieve more uniform stress distribution. With all this in mind it is possible to conclude the yielding will start first in position of lower material strength, in undermatched weld metal, and at the location of highest stress concentration in the vicinity of knee and where it is caused by imperfection of welded joint shape. Applied instrumentation, strain gauges 53, 59, 2 and 34, enabled to quantify residual plastic strains ε_{pl}, in weld metals after first and second pressurizing (Fig. 2-7). In addition, in the second loading the behavior of strain gauge 3 had been monitored. Strain developed uniformly in parent metal (SG53) and circular SAW weld metal SC (SG59).

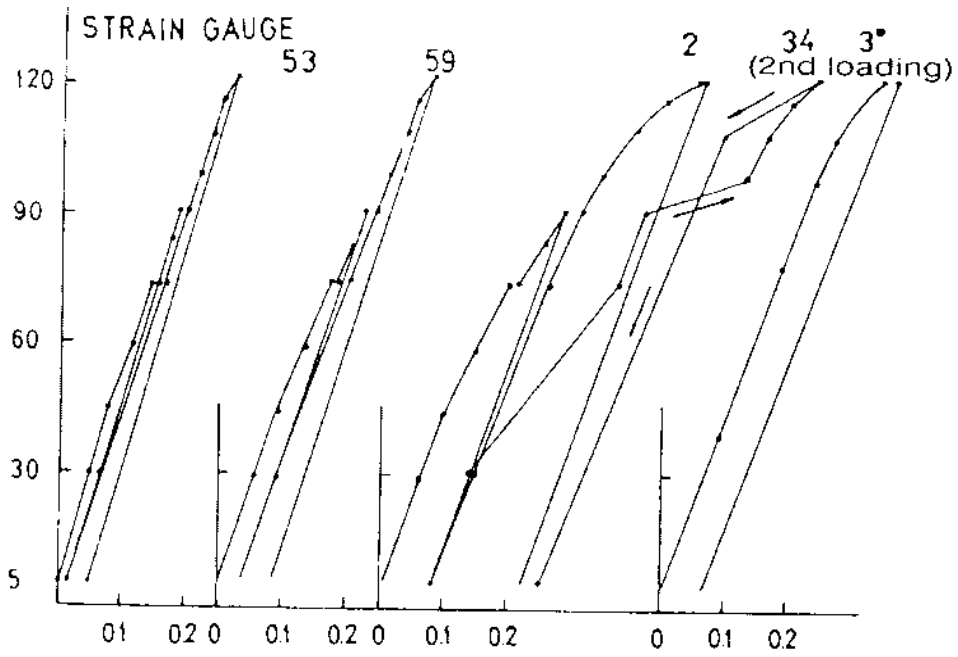

Figure 2-8. Typical relationships between pressure and strain

3 - FINITE ELEMENT ANALYSIS OF SOLIDS

3-1. Introduction

The finite element method (FEM) is a numerical technique for solving problems which are described by partial differential equations or can be formulated as a functional minimization. A domain of interest is represented as an assembly of finite elements. Approximating functions in finite elements are determined in terms of nodal values of a physical field which is sought. A continuous physical problem is transferred into discretized finite element problem with unknown nodal values.

3-2. Formulation of finite element equation

Several approaches can be used to transform the physical formulation of the problem to its finite element discrete analogue. If the physical formulation of the problem is a differential equation then the most popular method of its finite element formulation is the Galerkin method. If the physical problem can be formulated as a minimization of a functional and then variational formulation of the finite element is usually use

3-3.Linear-elastic finite element analysis

Let us consider a three-dimensional elastic body subjected to surface and body force. In addition, displacement is specified on some surface area. For a given geometry of the body, applied force, displacement boundary condition, and material stress-strain law it is necessary to determine the displacement field for the body.

-Displacement vector u , along coordinates axes X, Y and Z

$$u = \{uvw\} \tag{3-1}$$

-Strain vector ε :

$$\varepsilon = \{\varepsilon_x \varepsilon_y \varepsilon_z \varepsilon_{xy} \varepsilon_{xz} \varepsilon_{yz}\} \tag{3-2}$$

-Strain-displacement relationship:

$$\varepsilon = D\ \{u\} \tag{3-3}$$

Where D is the matrix differentiation Operator:

$$D = \begin{matrix} \partial/\partial x & 0 & 0 \\ 0 & \partial/\partial y & 0 \\ 0 & 0 & \partial/\partial z \\ \partial/\partial y & \partial/\partial x & 0 \\ 0 & \partial/\partial z & \partial/\partial y \\ \partial/\partial z & o & \partial/\partial x \end{matrix} \tag{3-4}$$

-Stress vector σ :

$$\sigma = \{\sigma_x \sigma_y \sigma_z \sigma_{xy} \sigma_{xz} \sigma_{yz}\} \tag{3-5}$$

-Stress- strain relationship of elastic body (Hook's law):

$$\sigma = E\ \{\varepsilon\} \tag{3-6}$$

Where E is the elasticity matrix:

$$E = \begin{matrix} \lambda+2\mu & \lambda & \lambda & 0 & 0 & 0 \\ \lambda & \lambda+2\mu & \lambda & 0 & 0 & 0 \\ \lambda & \lambda & \lambda+2\mu & 0 & 0 & 0 \\ 0 & 0 & 0 & \mu & 0 & 0 \\ 0 & 0 & 0 & 0 & \mu & 0 \\ 0 & 0 & 0 & 0 & 0 & \mu \end{matrix} \tag{3-7}$$

$$\lambda = \frac{vE}{1+v\ (1-2v)}$$

$$\mu = \frac{E}{2(1+2v)}$$

Where:

E=Young's modulus

v=poisson's ratio

The purpose of FEA solution of elastic problem is to find such displacement field which provides minimum to functional of total potential energy $\prod$:

$$\prod = \int_V \frac{1}{2} \{\varepsilon\}^T \ \sigma \ dv - \int_V \{u\}^T \ p^V \ dV - \int_V \{u\}^T \ p^S \ dS \qquad (3\text{-}8)$$

Where:

$$p^V = \{\mathrm{p_x^V} \ \mathrm{p_y^V} \ \mathrm{p_z^V}\} \text{Vector of body force} \qquad (3\text{-}9)$$

$$p^S = \{\mathrm{p_x^S} \ \mathrm{p_y^S} \ \mathrm{p_z^S}\} \text{Vector of surface force} \qquad (3\text{-}10)$$

3-3-1.Three dimensional isoparametric elements

-Shape function:

Hexahedral (or brick type) linear-8 nodes and quadratic 20-nodes three-dimensional elements are illustrated in fig (3-1). The term isoparametric means that geometry and displacement field are interpolated with the same function shape.

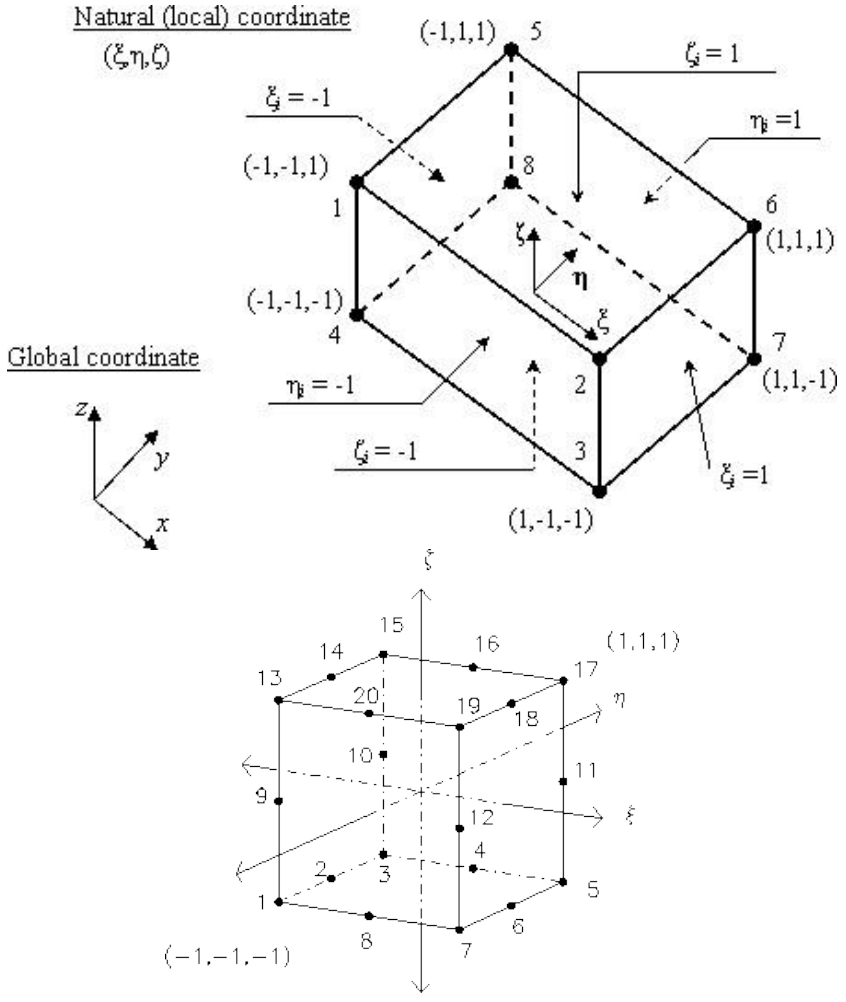

Figure 3-1. The linear and quadratic elements

Interpolation functions are polynomials of local coordinates ξ, η, ζ ($-1 \leq \xi, \eta, \zeta \leq 1$). Both coordinates and displacement are interpolated with the same function: $u = N\ \{q\}$

$$u = \{uvw\} \tag{3-11}$$

$$q = \{u_1 v_1 w_1 u_2 v_2 w_3 \ldots\}$$

$$x = N\ x^e$$

$$x = xyz \tag{3-12}$$

$$x^e = \{x_1 y_1 z_1 x_2 y_2 z_2 \ldots\}$$

Here $u, v, w,$ are displacements at point at point with local coordinate ξ, η, ζ ; $u_i, v_i, w_i,$ are displacement values at nodes $x, y, z,$ are point coordinates and x_i, y_i, z_i, are coordinates of nodes. The matrix of shape functionis:

$$N = \begin{matrix} N_1 & 0 & 0 & N_2 & 0 & 0 & \ldots \\ 0 & N_1 & 0 & 0 & N_2 & 0 & \ldots \\ 0 & 0 & N_1 & 0 & 0 & N_2 & \ldots \end{matrix} \tag{3-13}$$

Shape function of linear element is equal to:

$$N_i = \frac{1}{8}\ 1 + \xi_O\ (1 + \eta_0)(1 + \zeta_0)$$

$$\xi_O = \xi\xi_i,\ \eta_0 = \eta\eta_i,\ \zeta_0 = \zeta\zeta_i \tag{3-14}$$

Shape function of quadratic element with 20 nodes can be written as:

$$N_i = \tfrac{1}{8}\ 1 + \xi_O \quad 1 + \eta_0 \quad 1 + \zeta_0 \quad (\xi_0 + \eta_0 + \zeta_0 - 2) \text{ vertices}$$

$$N_i = \tfrac{1}{4}\ 1 - \xi^2 \quad 1 + \eta_0 \quad 1 + \zeta_0 \quad i = 2, 6, 14, 18 \tag{3-15}$$

$$N_i = \frac{1}{4}\ 1 - \eta^2 \quad 1 + \xi_O \quad 1 + \zeta_0 \qquad i = 4, 8, 16, 20$$

$$N_i = \frac{1}{4}\ 1-\zeta^2\quad 1+\xi_O\quad 1+\eta_0\ \ i=9,10,11,12$$

In the above relation $\xi_i, \eta_i, \zeta_i,$ are values of local coordinates $\xi, \eta, \zeta,$ at nodes.

-Strain displacement matrix:

The strain vector $\{\varepsilon\}$ contains six different components of strain tensor

$$\varepsilon\ = \{\varepsilon_x \varepsilon_y \varepsilon_z \varepsilon_{xy} \varepsilon_{xz} \varepsilon_{yz}\} \tag{3-16}$$

The strain-displacement matrix has the following appearance:

$$B\ =\ D\quad N\ [B_1 B_2 B_3 \ldots]$$

$$B_i = \begin{matrix} \frac{\partial N_i}{\partial x} & 0 & 0 \\ 0 & \frac{\partial N_i}{\partial y} & 0 \\ 0 & 0 & \frac{\partial N_i}{\partial z} \\ \frac{\partial N_i}{\partial y} & \frac{\partial N_i}{\partial x} & 0 \\ 0 & \frac{\partial N_i}{\partial z} & \frac{\partial N_i}{\partial y} \\ \frac{\partial N_i}{\partial z} & 0 & \frac{\partial N_i}{\partial x} \end{matrix} \tag{3-17}$$

Derivatives of shape function with respect to global coordinates are obtained as follows:

$$\begin{matrix} \frac{\partial N_i}{\partial x} \\ \frac{\partial N_i}{\partial y} \\ \frac{\partial N_i}{\partial z} \end{matrix} = [J]^{-1} \begin{matrix} \frac{\partial N_i}{\partial \xi} \\ \frac{\partial N_i}{\partial \eta} \\ \frac{\partial N_i}{\partial \zeta} \end{matrix} \tag{3-18}$$

Where the Jacobian matrix has the following appearance:

$$J\ =\ \begin{matrix} \frac{\partial x}{\partial \xi} & \frac{\partial y}{\partial \xi} & \frac{\partial z}{\partial \xi} \\ \frac{\partial x}{\partial \eta} & \frac{\partial y}{\partial \eta} & \frac{\partial z}{\partial \eta} \\ \frac{\partial x}{\partial \zeta} & \frac{\partial y}{\partial \zeta} & \frac{\partial z}{\partial \zeta} \end{matrix} \tag{3-19}$$

The partial derivative of x, y, z with respect to ξ, η ,ζ are found by differentiation of displacements expressed through shape functions and nodal displacement values:

$$\frac{\partial x}{\partial \xi} = \frac{\partial N_i}{\partial \xi} x_i \,, \frac{\partial x}{\partial \eta} = \frac{\partial N_i}{\partial \eta} x_i \,, \frac{\partial x}{\partial \zeta} = \frac{\partial N_i}{\partial \zeta} x_i$$

$$\frac{\partial y}{\partial \xi} = \frac{\partial N_i}{\partial \xi} y_i, \frac{\partial y}{\partial \eta} = \frac{\partial N_i}{\partial \eta} y_i, \frac{\partial y}{\partial \zeta} = \frac{\partial N_i}{\partial \zeta} y_i \qquad (3\text{-}20)$$

$$\frac{\partial z}{\partial \xi} = \frac{\partial N_i}{\partial \xi} z_i \,, \frac{\partial z}{\partial \eta} = \frac{\partial N_i}{\partial \eta} z_i \,, \frac{\partial z}{\partial \zeta} = \frac{\partial N_i}{\partial \zeta} z_i$$

The transformation of integrals from the global coordinates system to local coordinate system is performed with the use of determinant of Jacobian matrix:

$$dV = dxdydz = |J| d\xi d\eta d\zeta \qquad (3\text{-}21)$$

- Element properties

Element equilibrium equation has the following form:

$$K \quad q \quad = \quad p \qquad (3\text{-}22)$$

Element matrices and vectors:

Stiffness matrix

$$K \quad = \quad \dot{}_V [B]^T \; E \quad B \; dV \qquad (3\text{-}23)$$

Force vector (volume and surface loads):

$$p \quad = \quad \dot{}_V [N]^T \; P^V \; dV + \; \dot{}_S [N]^T \; P^S \; dS \qquad (3\text{-}24)$$

The elasticity matrix E is:

$$E \quad = \quad \begin{matrix} \lambda + 2\mu & \lambda & \lambda & 0 & 0 & 0 \\ \lambda & \lambda + 2\mu & \lambda & 0 & 0 & 0 \\ \lambda & \lambda & \lambda + 2\mu & 0 & 0 & 0 \\ 0 & 0 & 0 & \mu & 0 & 0 \\ 0 & 0 & 0 & 0 & \mu & 0 \\ 0 & 0 & 0 & 0 & 0 & \mu \end{matrix} \qquad (3\text{-}25)$$

Where λ and μ are elastic constants, which can be expressed through the elasticity modulus E and Poisson's ratio:

$$\lambda = \frac{vE}{1+v\ (1-2v)}, \mu = \frac{E}{2(1+v)} \quad (3\text{-}26)$$

-Integration of the stiffness matrix

Integration of the stiffness matrix for three-dimensional isoparametric elements is carried out in the local coordinate $\xi, \eta, \zeta,$:

$$K = \int_{-1}^{1}\int_{-1}^{1}\int_{-1}^{1}[B(\xi,\eta,\zeta,)]^T\ E\ \ B\ \xi,\eta,\zeta,\ \ d\xi d\eta d\zeta \quad (3\text{-}27)$$

Usually $2 \times 2 \times 2$ integration is used for linear elements integration and integration $3 \times 3 \times 3$ applied to the evaluation of the stiffness matrix for quadratic elements.

- Calculation of strains and stress:

After computing elements matrices and vectors, the assembly process is used to compose the global equation system. Solution of the global equation system provides displacements at nodes of the finite element nodal. Using disassembly nodal displacement for each element can be obtained.

Strains inside an element are determined with the use of displacement, differentiation matrix:

$$\varepsilon = B\ \ q \quad (3\text{-}28)$$

Stresses calculated with the hook's law:

$$\sigma = E\ \{\varepsilon\} \quad (3\text{-}29)$$

The highest precision for displacement gradients are at the geometric center for linear element, and at reduced integration points $2 \times 2 \times 2$ for quadratic hexagonal element.

3-4. Elastic –plastic finite element analysis:

The elastic-plastic stress analysis of solids which conform to plane stress or plane strain conditions is considered. Only the essential expressions will be reproduced

here for theoretical and numerical treatment. The basic laws governing elastic-plastic continuum behavior are summarized before considering numerical formulation. In particular, the form of the yield criterion which governs the onset of plastic flow must be defined as well as the incremental relationship between stress and strain during continuing elastic-plastic deformation. In this section the Von Misses yield criteria, which closely approximate metal plasticity behavior are considered. The basic theoretical expression is then rewritten in a form suitable for numerical manipulation.

3-4-1.The mathematical theory of plasticity:

In order to formulate a theory which models elastic-plastic material deformation three requirements have to be met:

An explicit relationship between stress and strain must be formulated to describe material behavior under elastic conditions, i.e. before the onset of plastic deformation. A yield criterion indicating the stress level at which plastic flow commences must be postulated. A relationship between stress and strain must be developed for post-yield behavior, i.e. when the deformation is made up of both elastic and plastic components.

3-4-2.The yield criteria:

The yield criterion determines the stress level at which plastic deformation begins and can be written in the general form

$$f(\sigma_{ij}) = f(J_2', J_3') = k(k) \tag{3-30}$$

Where f is some function of the deviatoric stress invariants:

$$J_2' = \frac{1}{2}\sigma_{ij}'\sigma_{ij}'$$
$$J_3' = \frac{1}{3}\sigma_{ij}'\sigma_{jk}'\sigma_{ki}' \tag{3-31}$$

In which σ_{ij}' the deviatoric stress components

$$\sigma_{ij}' = \sigma_{ij} - \frac{1}{3}\delta_{ij}\sigma_{kk} \tag{3-32}$$

The term k in eq. (3-30) can be a function of a hardening parameter. The two most common yield criteria employed in the description of the behavior of metals are the Tresca criterion and the Von Misses criterion.

3-4-3.The Von Misses criterion:

Von Misses suggested that yielding occurs when J'_2 reaches a critical value, or

$$J'^{1/2}_2 = k \qquad (3\text{-}33)$$

In which k is a material parameter to be determined the second deviatoric stress invariant, J'_2 can be explicitly written as

$$J'_2 = \frac{1}{2}\sigma_{ij}\sigma_{ij} = \frac{1}{6}\left[(\sigma_1 - \sigma_2)^2 + (\sigma_2 - \sigma_3)^2 + (\sigma_3 - \sigma_1)^2\right]$$
$$= \frac{1}{2}\left[\sigma_x'^2 + \sigma_y'^2 + \sigma_z'^2\right] + \tau_{xy}^2 + \tau_{yz}^2 + \tau_{xz}^2 \qquad (3\text{-}34)$$

Yield criterion (3-33) may be further written as

$$\bar{\sigma} = \sqrt{3}J'^{1/2}_2 = \sqrt{3}k \qquad (3\text{-}35)$$

Where:

$$\bar{\sigma} = \sqrt{\frac{3}{2}}\left\{\sigma'_{ij}\,\sigma'_{ij}\right\}^{1/2} \qquad (3\text{-}36)$$

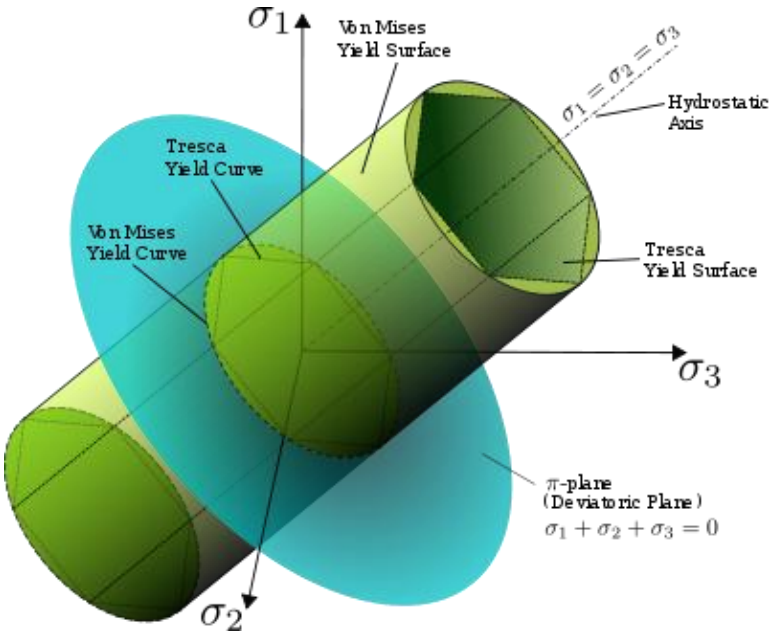

Figure 3-2, Von Misses and Tresca yield surface in principle stress coordinate

The geometrical interpretation of the Von Misses yield surface to be a circular cylinder whose projection onto the π plane is a circle of radius $\sqrt{2}k$). A physical meaning of the constant k can be obtained by considering the yielding of materials under simple stress states. The case of pure shear ($\sigma_1 = -\sigma_2, \sigma_3 = 0$) requires on use of (3-33) and (3-35) that k must equal the yield shear stress. Alternatively the case of unaxial tension ($\sigma_2 = \sigma_3 = 0$) requires that $\sqrt{3}k$ is the unaxial yield stress.

The Tresca yield locus is a hexagon with distances of $\sqrt{\frac{2}{3}}Y$ from origin to apex on the π plane whereas the Von Misses yield surface is a circle of radius $\sqrt{2}k$. By suitably choosing the constant Y, the criteria can be made to agree with each other, and with experiment, for a single state of stress. This may be selected arbitrarily: it is conventional to make the circle pass through the apices of the hexagon by taking the constant Y = $\sqrt{3}k$, the yield stress in simple tension. The criteria then differ most for a state of pure shear, where the Von Misses criterion gives a yield stress $2/\sqrt{3} \approx 1 \cdot 15$ times that given by the Tresca criterion.

3-4-4.Work or strain hardening:

After initial yielding, the stress level at which further plastic deformation occurs may be dependent on the current degree of plastic straining. Thus the yield surface will vary at each stage of the plastic deformation with the subsequent yield surfaces being dependent on the plastic strains in some way. In this text attention is restricted to an isotropic hardening model, in which the original yield surface expands uniformly without translation. The progressive development of the yield surface can be defined by relating the yield stress k to the plastic deformation by means of the hardening parameter k. In a work hardening hypothesis k related to the total plastic work W_P as

$$\kappa = W_p = \int \sigma_{ij} (d\varepsilon_{ij})_p \qquad (3\text{-}37)$$

In which $(d\varepsilon_{ij})_p$ are the plastic components of strain occurring during a strain increment. Alternatively, in a strain hardening hypothesis, k is related to a measure

of the total plastic deformation termed the effective or equivalent plastic strain which is defined incrementally as

$$\kappa = \bar{\varepsilon}_p$$

Then

$$d\bar{\varepsilon}_p = \sqrt{\frac{2}{3}} \left\{ d\varepsilon_{ij}^{(p)} d\varepsilon_{ij}^{(p)} \right\}^{1/2} \tag{3-38}$$

Where $\bar{\varepsilon}_p$ is the result of integrating $d\bar{\varepsilon}_p$ over the strain path.

3-4-5.Elastic-plastic stress/strain relation:

After initial yielding the material behavior will be partly elastic and partly plastic. During any increment of stress, the changes of strain are assumed to be divisible into elastic and plastic components, so that

$$d\varepsilon_{ij} = d\varepsilon_{ij}^{(e)} + d\varepsilon_{ij}^{(p)} \tag{3-39}$$

The elastic strain increment is related to the stress increment by the incremental form of (3-40).

In order to derive the relationship between the plastic strain component and the stress increment a further assumption on the material behavior must be made. In particular it will be assumed that the plastic strain increment is proportional to the stress gradient of a quantity termed the plastic potential Q, so that

$$d\varepsilon_{ij}^{(p)} = d\lambda \frac{\partial Q}{\partial \sigma_{ij}} \tag{3-40}$$

where $d\lambda$ is a constant termed the plastic multiplier. Equation (3-40) is termed the flow rule since it governs the plastic flow after yielding. The potential Q must be a function of J'_2 and J'_3 but as yet it cannot be determined in its most general form. The assumption $f \equiv Q$ gives rise to an *associated* theory of plasticity. In this case (3-40) becomes

$$d\varepsilon_{ij}^{(p)} = d\lambda \frac{\partial f}{\partial \sigma_{ij}} \tag{3-41}$$

And is termed the normality condition since $\partial f / \partial \sigma_{ij}$ is a vector directed normal to the tiled surface at the stress point under consideration.

3-3-6.Matrix formulation:

The theoretical expression reviewed in Section (3-31) will now be converted to matrix form. The yield function, defined in (3-31), can be rewritten as

$$F(\boldsymbol{\sigma}, \kappa) = f(\boldsymbol{\sigma}) - k(\kappa) = 0 \tag{3-42}$$

In which $\boldsymbol{\sigma}$ is the stress vector and k is the hardening parameter which governs the expansion of the yield surface. The differential form of (3-42) is

$$\mathbf{a}^T d\boldsymbol{\sigma} - A d\lambda = 0 \tag{3-43}$$

In which

$$\mathbf{a}^T = \frac{\partial F}{\partial \boldsymbol{\sigma}} = \left\{ \frac{\partial F}{\partial \sigma_x}, \frac{\partial F}{\partial \sigma_y}, \frac{\partial F}{\partial \tau_{xy}}, \frac{\partial F}{\partial \sigma_z} \right\} \tag{3-44}$$

And

$$A = -\frac{1}{d\lambda} \frac{\partial F}{\partial k} dk \tag{3-45}$$

The vector (**a)** is termed the flow vector. Substituting from (3-43) into (3-41) result in

$$d\boldsymbol{\varepsilon} = \mathbf{D}^{-1} d\boldsymbol{\sigma} + d\lambda \frac{\partial F}{\partial \boldsymbol{\sigma}} \tag{3-46}$$

Manipulation of (3-43) and (3-46) leads to the following complete elastic-plastic incremental stress-strain relation

$$d\boldsymbol{\sigma} = \mathbf{D}_{ep} d\boldsymbol{\varepsilon} \tag{3-47}$$

With

$$\mathbf{D}_{ep} = \mathbf{D} - \frac{\mathbf{d}_D \mathbf{d}_D^T}{A + \mathbf{d}_D^T \mathbf{a}}; \quad \mathbf{d}_D = \mathbf{D}\mathbf{a} \tag{3-48}$$

Assumption of a work hardening hypothesis and consideration of unaxial loading conditions result in the scalar term A being given by

$$A = H' = \frac{d\sigma}{d\varepsilon_p} = \frac{E_T}{1 - E_T / E} \tag{3-49}$$

In which E_T is the elastic-plastic tangent modulus of the unaxial stress-strain curve, and E is the elastic modulus of the material.

3-5. ABAQUS software package

ABAQUS software is a developed by Hibbitt, Karlsson and Sorensen, Inc, [11]. It is a complete package of powerful engineering simulation programs, based on the finite element analysis. This simulation software is capable of performing a simple linear analysis to the most complex non-linear simulation. ABAQUS - standard and ABAQUS Explicit are two main modules available in ABAQUS.

ABAQUS - Standard:

ABAQUS -Standard is an all purpose analysis module that can solve a variety of problems covering linear and non-linear problems maintaining the accuracy and reliability of the results. And it consists of three distinct stages, preprocessing, simulation and post processing.

ABAQUS -Explicit:

ABAQUS -Explicit is a special purpose software to analysis module that uses dynamic finite element formulation which is applied to deal with transient and dynamic in nature.

ABAQUS -CAE:

ABAQUS -CAE is the total ABAQUS working interface that includes all the options to generate ABAQUS module, to submit and monitor the job for analysis and also a means to review the results.

3-5-1. Elastic-plastic analysis in ABAQUS:

Stress-strain follows Hook‘s law, giving a linear relationship at low strain values which is true for most materials, but at higher strain the material yield. At which point the material relationship becomes non-linear and irreversible, and can be described as a material nonlinearity. Newton-Raphson method is used in ABAQUS to obtain solution for a non-linear problem by applying the specified loads gradually and incrementally the solution is found reaching towards the final solution. ABAQUS breaks the analysis into a number of load increments and finds the approximate

equilibrium configuration at the end of each load increment. Hence it often takes ABAQUS several iterations for a defined loading condition. The sum of all of the incremental responses is the approximate solution for the nonlinear analysis.

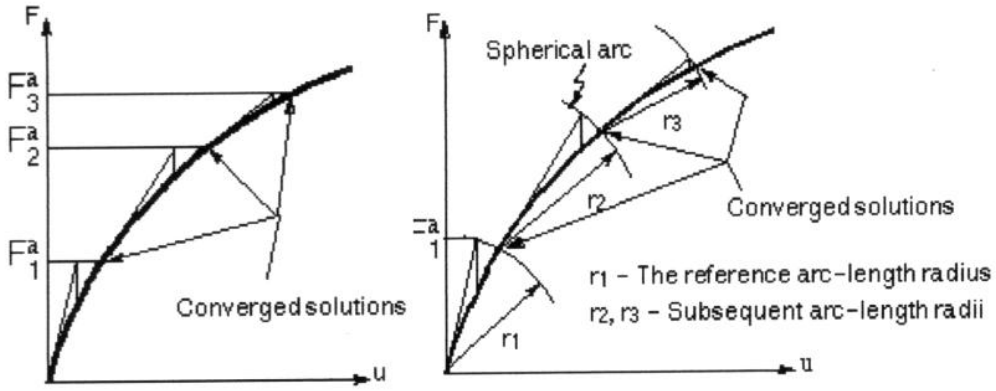

Figure 3-3. Traditional Newton-Raphson method vs. arc-length method

4. Numerical Simulation of full-scale model beahviour

4-1. Introduction

The hydrostatic test of a full-scale model of penstock has been modeled in an FEA ABAQUS, to simulate the behaviour of the finite element model with inner pressure. In the first portion of analysis the von Misses stress distribution will be investigated in two steps; the first load-unload and the second load-unload, and focus on where the yielding initiates and spreads. For the second portion of the numerical study the behavior of the model with initial residual stresses in weld joints will be analyzed for von Misses stresses distribution and initiation of plasticity for first load-unload and second load-unload.

4-2. Methodology and approach of FEA

The geometry model of penstock has been modeled in ABAQUS/CEA, as illustrated in figure 4-1. This model has been sketched as the experimental model of the penstock, figure 2-5, except that the third segment of cylindrical mantle of the experimental model has been left out, because the effect of size of the geometrical model on the run time of finite element analysis. On the other hand, this part of the experimental model is not important and could be negligible.

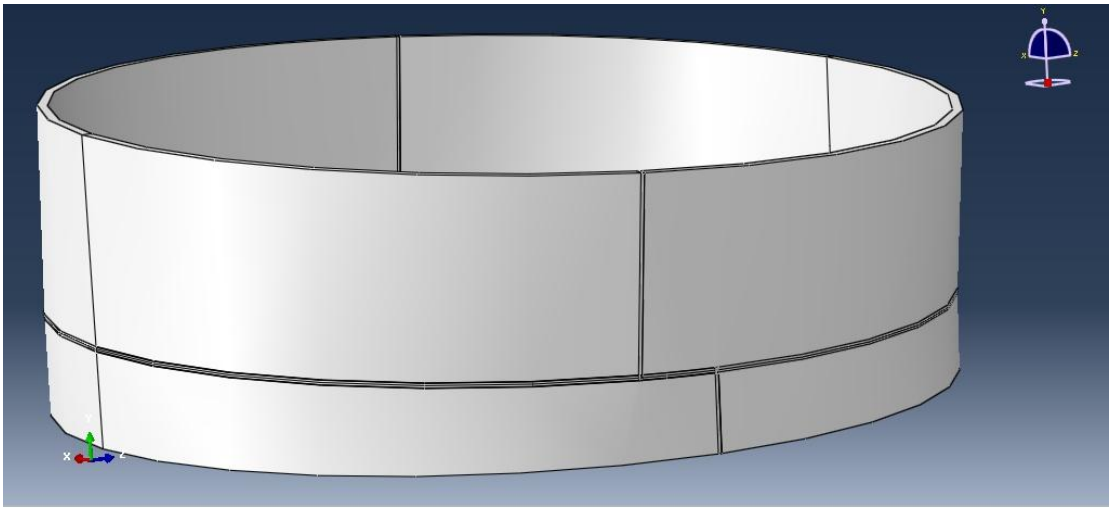

Figure 4-1. The finite element model of penstock as sketched in ABAQUS/CEA

4-2-1. Mechanical properties of FE model

To perform elastic-plastic analysis in ABAQUS, elastic and plastic properties are needed. For elastic properties, we need to define Young‘s module and Poisson‘s ratio in ABAQUS sheet of elasticity. In order to develop the plastic range in ABAQUS, the yield strength and the plastic strain corresponds to each increment of stresses which are needed to define in its ABAQUS sheet. All mechanical properties have been used of this model from experimental test.

4-2-2. Mesh of Finite Element (FE) model

The mesh of the finite element model is an important element, because a poor mesh could show us unrealistic results. A mesh density study was performed to achieve a fine mesh of the model, as illustrated in figure 4-2.

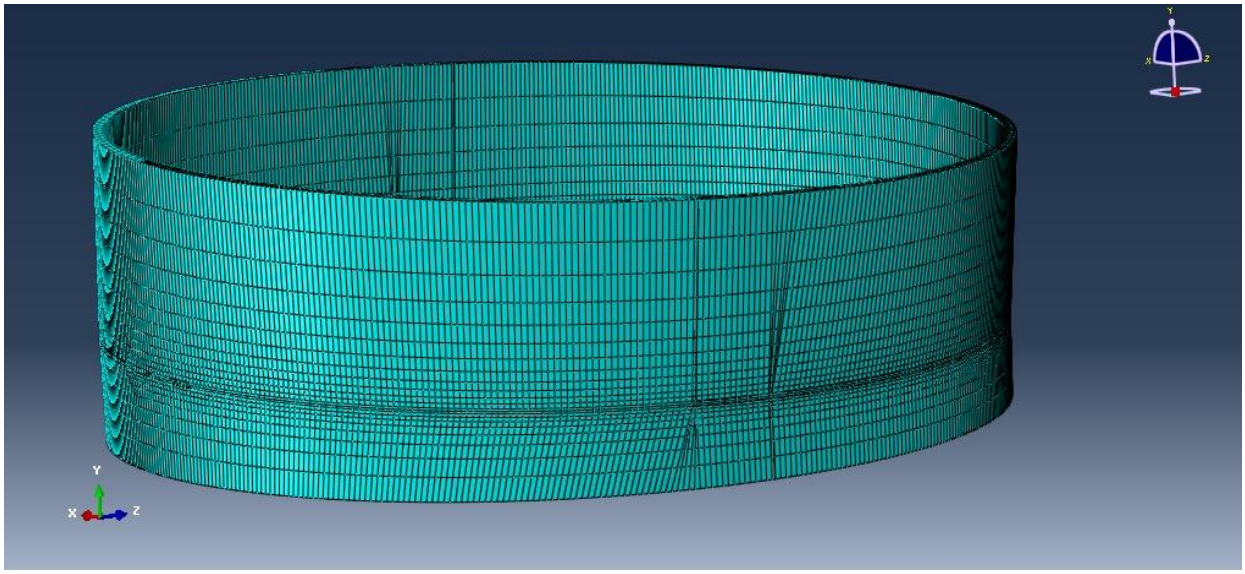

Figure 4-2. The mesh of FE model

4-2-3. Boundary condition and loading

For the finite element to simulate this experiment, the two ends of FE model are fixed from displacing or rotating them in the three directions X, Y and Z. The boundary conditions applied in this simulation are illustrated in figure 4-3. The inner pressure was applied to the inner surface of the finite element model of the penstock.

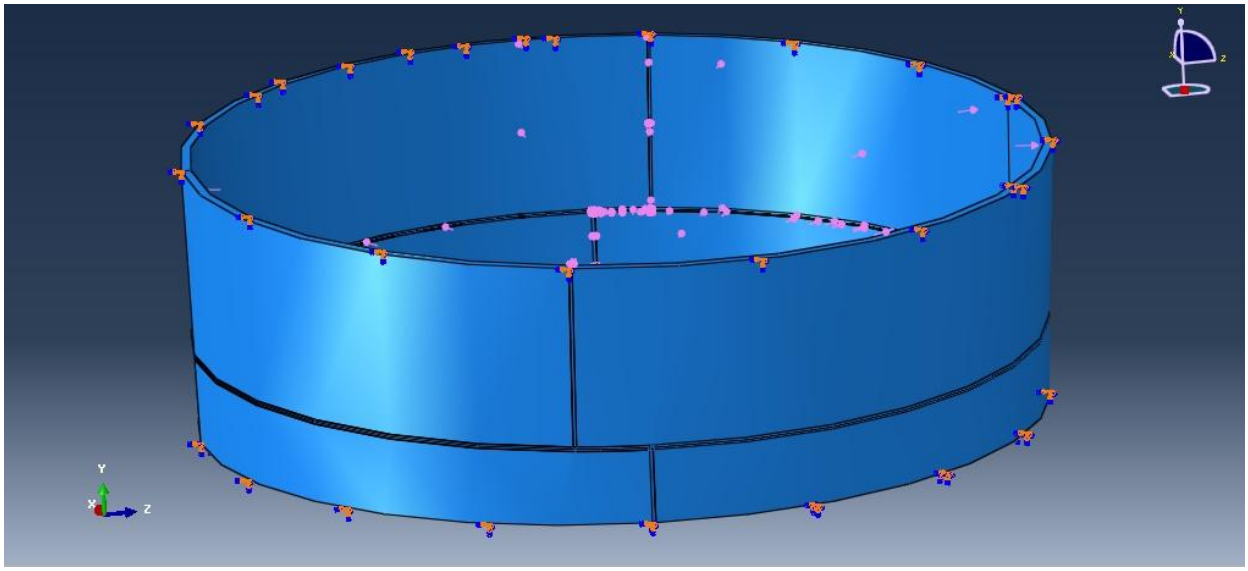

Figure 4-3. Boundary condition and applied inner pressure.

4-2-4. Initial residual stresses for the first loading (FL)

To simulate the effect of residual stresses on the behavior of weld joints of the first load, 40% of yield strength was added to each weld joint as a predefined field, and the six values of von Misses stresses were defined in its ABAQUS sheets.

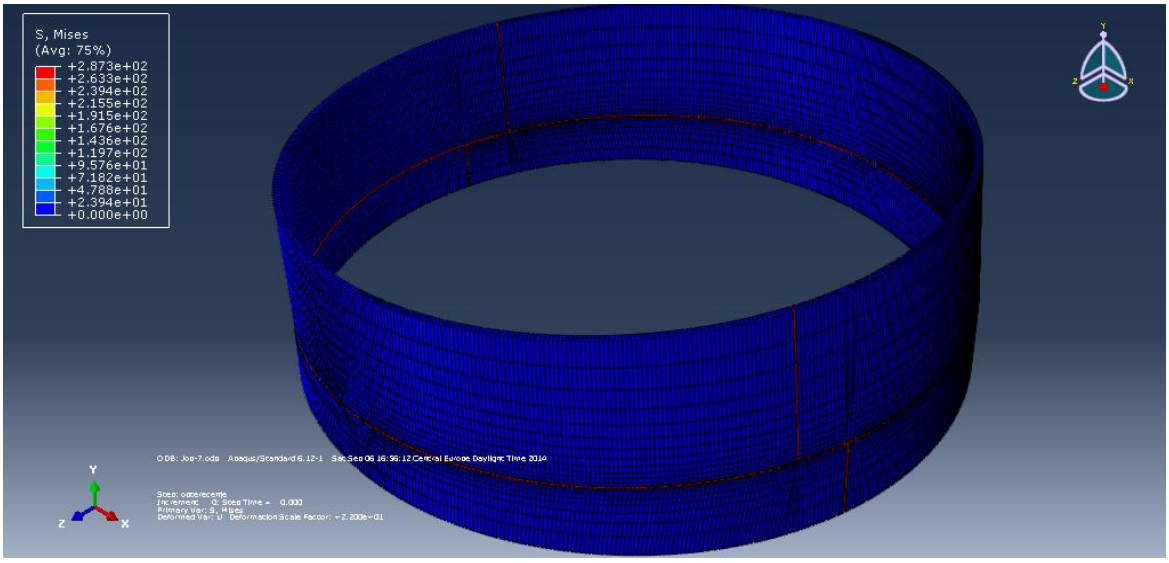

Figure 4-4. The initial residual stresses for FL of FE model

4-2-5.Initial residual stresses for second load

As it will be shown later, the resulted residual stress after first load-unload is much lower than the initial residual stresses, and to simulate the effect of initial residual stresses on weld joints for the second load, we assume the value of initial residual stresses for the second load is equal or a little bit higher than that one used for the first load.

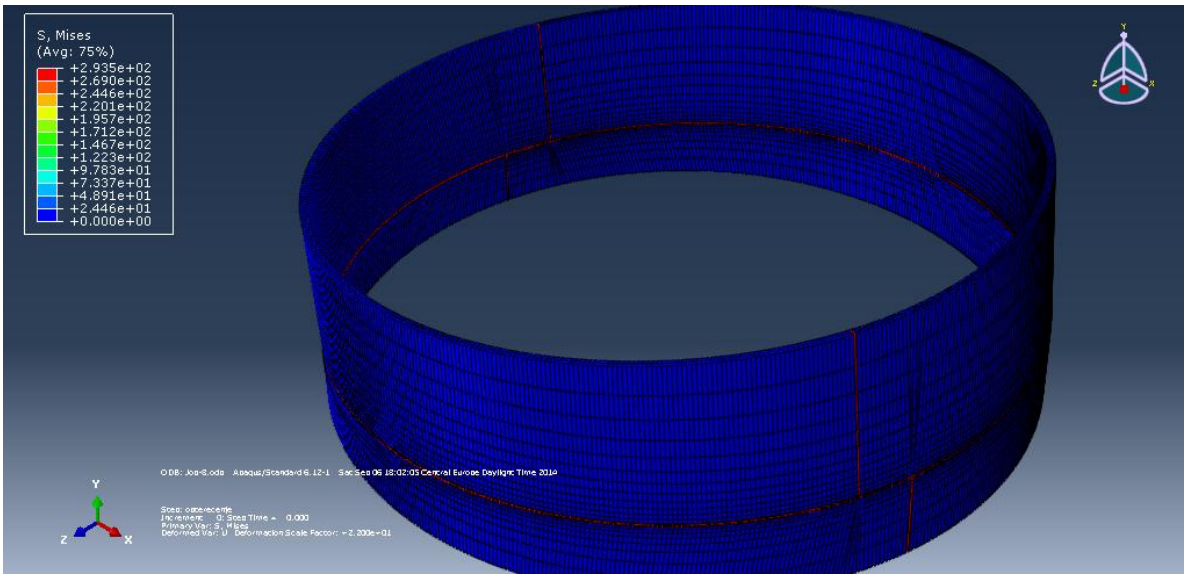

Figure 4-5. Initial residual stresses for SL of FE model

4-2-6. Results and discussion

The FEA results include:

1- Von Misses stresses distribution of full-scale model of FEA model, which is the model loading by inner pressure in two steps, (first load-unload, second load-unload).
2- Von Misses stress-strain curves (FL-UNL, SL-UNL)
3- Von misses stress - Inner pressure curves (FL-UNL, SL-UNL)
4- Inner Pressure - von Misses strain curves (FL-UNL, SL-UNL)
5- Hoop stresses - strain curves (FL-UNL, SL-UNL).

4-2-6-1. Von Misses stresses distribution of FE model for FL (without RS).

Figure 4-6 showed the von Misses distribution of the finite element model for first load as calculated in ABAQUS software. The highest stresses was in the weld joint (LSI SAW), and the base metal at that side. This concentration of stress is due to the geometrical shape of the model, which exerts more stresses (compression) on that side, and the geometry of the model tends to be ideal.

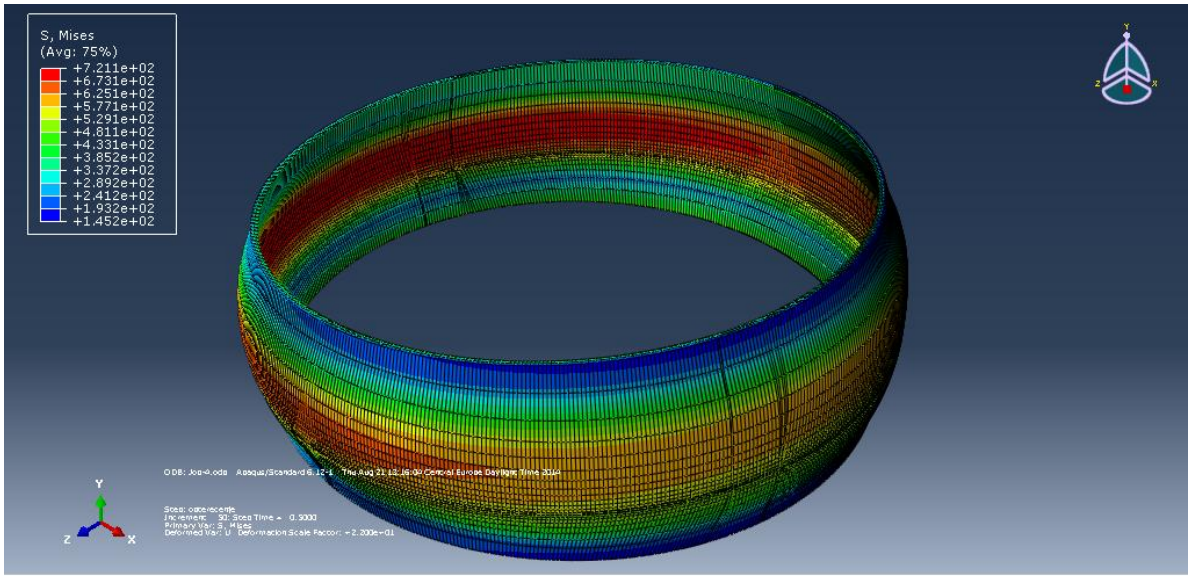

Figure 4-6. Von Misses stresses distribution of FE model of first load, (P =14.5MPa)

4-2-6-2. Plastic strain (FL-UNL).

As indicated in figure (4-7), the plastic strain is only initiated in the weld joint (LS1 Sub Merged Arc (SAW). This behavior is due to the lower yield strength of the joint and its location in the stress concentration region.

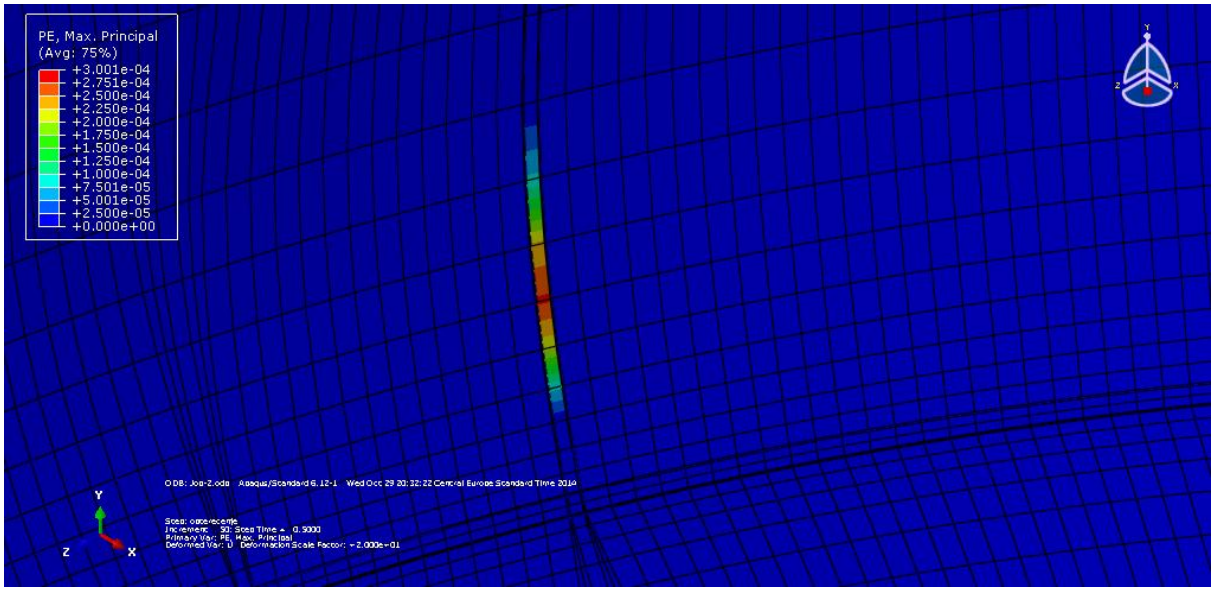

Figure 4-7 plastic deformation of FE model (FL-UNL, P=14.5MPa)

4-2-6-3. Von Misses stress distribution of FE model for SL (without RS).

As the internal pressure increased in the second load of FE model, the level of von Misses stress will be increased, and the distribution of stress has not been changed compared to the first load except the behavior of weld joint (LS1 SAW), which has lower stress than the base metal at that side of stress concentration region due to the effect of initiation of plasticity as indicated in figure 4-8.

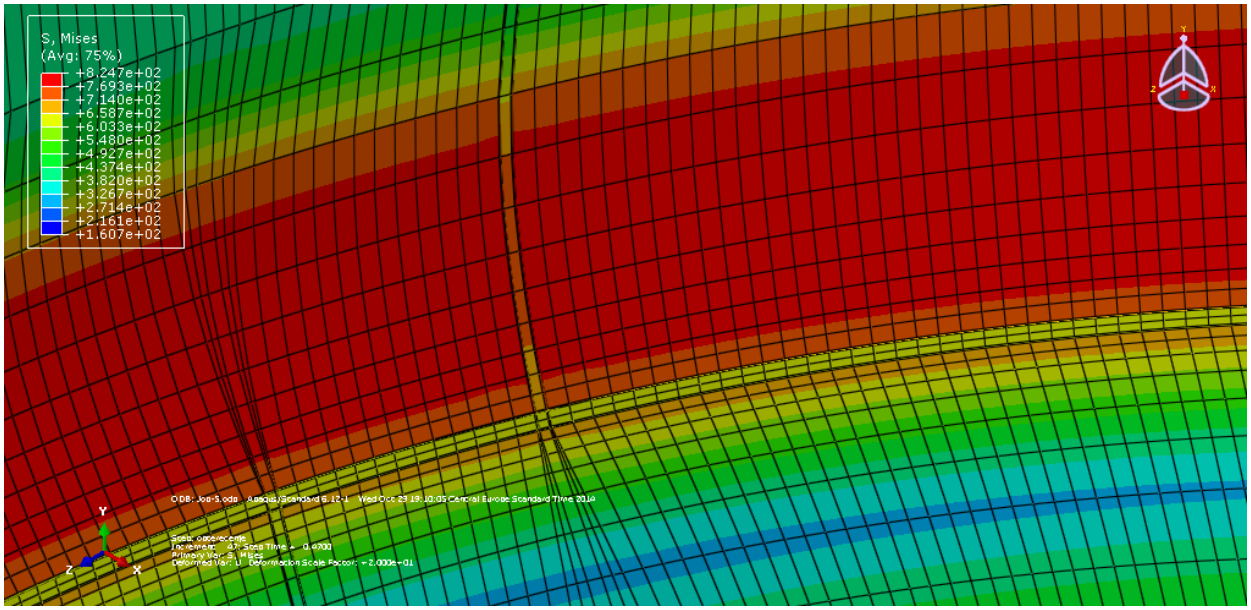

Figure 4-8. von Misses stresses distribution of FE model - second load, p=18.5 MPa

4-2-6-4. Plastic strain (SL-UNL).

As illustrated in figure 4-9, the levels of von Misses stresses have exceeded the yielding of the base metal and weld joints at that side of the stress concentration region and the plasticity initiated and spreads in base metal and weld joints in this area.

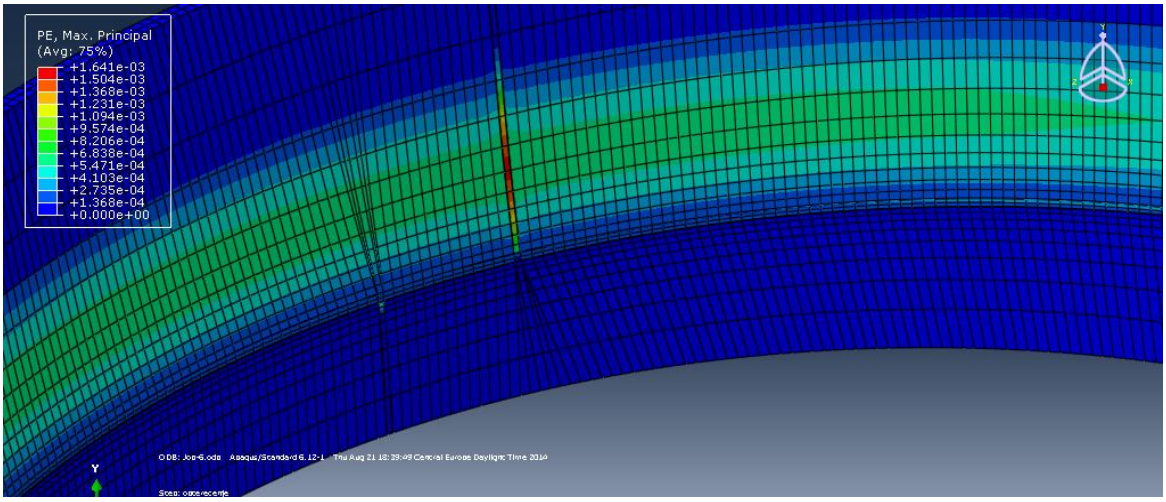

Figure 4-9. plastic deformation of FE model (SL-UNL, P=18.5MPa).

4-2-6-5. Von Misses stress-strain curve of WJ LSI without RS (FL-UNL,SL-UNL).

Figure 4-10 illustrates the behavior of von Misses stress-strain curve of the weld joint (LS1SAW) for first load-unload and second load-unload as calculated in ABAQUS software. This behavior showed the linearity of the stress-strain curve of the loading and unloading behavior for the first and second load.

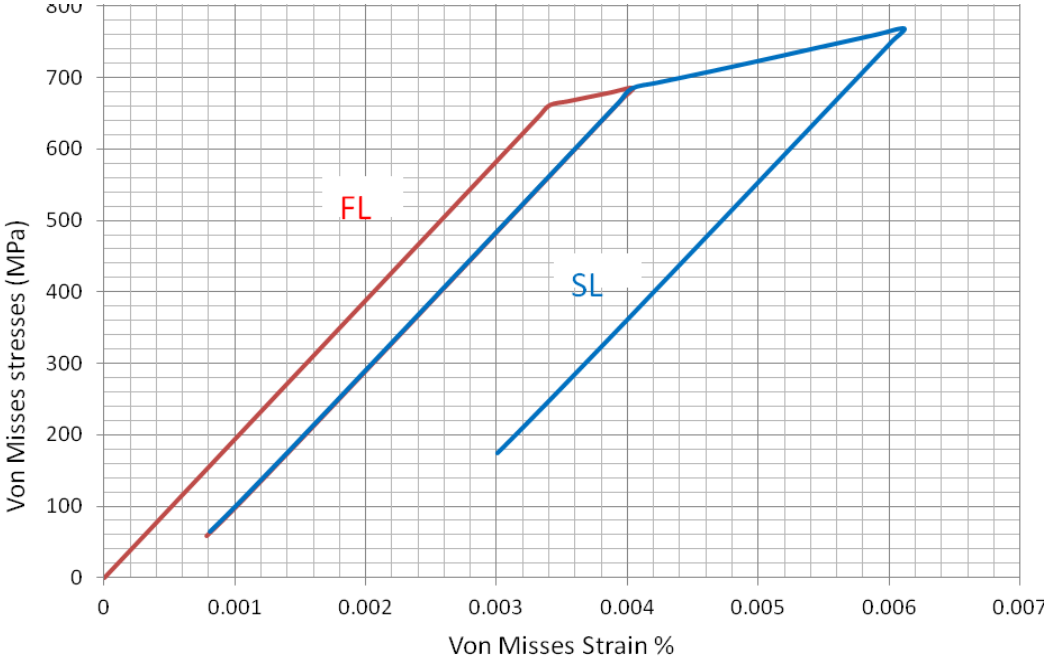

Figure (4-10), Von Misses stress-strain behavior LS1 SAW without RS

4-2-6-6. Von Misses stress-inner Pressure curve of weld joint LSI SAW without RS, (FL-UNL, SL-UNL).

Figure 4-11 shows the behavior of von Misses stresses with loading and unloading of the FE model by inner pressure. As the inner pressure increases the von Misses stresses increases to the yield point of the weld joint, then the changing of Von Misses stresses will be lower. For unloading, the behavior will be linear, until the effect of residual stresses and then it will be non-linear.

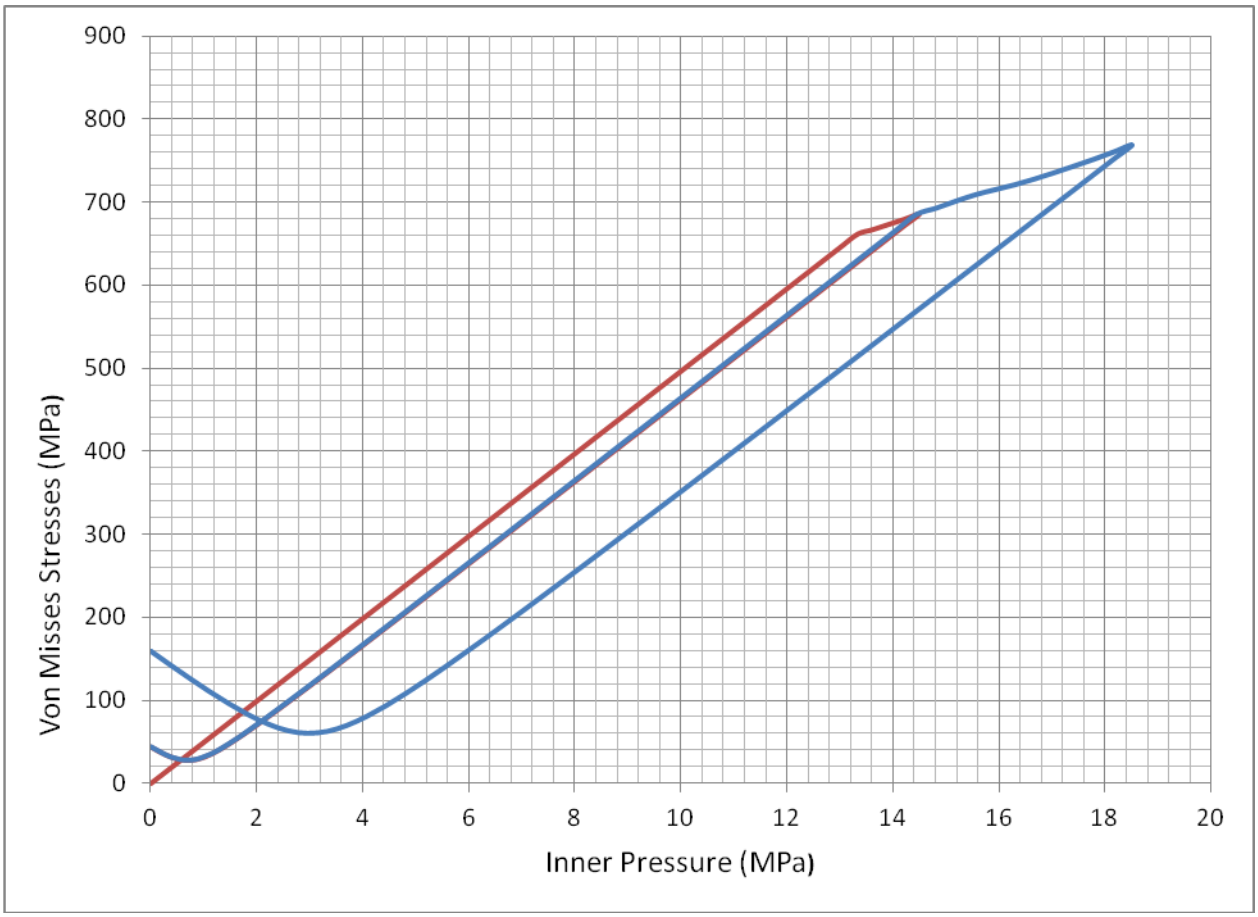

Figure 4-11. Von Misses-Inner Pressure behavior of WM LSI SAW

4-2-6-7. Inner Pressure-Von Misses strain curve of weld joint LSI SAW without RS (FL-UNL, SL-UNL).

The behavior of the von Misses strain with inner pressure as calculated in ABAQUS is illustrated in figure 4-12. This behavior showed linearity during loading and unloading with a little bit of change during plasticity.

4-2-6-8. Hoop stress-strain curve of WJ LS1 without RS (FL-UNL, SL-UNL)

The behavior of hoop stress-strain curve as indicated in figure 4-13. The yielding for the first load starts at 13.3 MPa of inner pressure (531.5 MPa of hoop stresses), while for the second load the plastic deformation initiated at 14.8 MPa of inner pressure (586.1 MPa of hoop stresses).

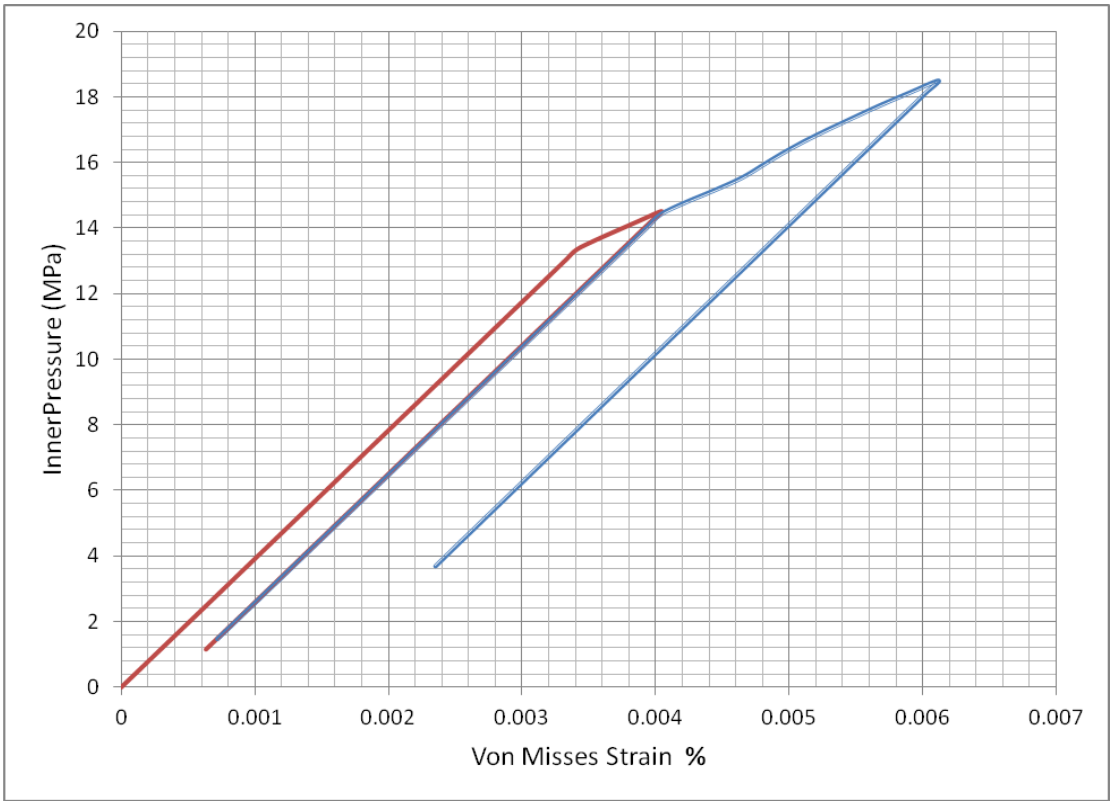

Figure 4-12. The inner Pressure-Von Misses strain of LS1 SAW

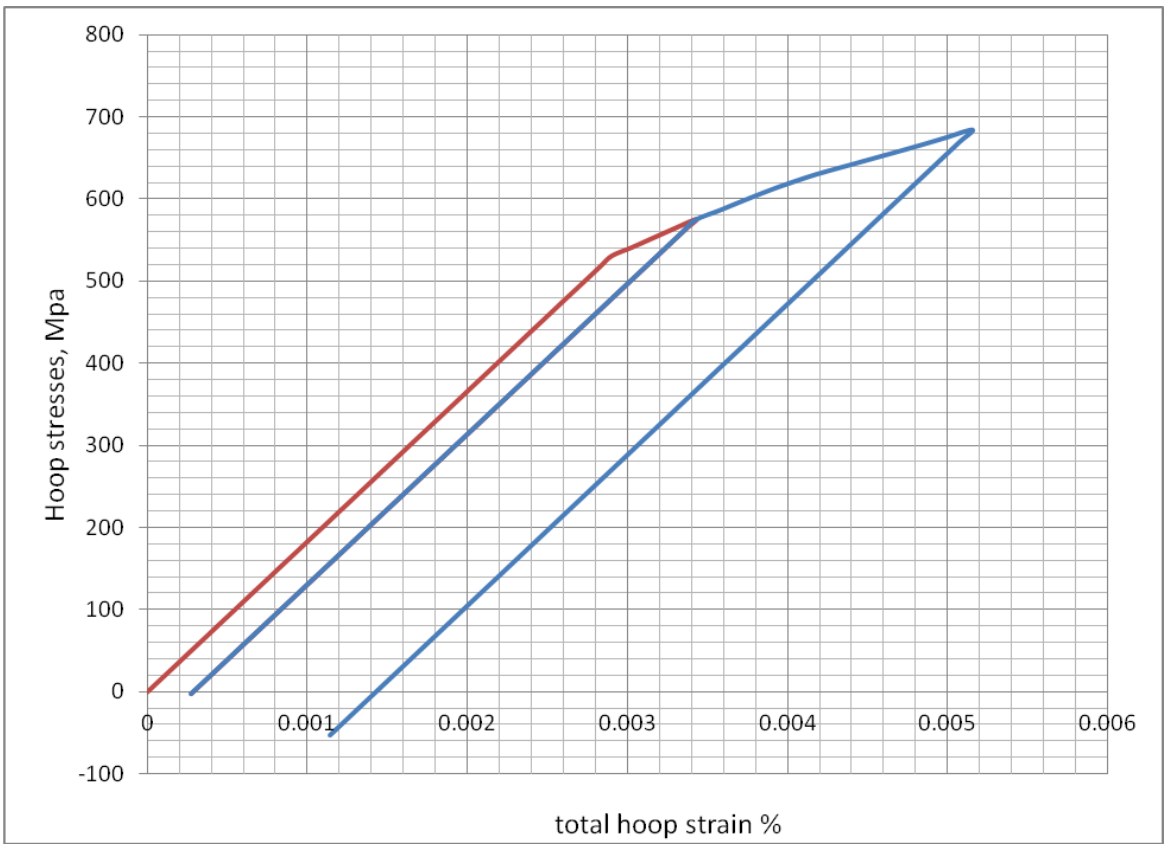

Figure 4-13. Hoop stresses-strain curve of WM LS1 SAW

4-2-6-9. Von Misses stresses distribution of FE model for FL (with RS).

Figure 4-14 shows von Misses stresses distribution of finite element model as calculated in ABAQUS, the highest stress has been in weld joints at the stress concentration side. This high level of stress is due to the effect of initial residual stresses (40% of yield strength) and the geometric shape of the model.

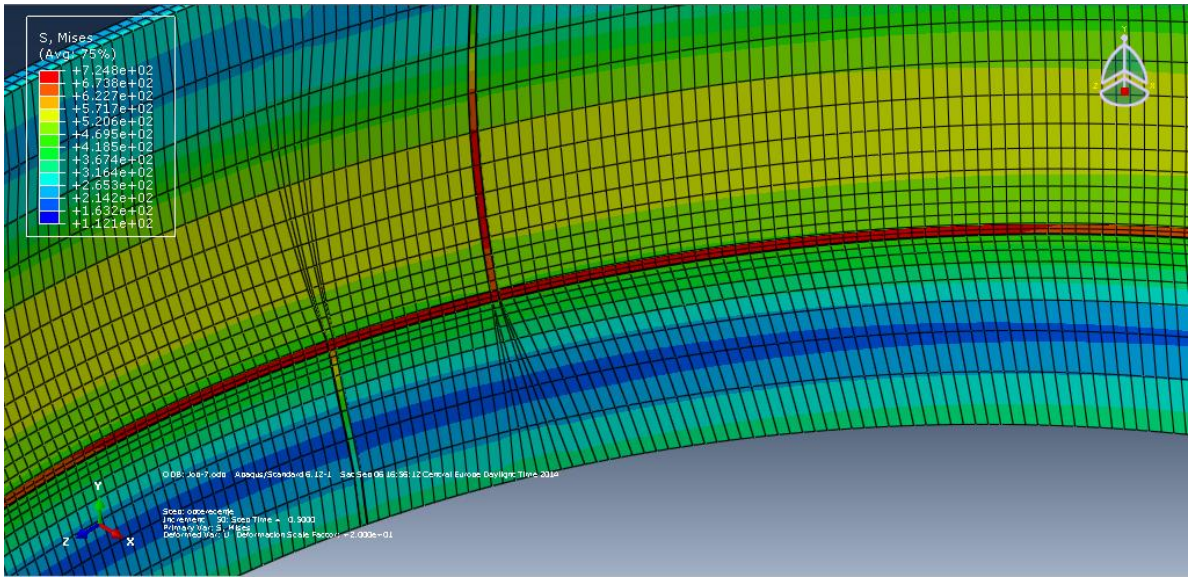

Figure (4-14), von Misses stresses - FE model for first load with RS (P=11.2 MPa).

4-2-6-10. plastic strain (FL-UNL, with RS)

Figure 4-15 shows the initiation of plasticity after first load of FE model, where the plasticity initiated is in the weld joint LS1 SAW. This behavior is due to the lower yield point and its location of this joint.

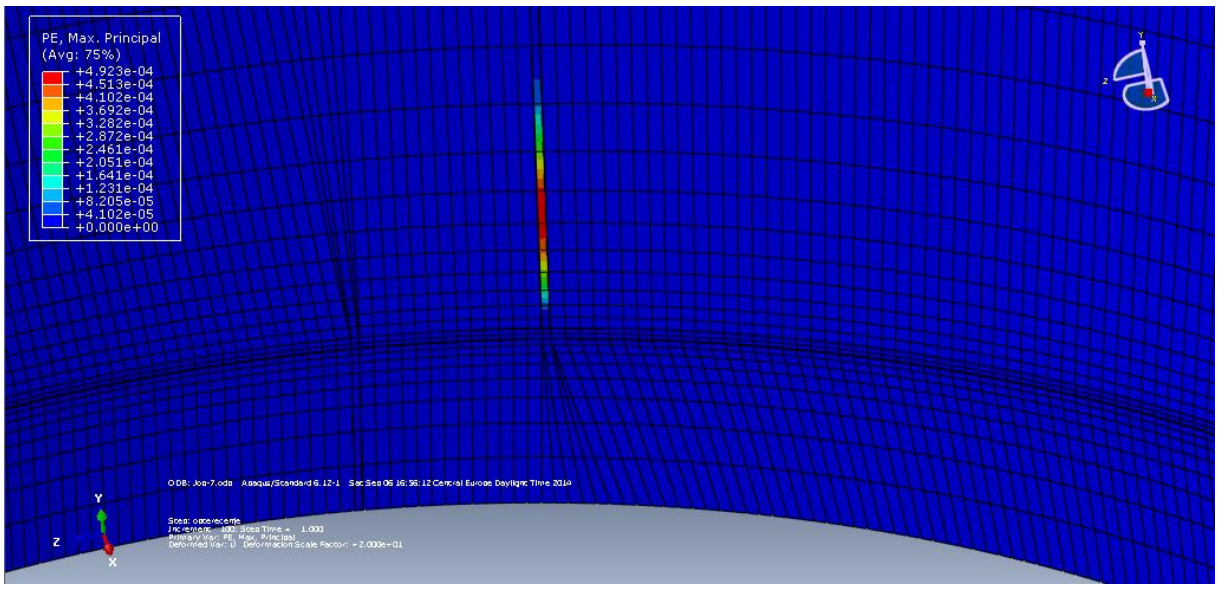

Figure 4-15. The plastic strain of WM LS1 SAW after FL (P=11.2 MPa).

4-2-6-11. Von Misses stresses distribution of FE model for SL (with RS).

Figure 4-16 shows von Misses distribution of FE model for second load with residual stresses, as the inner pressure increased for the second load, the highest von Misses stresses were still in the weld joints at the concentration stress side with a considerable increasing of von Misses stresses in the base metal on that side.

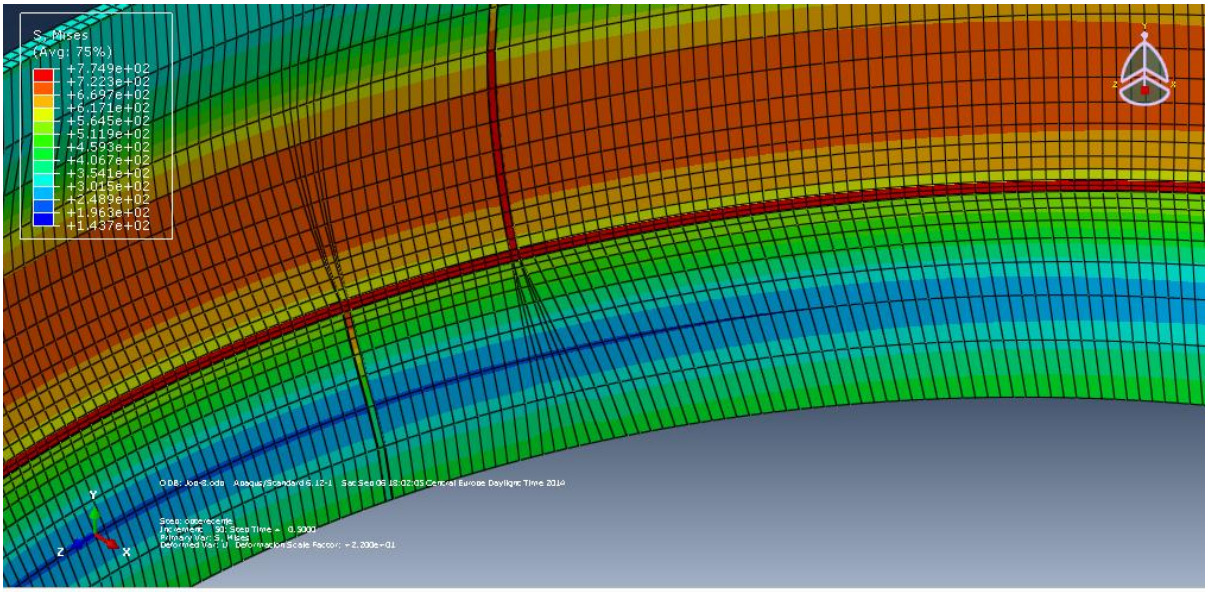

Figure 4-16. Von Misses distribution of FE model for SL with RS (P=14.4MPa).

4-2-6-12. The plastic strain (SL-UNL, with RS).

As the inner pressure increased for second load, the plastic strain initiated in the other weld joints was at the shorter side CMAW, LS3 SEW, Fig. 4-17.

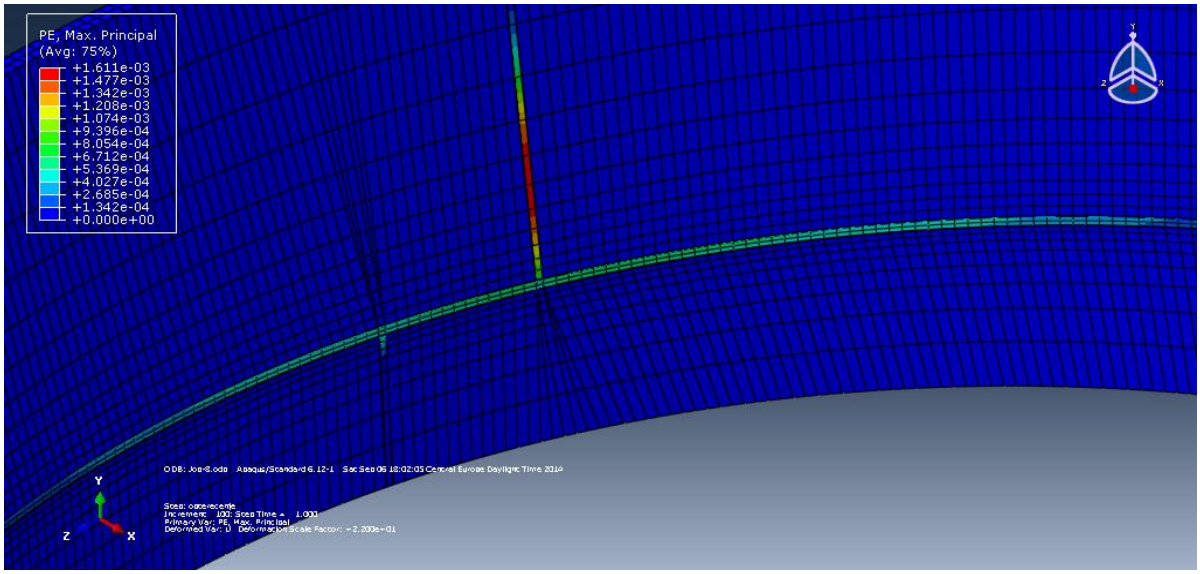

Figure 4-17. The plastic strain of WM LS1 SAW after SL (P=14.4MPa).

4-2-6-13. Von Misses stresses-strains curve of weld metal LS1 SAW, (FL-UNL, SL-UNL, with RS).

The behavior of the von Misses stress-strain curve of weld joint LS1 SAW with residual stresses is similar to the behavior without residual stresses, but it yields at a lower level of inner pressure due to the effect of residual stresses as illustrated in figure 4-18.

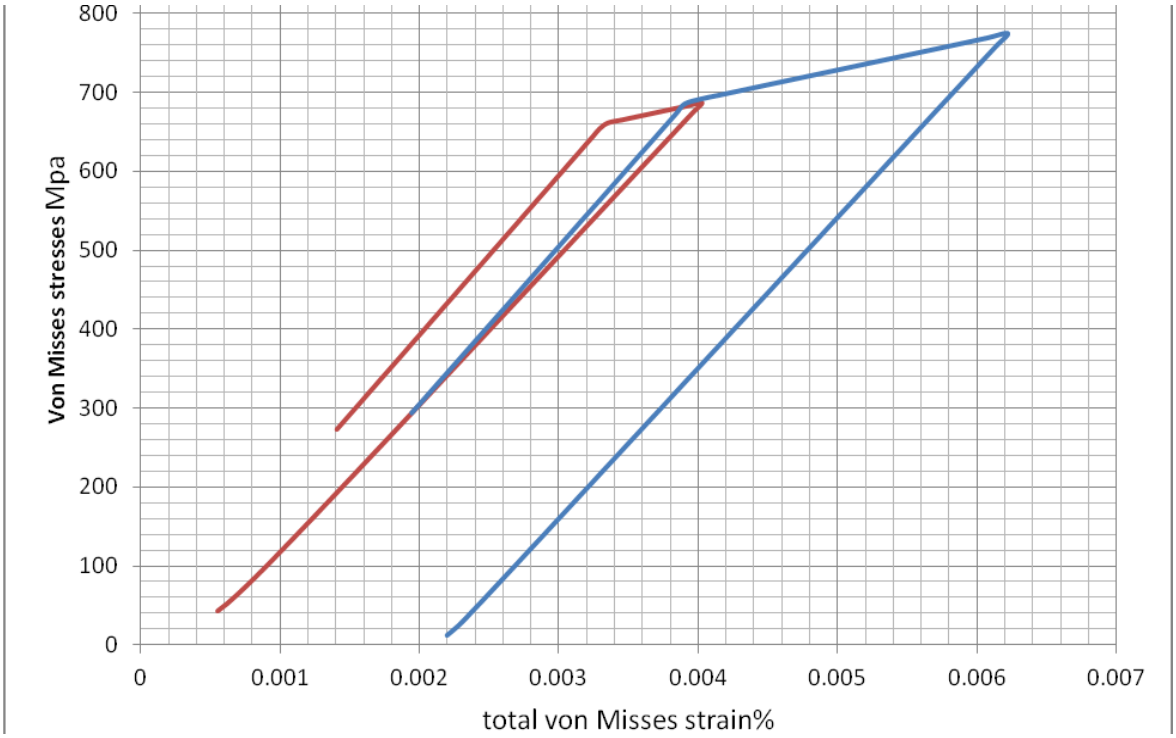

Figure 4-18. von Misses stresses-strain curve of WM LS1 SAW with RS

4-2-6-14. Hoop stresses- strains curve of WM LS1 SAW, FL-UNL, SL-UNL, with RS

The behavior of the hoop-stress-strain curve of the weld joint LS1 SAW with residual stresses showed that the plastic strain for first load was in the direction of axial stresses and not in a circumferential direction (there is no plasticity that appears for first load in hoop stress-strain curve) as indicated in figure 4-19. This behavior is due to the geometric shape of the model (5º angle), which exerts more compression in the axial direction.

4-3. Experimental results with numerical calculations of full-scale model of penstock.

There are three different stress-strain distribution treatments. The first one is the treatment of model as ideal cylindrical pressure vessel which behaves according to the linear elastic formulas, Fig. 4-20. The second distribution will be obtained from strain gauge measurements in both loading – unloading regimes using elastic – plastic formulas. The third treatment will be the use of finite element ABAQUS calculations. The first treatment used for the ideal cylinder pressure vessel can be presented in Tab. 4-1 for the FL-UL and in Tab. 4-2 for the FL-UL and SL-UN.

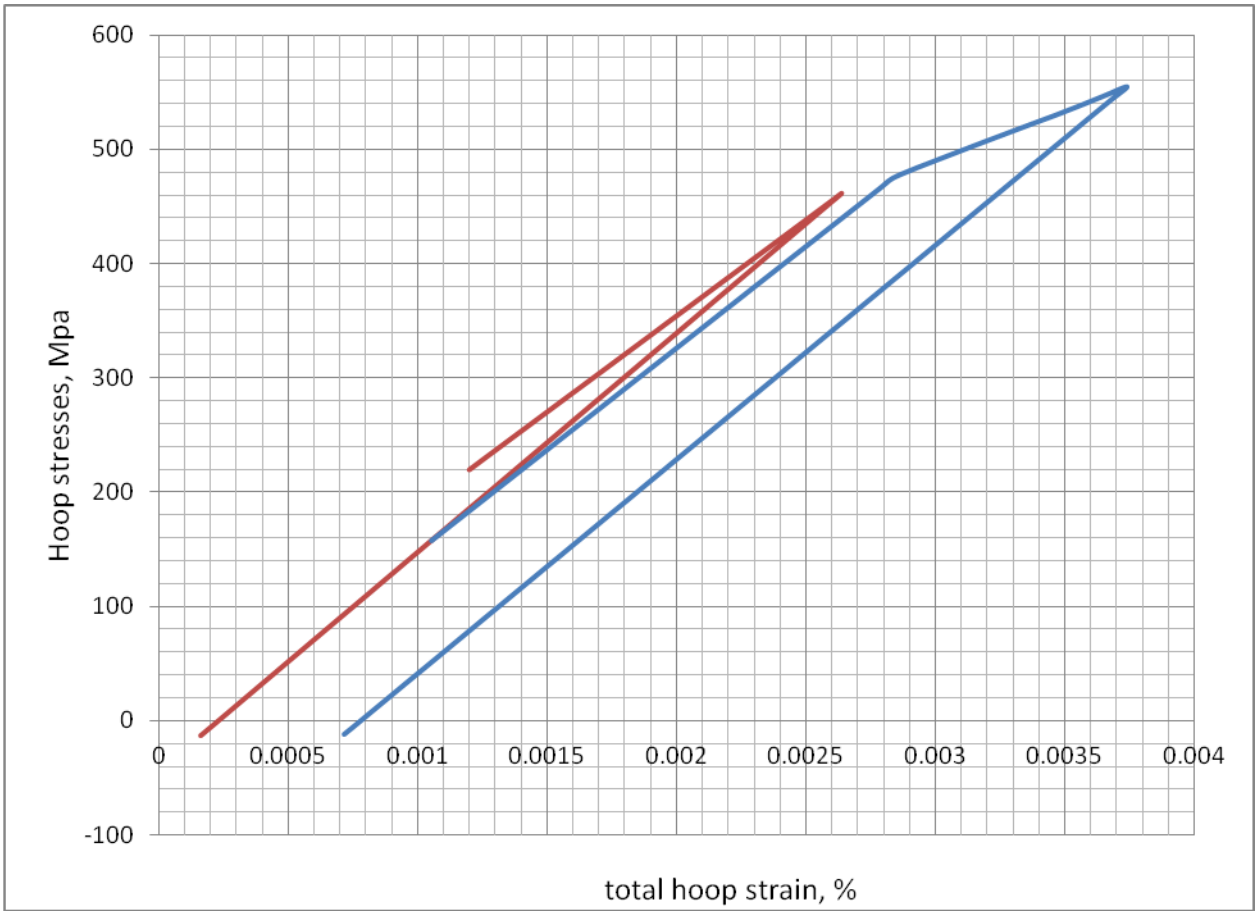

Figure 4-19. Hoop stresses- strain of WM LS1 SAW with RS

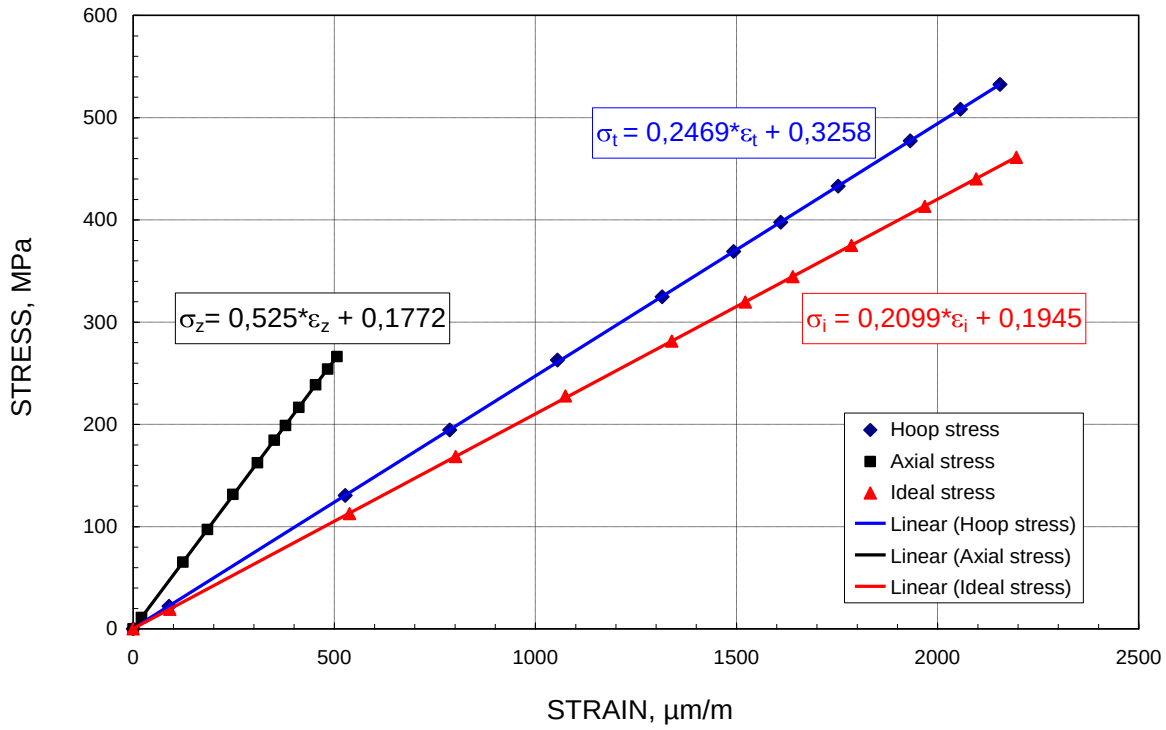

Figure (4-20). Relationships Stress – Strain for ideal cylinder

Table 4-1. Stress – Strain distribution obtained from Stain Gages readings

Pressure MPa	Strain, □m/m			Stresses, MPa		
	□ ε_t	□ ε_z	□ ε_i	□ σ_t	□ σ_z	□ σ_i
0,00	0	0	0	0,0	0,0	0,0
0,50	89	21	91	22,1	11,0	19,1
2,95	528	124	538	130,3	65,2	112,9
4,40	787	185	802	194,4	97,2	168,4
5,90	1055	248	1075	260,7	130,3	225,8
7,35	1315	309	1339	324,8	162,4	281,3
8,35	1493	351	1522	369,0	184,5	319,5
9,05	1619	381	1649	399,9	199,9	346,3
9,80	1753	412	1786	433,0	216,5	375,0
10,80	1932	454	1968	477,2	238,6	413,3
11,50	2057	484	2096	508,1	254,1	440,1
12,05	2155	507	2196	532,4	266,2	461,1

Table 4-2. Stress – Strain distribution obtained from Strain Gages readings

Pressure MPa	Strain, μm/m			Stress, MPa		
	□ε_t	□ε_z	□ε_i	□σ_t	□σ_z	□σ_i
0	0	0	0	0	0	0
0,50	89	21	90	22,0	11,0	19,0
2,95	593	124	599	145,4	69,7	126,0
4,40	855	185	865	210,1	101,9	182,0
5,90	1202	248	1212	294,6	140,4	255,2
7,35	1616	309	1624	394,3	183,2	341,8
8,35	1846	351	1854	450,3	208,8	390,3
9,05	1994	379	2003	486,4	225,5	421,6
0,50	277	21	272	65,4	24,0	57,3
0,00	183	0	183	42,2	12,7	37,5
0,50	277	21	272	65,4	24,0	57,3
2,95	578	124	584	142,0	68,6	123,0
7,35	1534	309	1545	375,4	177,5	325,3
9,05	1879	379	1893	459,9	217,5	398,4
9,80	2060	412	2074	503,9	237,7	436,6
10,80	2301	454	2315	562,4	264,1	487,4
11,50	2484	484	2498	606,7	283,7	525,8
12,05	2649	507	2662	646,4	300,4	560,3
12,05	2654	507	2667	647,6	300,7	561,3
10,80	2413	454	2423	588,3	271,8	510,0
9,00	2064	379	2070	502,5	230,4	435,7
7,35	1717	309	1721	417,6	190,2	362,2
2,95	842	124	838	202,9	86,9	176,3
0,50	362	21	355	85,0	29,9	74,7
0,00	273	0	266	63,0	18,9	56,0

Figure 4-21 presents the Von Misses stress dependence on inner pressure for an ideal cylinder without taking into account the residual stress and stress concentration, together with the calculations obtained using the strain gauges readings in two loading-unloading sequences and finally with finite elements (FE) calculations. FE calculations are showing the linear relationship until they reach the yield strength of the base metal and further plastic behavior and linear unloading. The pressure at which yield strength is reached is about 15 MPa, the pressure which was not used by hydraulic penstock model testing.

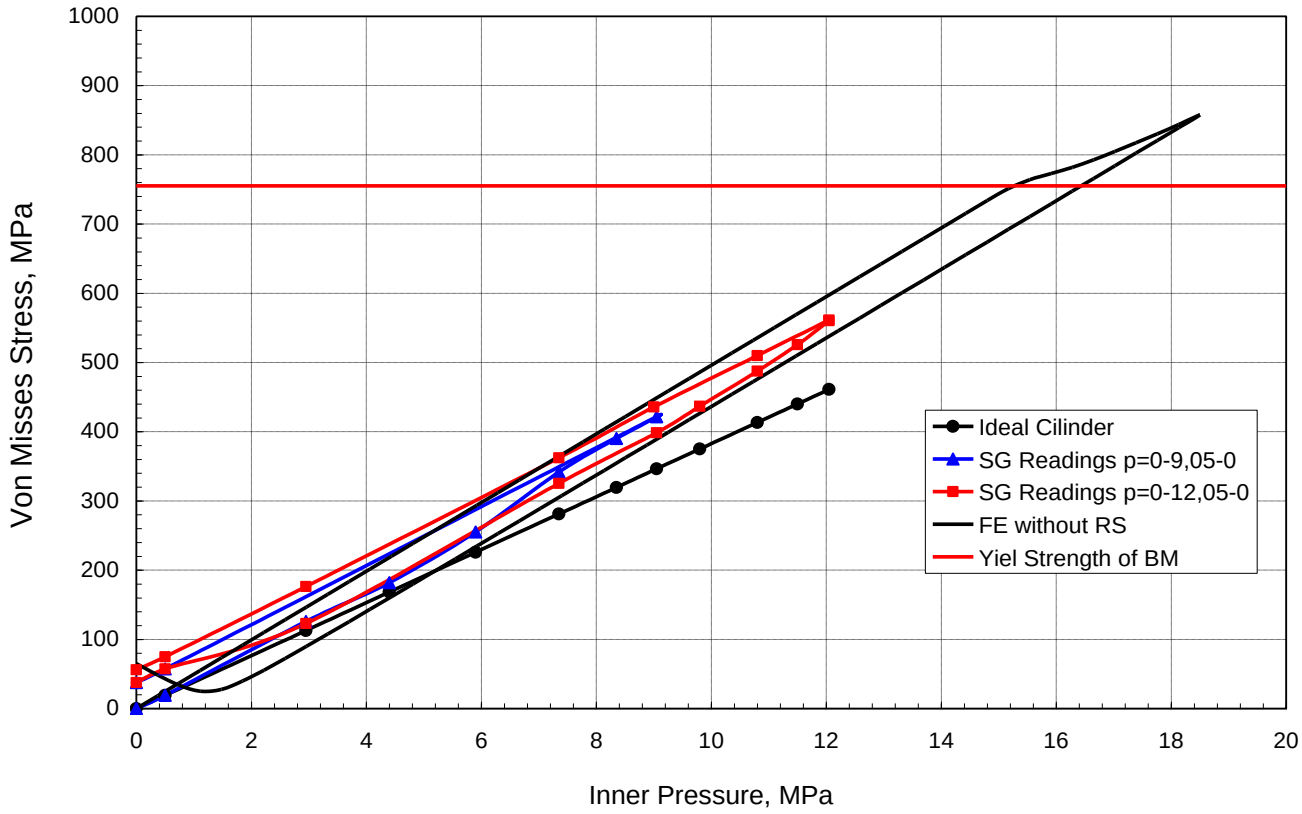

Figure 4-21. BM Von Misses Stress vs. Inner Pressure comparison with FE calculations

Figure 4-22 shows good agreement of Von Misses stress strain dependence obtained for different calculation methods.

Figure 4-23 presents the relationships of inner pressure depending on different ways of presenting the von Misses strain. Von Misses strain is calculated for an ideal cylinder, according to the strain gauge readings and finally using finite element calculations. Both relationships obtained for an ideal cylinder and FE calculations show linear behavior for inner pressure of 12.05 MPa. Strain gauge readings show little deviation from linearity due to the stress concentration, and geometric imperfections.

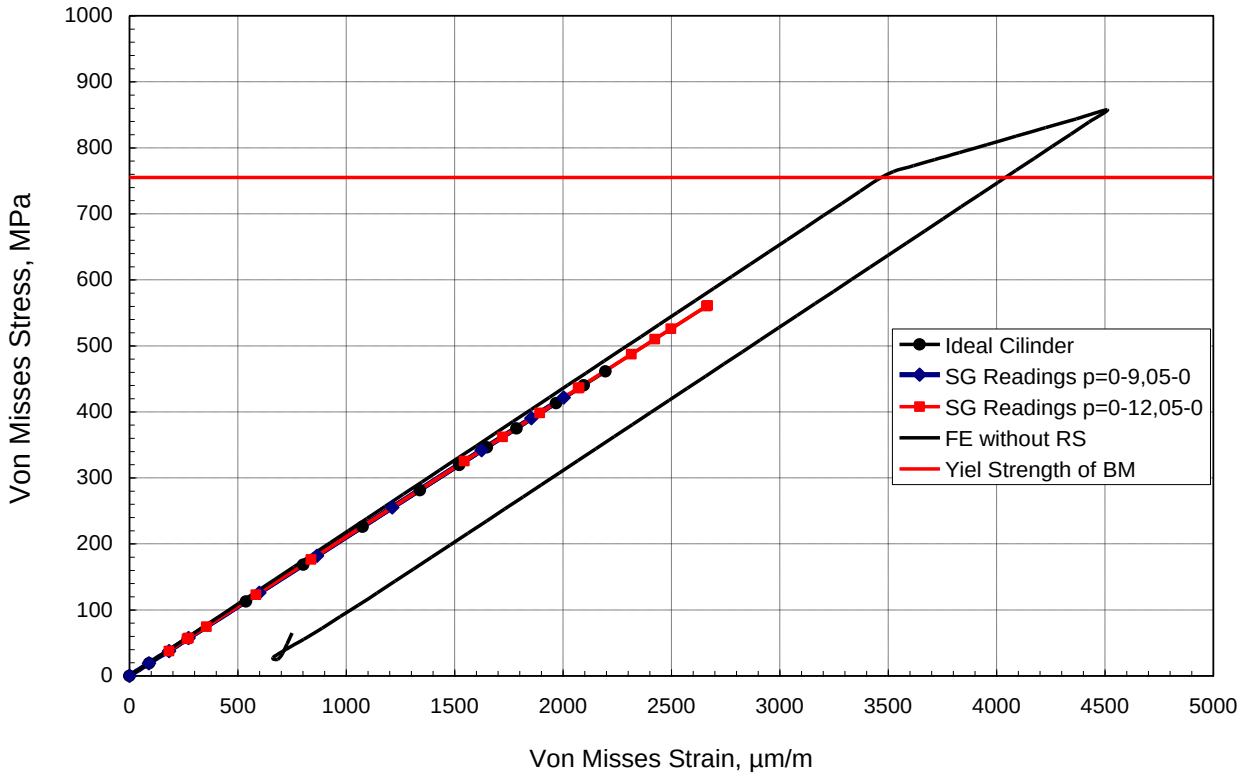

Figure 4-22. Von Misses stress-strain relationships of BM for different calculation methods

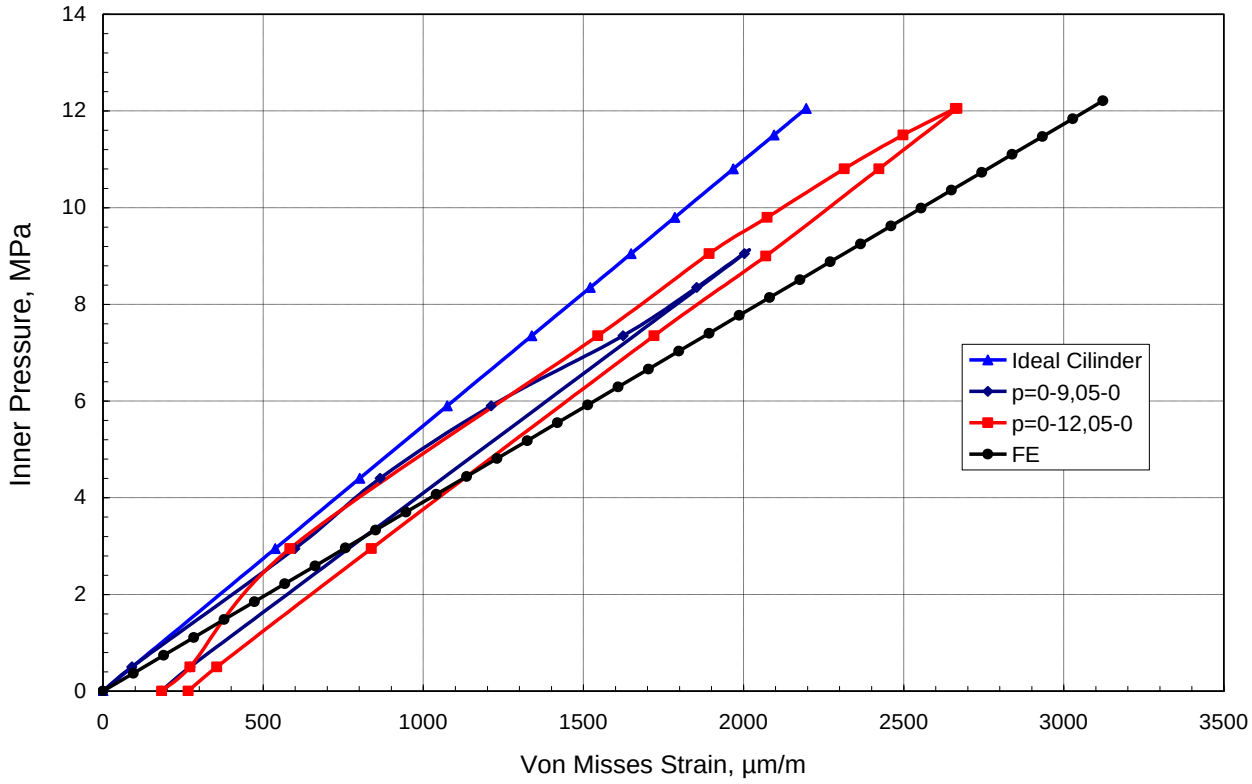

Figure 4-23. Relationships between inner pressure and von Misses strain for Penstock

Figure 4-24 shows linear relationships between the von Misses stress and strain obtained for an ideal cylinder, for strain gauge readings and for FE calculations. It looks like the ideal cylinder and strain gauge readings highly agree but FE calculations show slightly different behavior.

Figure 4-25 shows similar behavior of the linear relationship for ideal cylinder and FE calculations and a slight deviation for results obtained from strain gauges readings. After unloading from 9.05 MPa there was small residual stress which was the starting point for the next loading to 12.05 MPa. Again after unloading was calculated, there was a similar amount of residual stress. The reason for this residual stress is geometrical deviation from the ideal model shape.

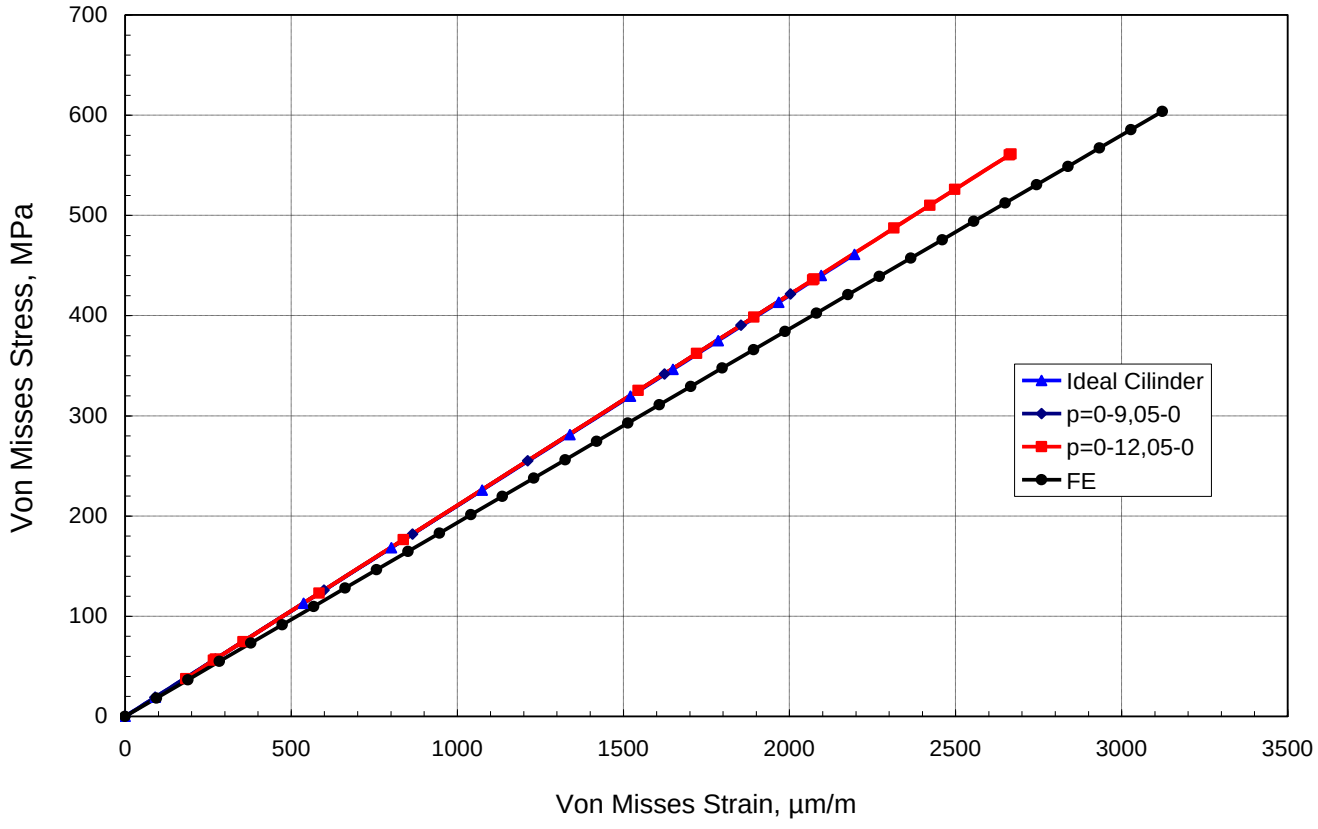

Figure (4-24), Stress – Strain distribution for penstock model

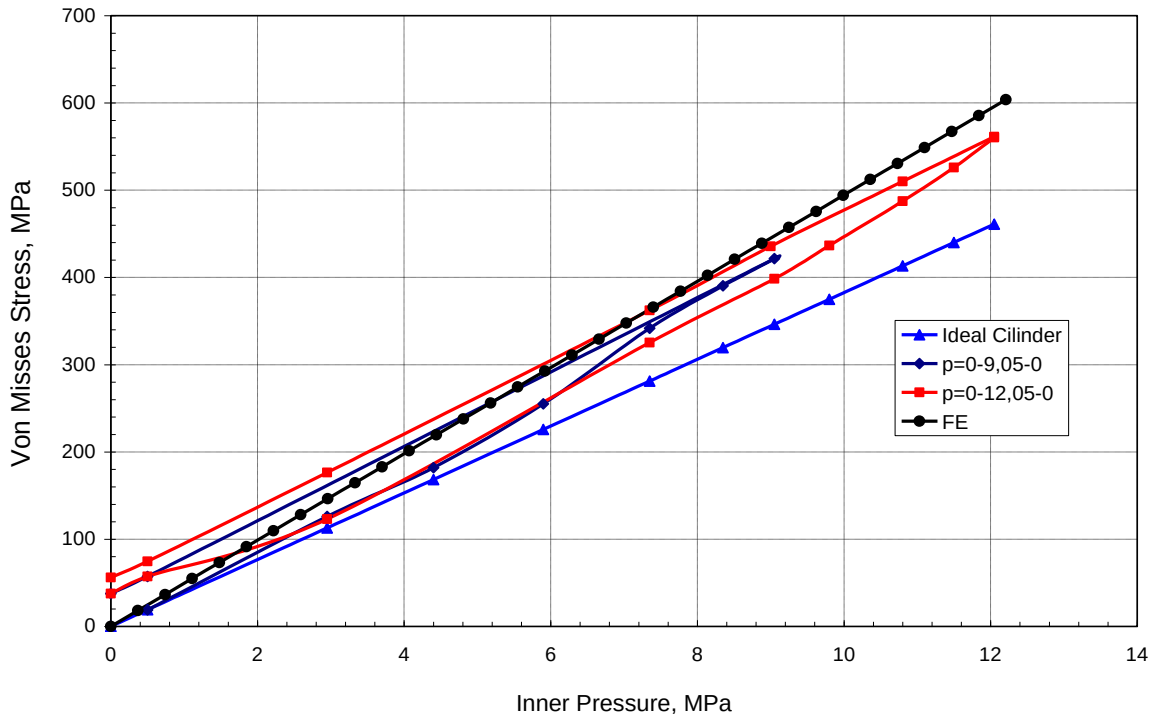

Figure 4-25. Von Misses Stress – Inner Pressure relationship

Figure (4-26) shows the relationships von Misses stress – strain for weld joint LS1 obtained using strain gauge readings, finite element calculations without taking into account residual stresses and geometrical imperfections and finite element calculations using residual stresses into account. The position of weld joint LS1 is on the shorter side of the upper cylinder with a slope of 5° and it is logical to expect high tensile stress and strains because under the inner pressure, the cylinder is trying to reach the ideal cylinder. Good agreement between SG readings and FE calculations is obtained using much higher inner pressure than the one used by experimental testing where the model was tested to 12.05 MPa. Using residual stress of 273 MPa it will once again be in good agreement. Residual stress of 273 MPa is obtained as 40% of yield strength of SMAW weld joint.

Figure (4-27) shows Von Misses stress strain relationships obtained from SG readings, without taking into account residual stresses and with taking residual stress of 273 MPa. Also it is showing the inner pressure correlating with the von Misses strain. The weld joint LS2 is on the longer side of the upper cylinder and under the inner pressure will show lower stress because the cylinder is trying to reach the ideal shape.

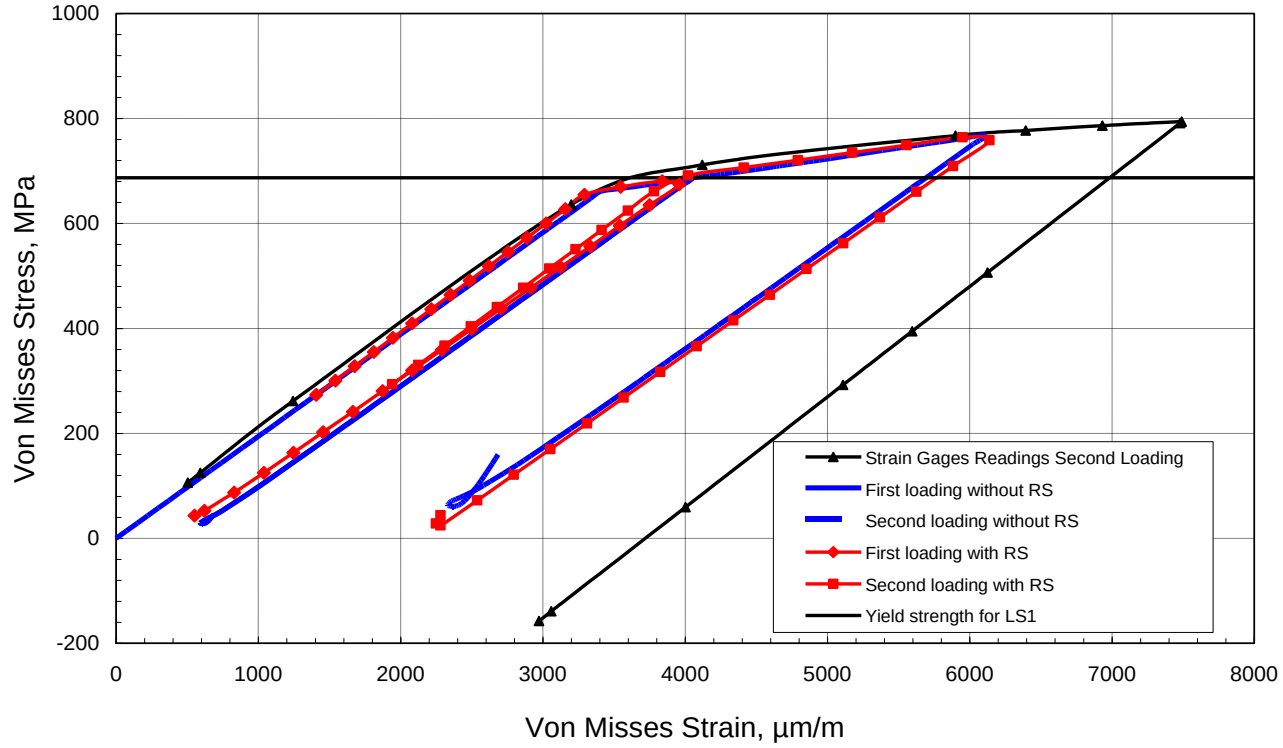

Figure 4-26. Von Misses Stress – Strain relationships for SMAW weld joint LS1

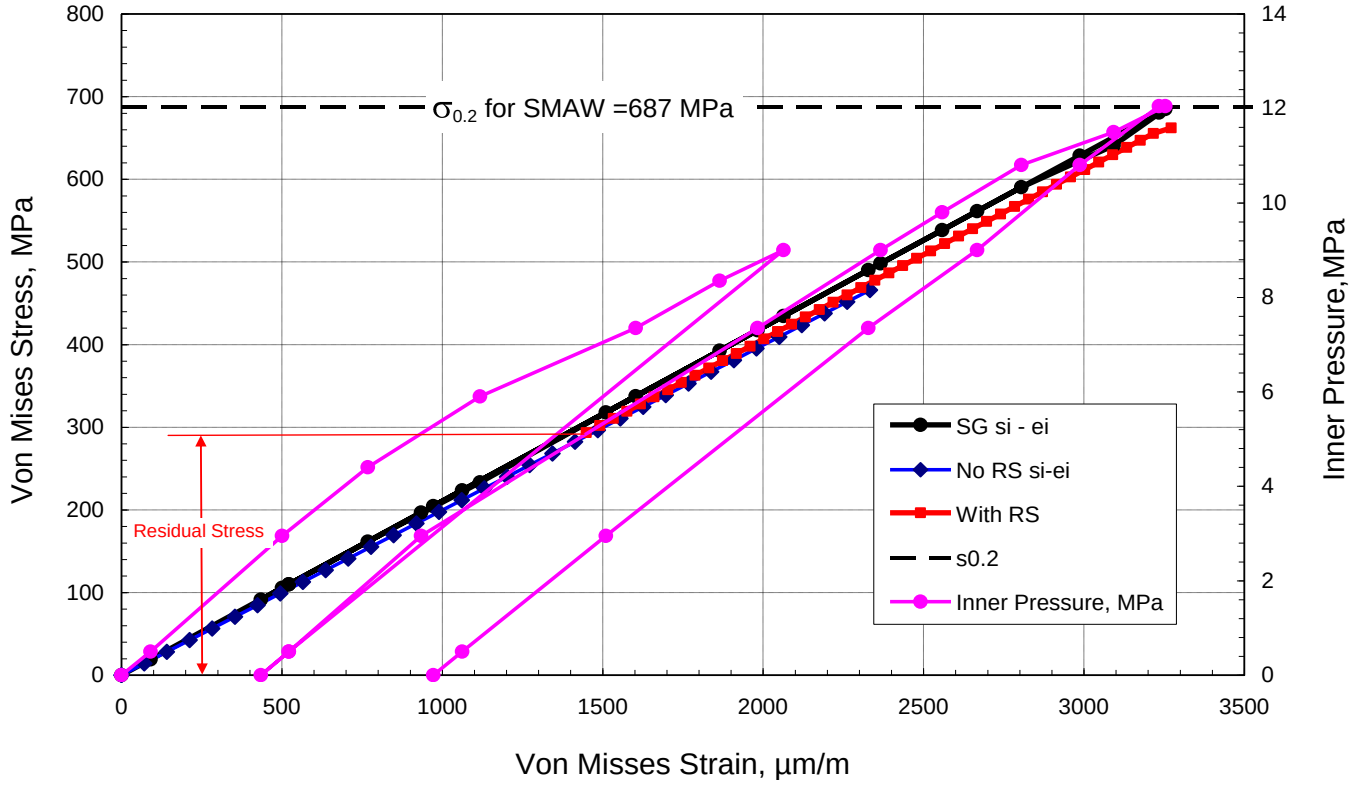

Figure 4-27. Von Misses Stress – Strain relationships for SMAW weld joint LS2

Because of the positioning of the two SMAW weld joints LS1 and LS2, it is easy to see the linear relationship of Stress – strain for the weld joint on the longer side of the upper cylinder of the penstock model and the plastic behavior of LS1 which is positioned on the lower side, Fig. 4-28. Weld joint LS2 has not reached the yield strength of the SMAW welded joint LS2.

After analyzing the upper cylinder of the penstock model, which is with a 5° deviation from the ideal cylinder geometry causing the additional stress concentration compared with the middle and lower cylinder of the model. Let us start with the SMAW joint L3 positioning on the similar side like SMAW L1.

Figure 4-29 shows the hoop strain response on the applied inner pressure in first and second loading sequence. According to the hoop strain readings one can conclude that Von Misses stress will reach the yield stress of the welded joint.

Figure 4-30 presents the Hoop stress – strain distribution for L3 SMAW joint together with the yield strength of weld metal. Hoop stresses after the inner pressure reached 9.8 MPa are higher than the yield stress of the SMAW weld metal.

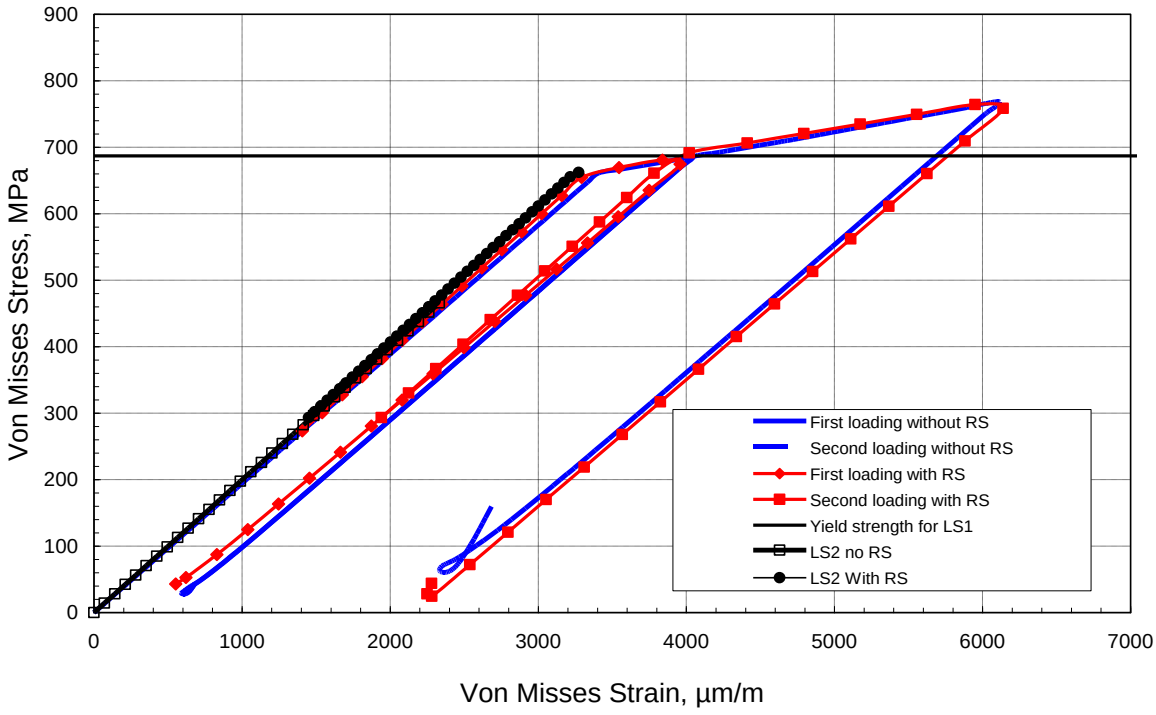

Figure 4-28. Comparison of Von Misses stress strain relationships for two SMAW joints LS1 and LS2

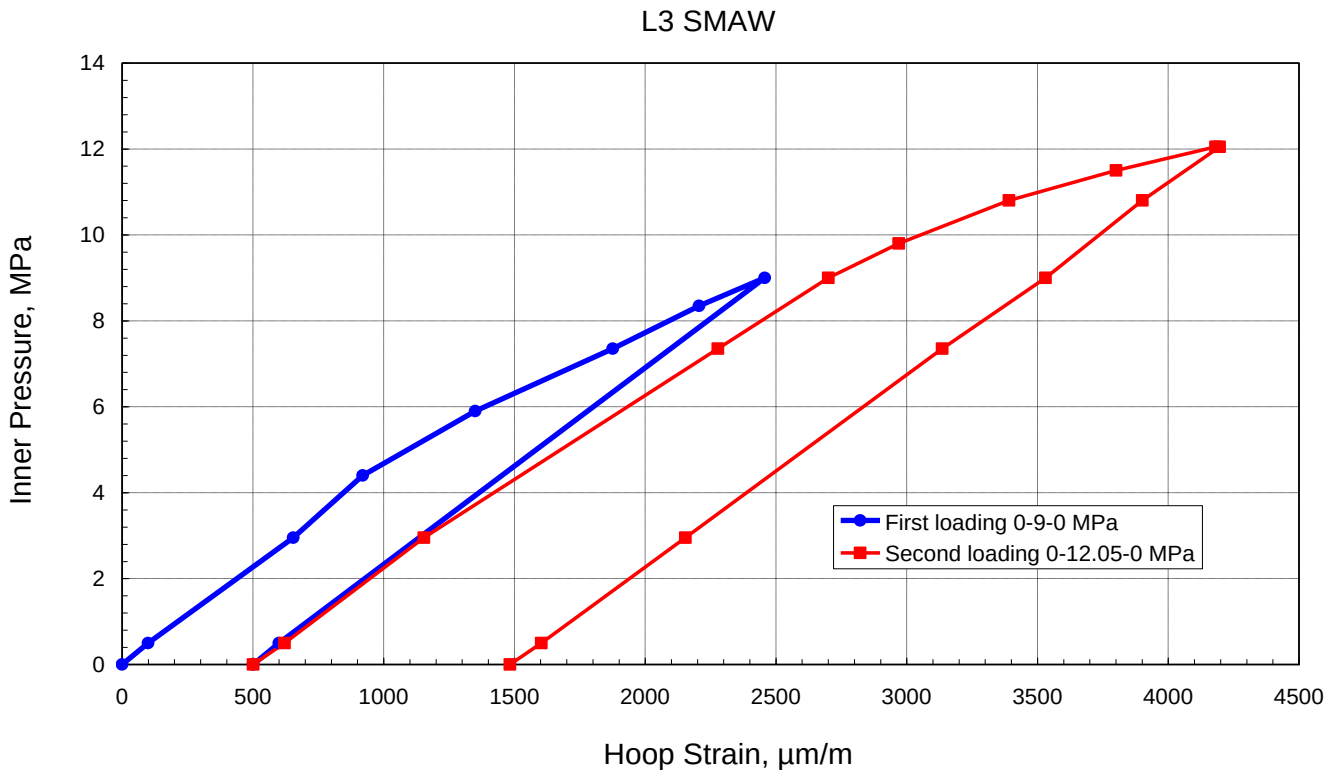

Figure 4-29. Hoop Strain against the applied inner pressure during both loading sequences

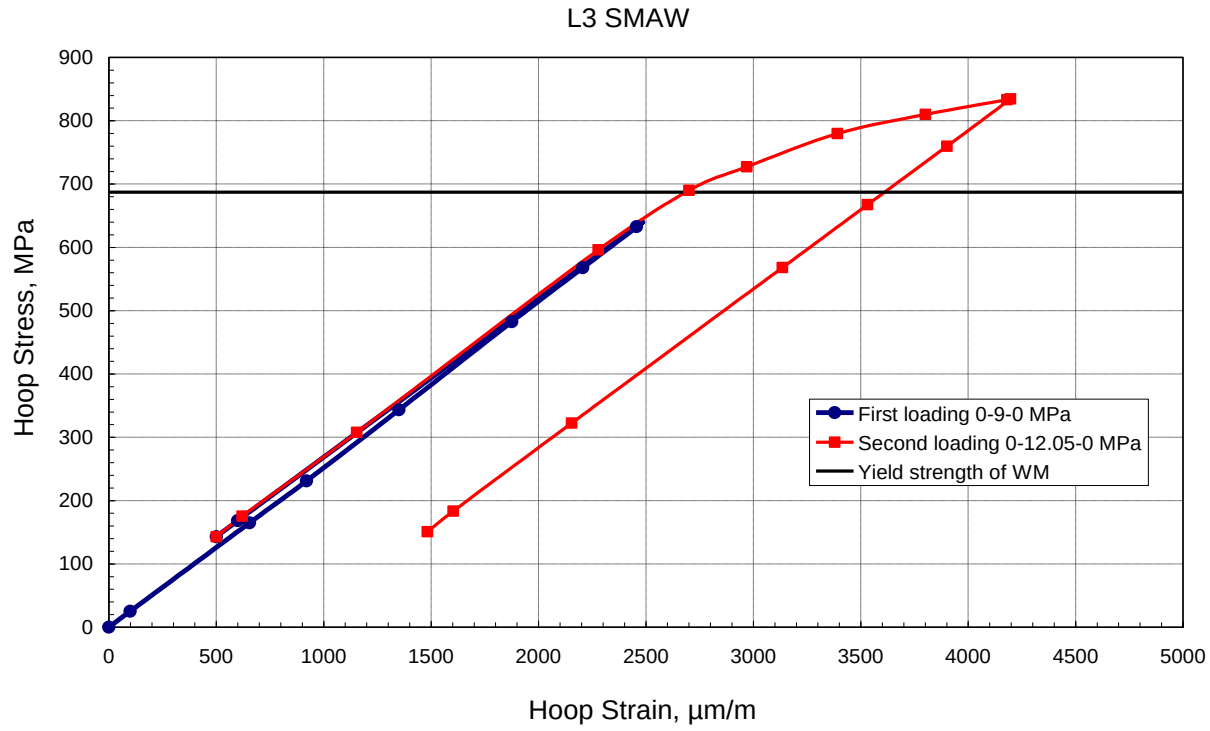

Figure 4-30. Hoop Stress – Strain distribution for L3 SMAW joint during loading in two sequences

In the figure 4-31 are presented Von Misses stress - strain distributions obtained from the SG readings together with the FE calculations. FE is taking into account initial residual stress of 293 MPa reaching the yield strength for inner pressure of 12.05 MPa. It can be concluded that there is good agreement reached between the calculations using SG readings and FE calculations using initial residual stress.

In fig. 4-32 the relationship between Inner pressure – Hoop strain for L4 MAW is given, in fig. 4-33 the relationship between Hoop Stress – Hoop strain for L4 MAW, in fig. 4-34 Von Misses Stress – Strain for L4 MAW, in fig. 4-35 the comparison between the welded joints stress–strain distribution in the second cylinder. As for the CM MAW circular weld joint, in fig. 4-36 the inner pressure vs. Hoop strains is given, in fig. 4-37 Hoop Stress vs. Hoop strains, in Fig. 4-38 Von Misses Stress vs. Hoop strains, together with FE calculations and in Fig. 4-39 Comparison of Von Misses Stress – Strain relationships for two circular weld joints.

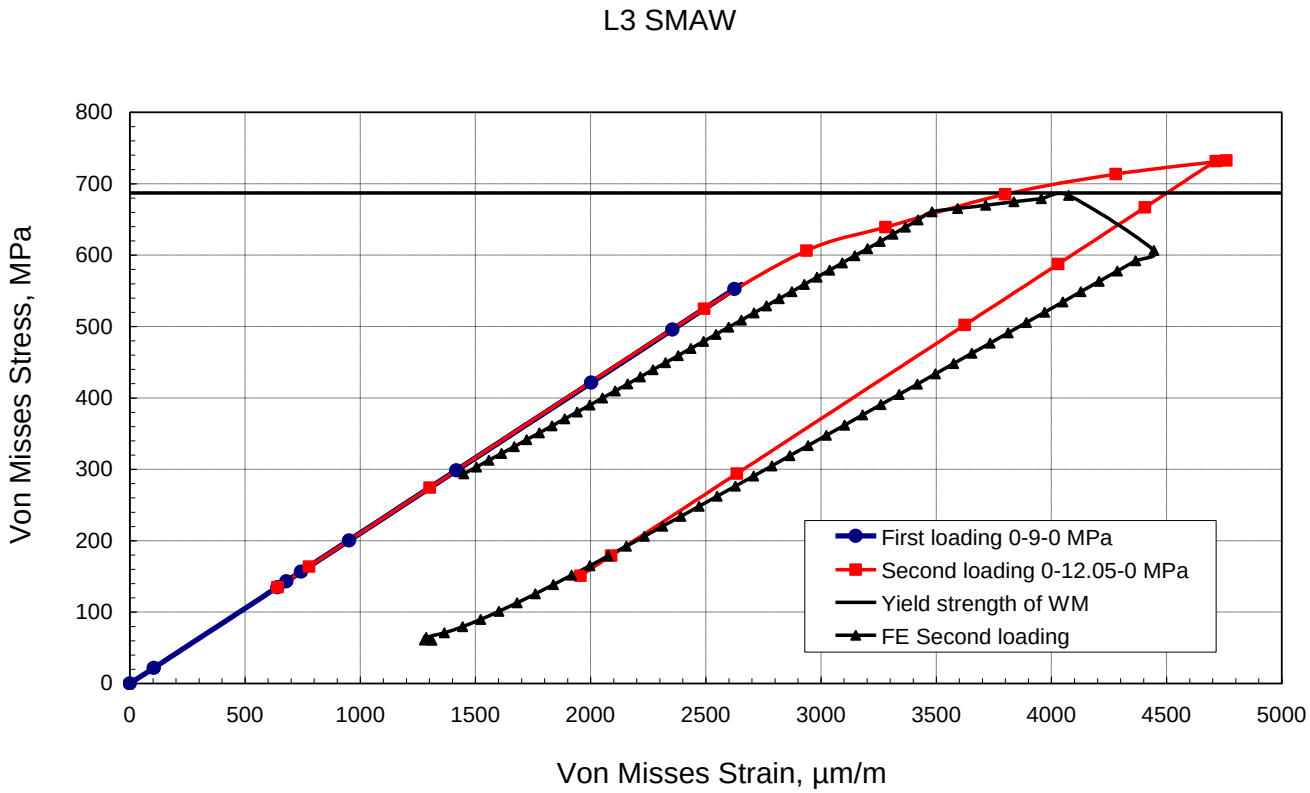

Figure 4-31. Von Misses Stress – Strain distribution for L3 SMAW joint compared with FE calculations

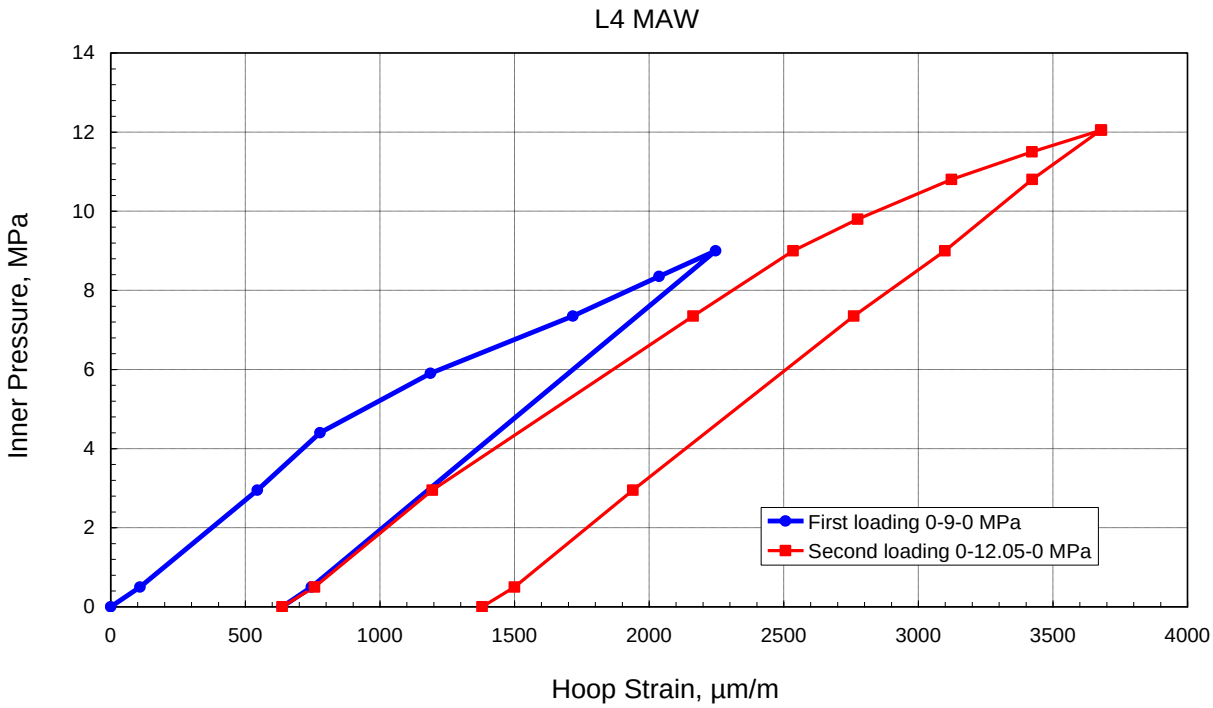

Figure (4-32), Inner pressure – Hoop strain for L4 MAW

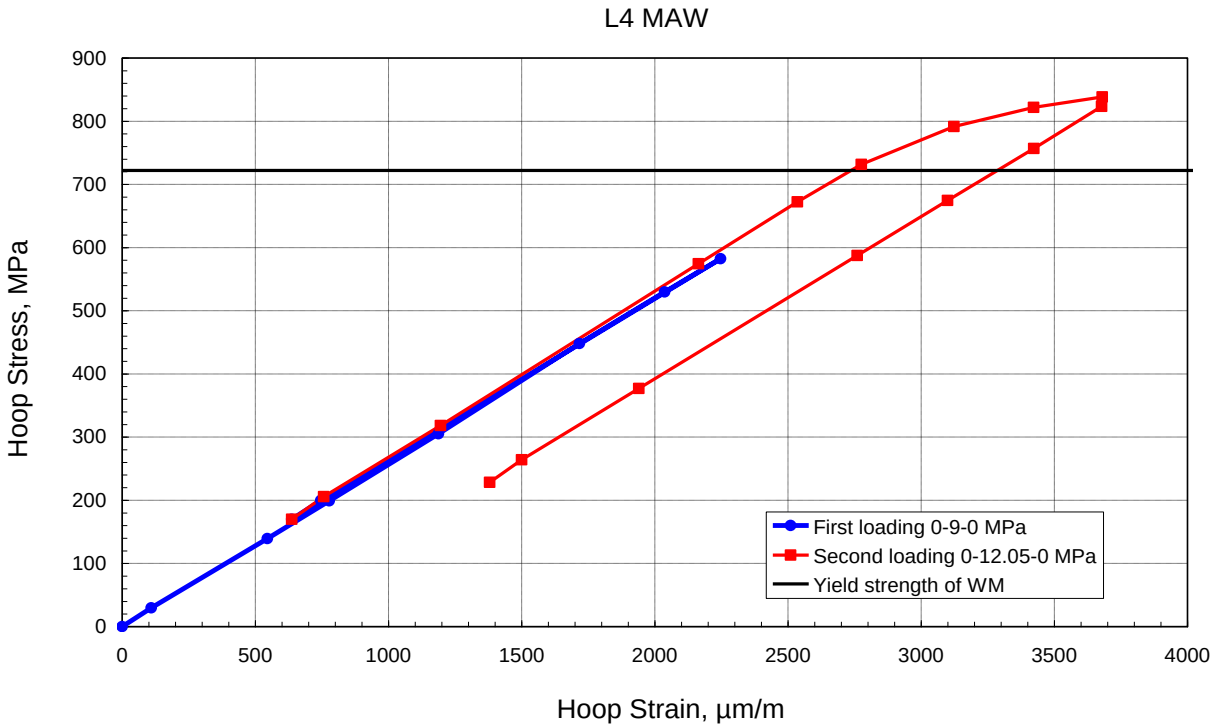

Figure 4-33. Hoop Stress – Hoop strain for L4 MAW

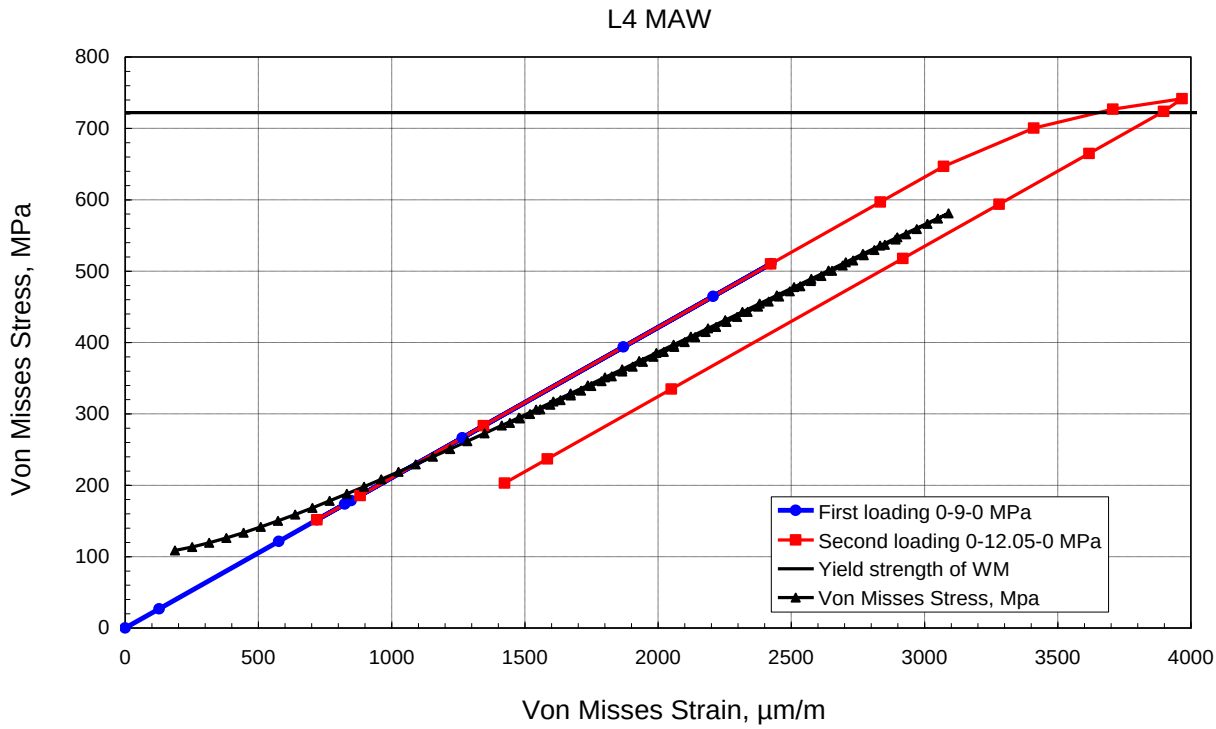

Figure 4-34. Von Misses Stress – Strain for L4 MAW

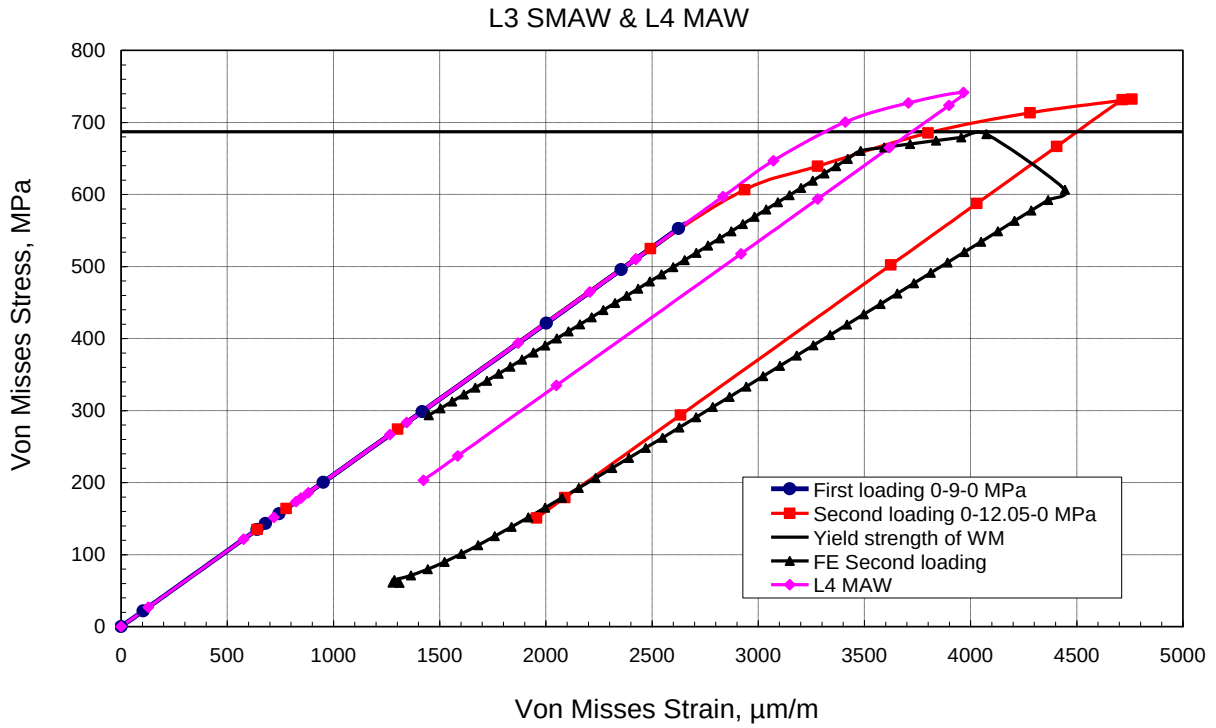

Figure 4-35. Comparison between the welded joints stress–strain distribution in the second cylinder

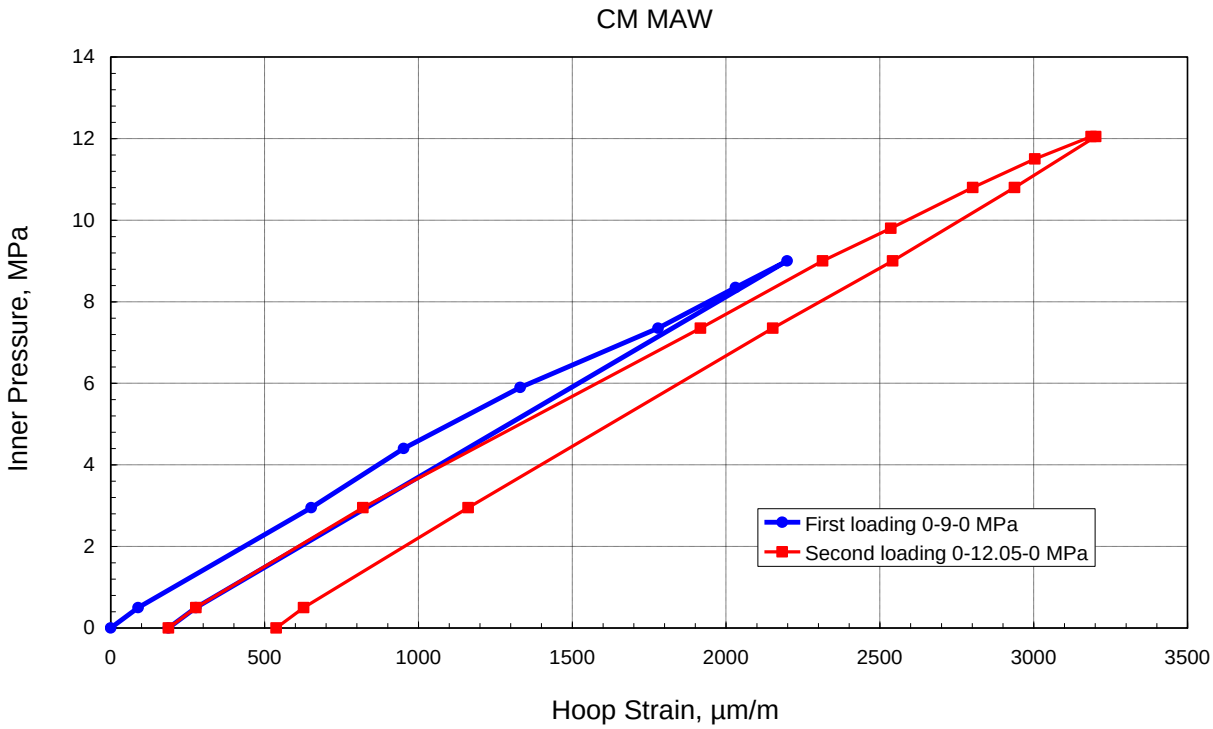

Figure 4-36. Inner pressure vs. Hoop strains for CM MAW circular weld joint

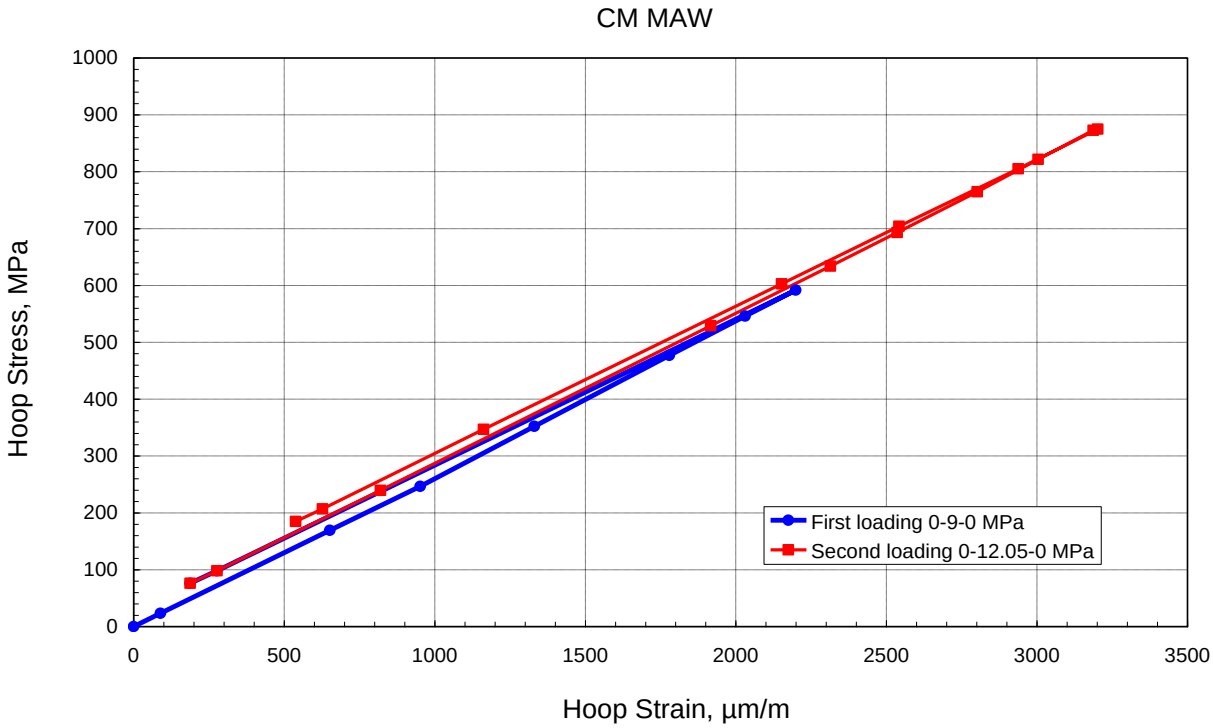

Figure 4-37. Hoop Stress vs. Hoop strains for CM MAW circular weld

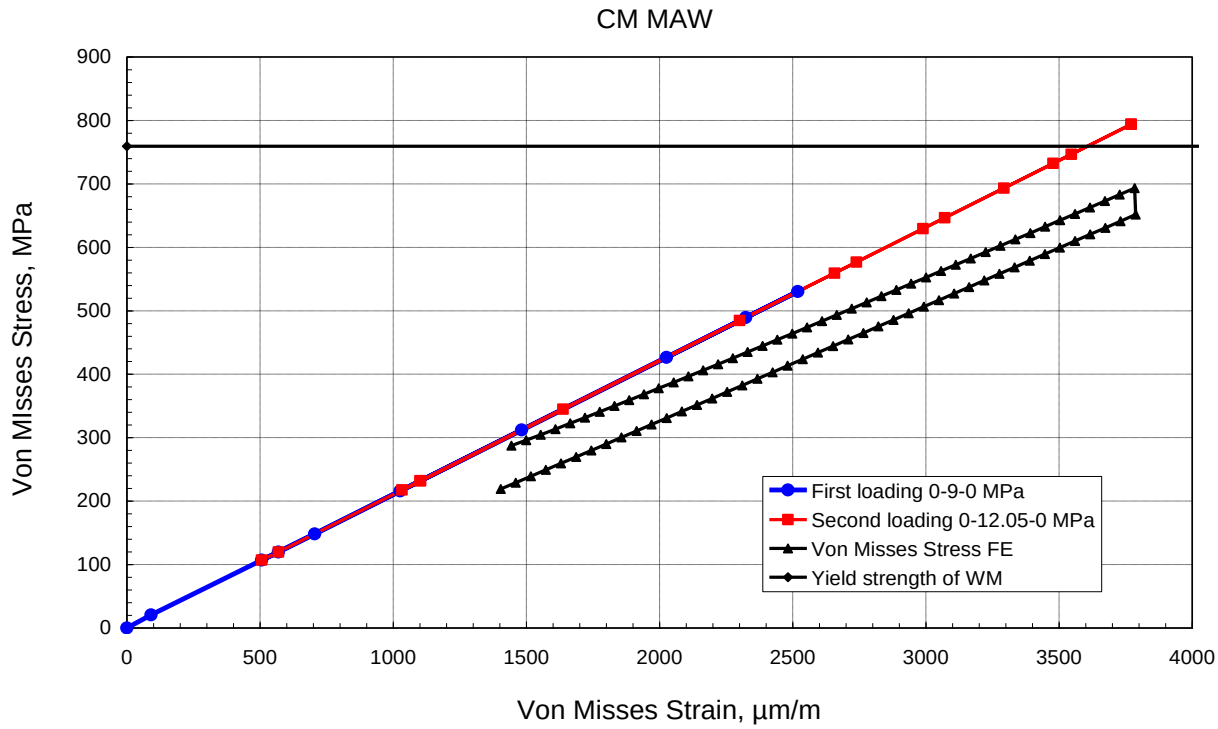

Figure 4-38. Von Misses Stress vs. Hoop strains for CM MAW circular weld together with FE calculations

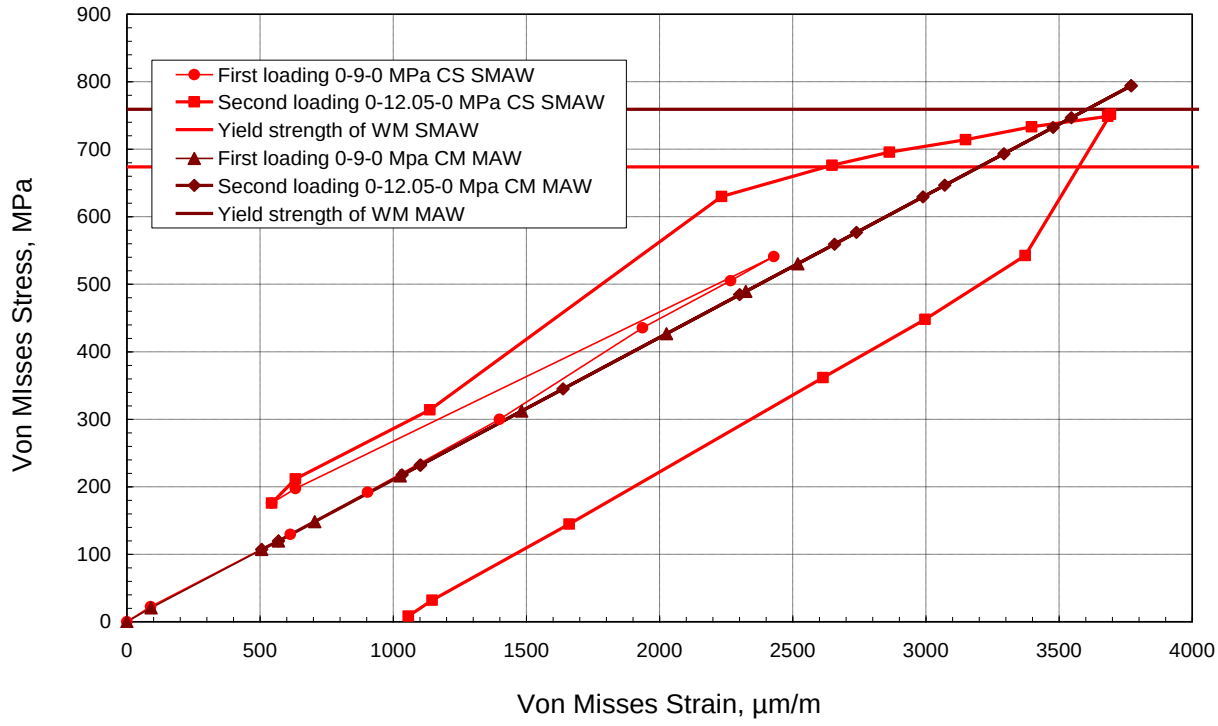

Figure 4-39. Comparison of Von Misses Stress – Strain relationships for two circular weld joints

5. Residual strength analysis by using fracture mechanics approach

Failure has occurred for many reasons, including uncertainties in the loading or environment, defects in the materials, inadequacies in design. Design against fracture has a technology of its own, and this is a very active area of current research.

The main modes of mechanical failure are:

- Failure in elastic deformation region (buckling)
- Failure after plastic deformation (yielding and necking)
- Failure by fast fracture (cracking)

Welded structures are only occasionally exposed to buckling, that can be prevented by convenient structural geometry. Failure by plastic deformation would occur when the applied stress was exceeding to the material's yield strength. To avoid this kind of failure the engineer follows a design code which ensures that the calculable stresses in his structure will not exceed the yield strength of materials.

The third type of modes of fracture has been produced by applied stresses less than the design stresses using safety factor. The structural integrity design requires consideration of factors that determine structural performance. It includes service environment, structural function, metallurgical properties, fabrication quality, inspection requirements, quality control, and factors that are specific to weldment. All of these factors interact with the fracture mechanics aspects because of their influence on crack size, stress and fracture properties. The knowledge and practical application of fracture mechanics are required in modern design.

The practical design use of fracture mechanics is highly dependent on experience which was evolved by structural integrity technology specialists. Engineering experience in the safe design of structures and in failure analysis is an important aspect for all practical application of fracture mechanics.

5-1. Linear elastic fracture mechanics

Linear elastic fracture mechanics (LEFM) is the basic theory of fracture, started by Griffith (1921-1942), [12], and completed in its essential aspects by Irwin (1957-1958), [13], and Rice (1968), [14]. Elastic theory deals with sharp cracks in elastic bodies, and is applicable to any material as long as certain conditions are met. These conditions are related to the basic ideal situation analyzed in which all the

material is elastic except in a small region (a point) at the crack tip. If the size of the plastic zone is small relative to the linear dimension of the body, the disturbance introduced by this plastic region is also small and, in the limit, LEFM is verified exactly.

5-1-1. Stress concentration

Definition of toughness began with the work of Inglis in 1913, [15]. Inglis showed that the local stresses around a corner or hole in a stressed platecould many times higher than the average applied stress. The presence of sharp corners, notches, or cracks serves to concentrate the applied stress at these points. Inglis showed that, the degree of stress magnification at the edge of the hole in the stressed plate depended on the radius of curvatureof the hole.The simplest case is defined as the Kirsch problem where different results are obtained for elliptic, square, rectangular, and other forms in a plate of finite size as well as for biaxial tension. For the elliptical hole in a flat plate Fig. 5-1, the stress at the tip of the major axis (A) is given by:

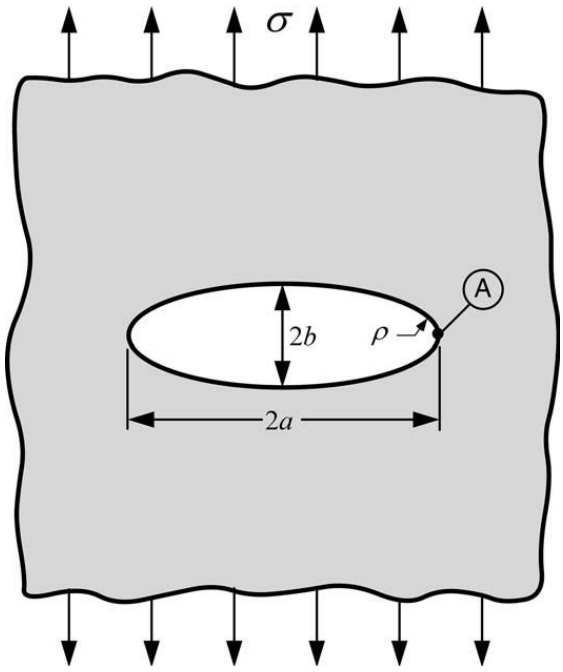

Figure 5-1. elliptical hole in flat plate, [16]

$$\sigma_A = \sigma(1 + \frac{2a}{b}) \quad (5\text{-}1)$$

$$\sigma_A = 2\sigma\sqrt{\frac{a}{\rho}} \quad (5\text{-}2)$$

Where: a –major axis of ellipse, b –minor axis, ρ –ellipse root radius ρ = $\frac{b^2}{a}$.

If minor axis tends to zero, normal stress will tend to infinity, and in elastically deformed material the condition for fracture is fulfilled.

5-1-2. Stress intensity factor

George R. Irwin became interested in the fracture of steel armor plating during penetration by ammunition, [17]. His experimental work at the U.S. Naval Research Laboratory in Washington, D. C. led in 1975 to a theoretical formulation of fracture that continus to find wide application. Irwin showed that the stress field $\sigma(r,\theta)$, Fig. 5-2, in the vicinity of a sharp crack tip could be discribed mathamatically by:

$$\sigma_{xx} = \frac{K_I}{\sqrt{2\pi r}} \cos\left(\frac{\theta}{2}\right)\left[1 - \sin\left(\frac{\theta}{2}\right)\sin\left(\frac{3\theta}{2}\right)\right] \quad (5\text{-}3)$$

The basic relationship for mode I crack growth between stress intensity factor ahead the crack tip (K_I), crack length (a) and applied stress (σ) is derived in term of coordinate (x , y , z) in crack surface direction:

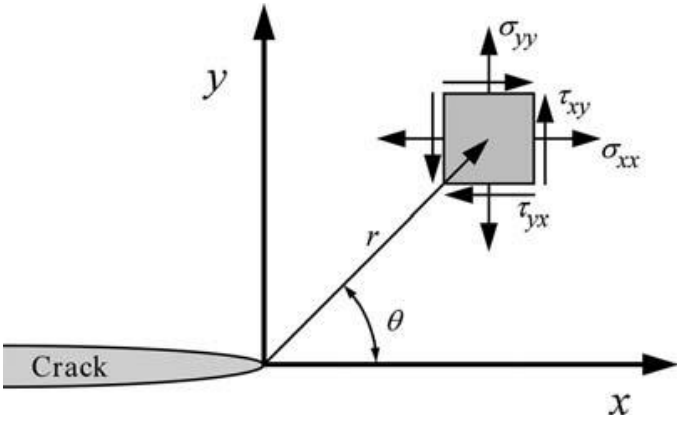

Figure 5-2. the stress field ahead of crack tip for mode I, [16]

$$\sigma_{xx} = \frac{K_I}{\sqrt{2\pi r}} \cos\left(\frac{\theta}{2}\right)\left[1 - \sin\left(\frac{\theta}{2}\right)\sin\left(\frac{3\theta}{2}\right)\right] \quad (5\text{-}4)$$

$$\sigma_{yy} = \frac{K_I}{\sqrt{2\pi r}} \cos\left(\frac{\theta}{2}\right)\left[1 + \sin\left(\frac{\theta}{2}\right)\sin\left(\frac{3\theta}{2}\right)\right] \quad (5\text{-}5)$$

$$\sigma_{zz} = v\,(\sigma_{xx} + \sigma_{yy}) \quad (5\text{-}6)$$

$$t_{xy} = \frac{K_I}{\sqrt{2\pi r}} \cos\left(\frac{\theta}{2}\right)\sin\left(\frac{\theta}{2}\right)\cos\left(\frac{3\theta}{2}\right) \quad (5\text{-}7)$$

$$t_{xz} = t_{yz} = 0$$

5-1-3. Energy balance criterion.

Inglis ‘s theory showed that the stress increase at the tip of a crack of flaw depeded only on the geometrical shape of the crack and not its absolute size, this seemed contrary to the well-known fact that large cracks are propagated more easily than smaller one. This fact led Griffith, [12], to a theoretical analysis of fracture based on the point of view minimum potential energy. Griffith proposed that the reduction in strain energy due to the formation of crack must be equal or greater than increase in surface energy required by the new crack face.

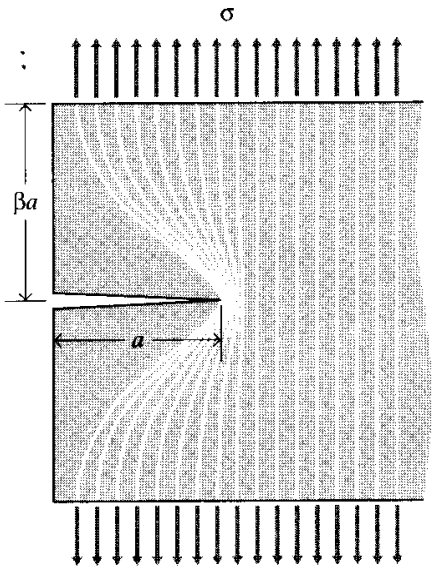

Figure 5-3.The unloaded area around free surface

The strain energy per unit volume of stressed material is:

$$U = \frac{1}{V}\int f\,dx \; ; V = AL \qquad (5\text{-}8)$$

$$U = \int \frac{f}{A}\frac{dx}{L} \; ; б = \frac{f}{A}$$

$$U = \int б\,d\epsilon \qquad (5\text{-}9)$$

If the material is linear, $(б = E\epsilon)$, then the strain energy per unit of volume is :

$$U = \frac{E\epsilon^2}{2} = \frac{\sigma^2}{2E} \qquad (5\text{-}10)$$

When a crack has grown into a solid to a depth (a), a region of material adjacent to the free surface is unloaded, and its strain energy released. Using the Inglis

solution, Griffith was able to compute just how much energy this is. The total strain energy being released is:

$$U = \frac{\sigma^2}{2E} . \pi a \tag{5-11}$$

In forming the crack, bonds must be broken, the surface energy needed to create two surfaces is:

$$S = 2\gamma a \tag{5-12}$$

The total energy is, Fig. 5-4:

$$W = U + S \tag{5-13}$$

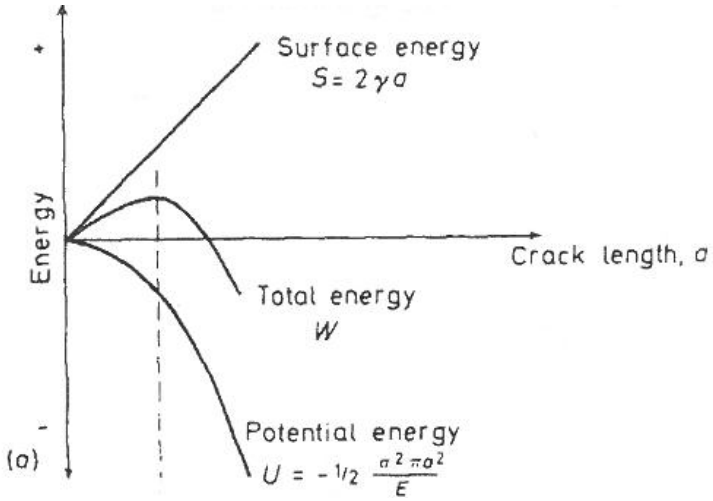

Figure.5-4 The fracture energy balance

The maximum in the total energy is given by, Fig. 5-4:

$$\frac{\partial w}{\partial a} = 0 \tag{5-14}$$

$$-\frac{\sigma^2 \pi a}{E} + 2\gamma = 0 \tag{5-15}$$

$$\frac{\sigma^2 \pi a}{E} = 2\gamma \tag{5-16}$$

For a given crack length a, the Griffith fracture stresses is given by:

$\sigma_f = \sqrt{\frac{2E\gamma}{\pi a}}$, in plane stress

$\sigma_f = \sqrt{\frac{2E\gamma}{\pi(1-\nu^2)a}}$, in plane strain

5-1-4. Fracture modes

Irwin and Orowan have shown that, three modes of crack surface displacement are possible, Fig. 5-5, and they describe crack behavior in all stress states, but our interest centers mainly on the type I loading, the most common type that lead to brittle failure.

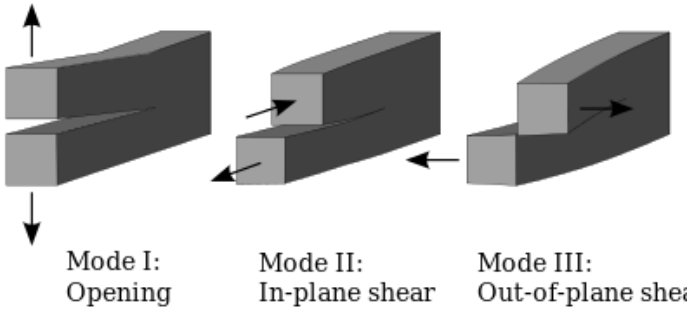

Figure 5-5. Three fracture modes.

5-1-5. Crack tip plastic zone

The stress at crack tip is limited at least the yield strength of the material, and hence linear elasticity can not be assumed with a certain distance of the crak tip. This non linear region is some times called “crack tip plastic zone“. For the ideally elastic mode I opening stress distribution in the crack plane ($\theta = 0$) and in the K dominant region is:

$$\sigma_y = \frac{K_I}{\sqrt{2\pi r}} \qquad (5\text{-}17)$$

The elastic analysis becomes inaccurate as the plastic zone ahead of crack tip grows. The size of this region can be astemited by the Irwin method. The stress in linear elastic material is given by eq. (5-17). As the first approximation, we can be assume that, the boundary condition between ealstic and plastic behavior starts when ($\sigma_Y = \sigma_{YS}$), Fig. 5-6, then the first order estimate of plastic zone is:

$$r_Y = \frac{1}{2\pi}\left(\frac{K_I}{\sigma_{YS}}\right)^2 \text{ for plane stress} \qquad (5\text{-}18)$$

$$r_Y = \frac{1}{6\pi}\left(\frac{K_I}{\sigma_{YS}}\right)^2 \text{ for plane strain} \qquad (5\text{-}19)$$

Second order estimates of the plastic zone size (r_p):

$$r_p = \frac{1}{6\pi}\left(\frac{K_I}{\sigma_{YS}}\right)^2 \qquad (5\text{-}20)$$

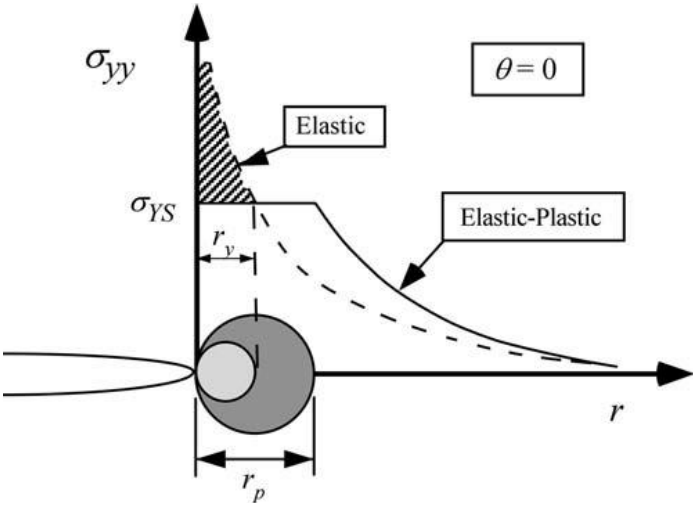

Figure 5-6. The first order and second order estimates of plastic zone (r_y, r_p)

5-1-6. The strip yield model

The strip model proposed by Dugdale and Barenbatt [18] among others estimates the size of the yield zone ahead of crack tip in a thin plate (plane stress) of elastic perfectly plastic material. Two elastic solutions are superimposed; one through a crack in an infinite plate under remote tension, and the other through a crack with closure stress at crack tip, as in figure 5-7.

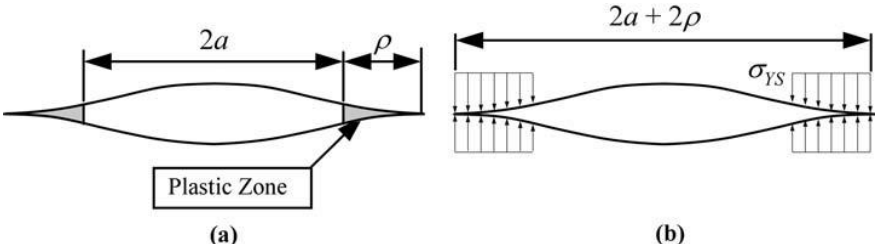

Figure 5-7. The strip yield model, [16]

The model assumes that, along the slender plastic zone at the crack tip with length r_p, i.e. the total crack length is $2a + 2r_p$. The stress over r_p is σ_{YS}, and since the stress finite is in the plastic zone, there can not be singularity at the crack tip. This is accomplished by choosing the plastic zone length such that the stress intensity factor from the remote tension and closure stress cancel each other out. This leads to:

$$r_p = \frac{\pi}{8}\left(\frac{K_I}{\sigma_{YS}}\right)^2 \qquad (5\text{-}21)$$

5-1-7. Crack resistance

The assumption that all strain energy is available for surface energy of new crack faces does not apply to aductile material where other energy dissipative mechanisms exist. Orowan, [19], modified Griffith‘s equation to take into account the non-reversible energy mechanisms associated with the plastic zone by simply including this term in the original Griffith ‘s equation:

$$\frac{dU_S}{dC} = \frac{dU_\gamma}{dC} = \frac{dU_P}{dC} \qquad (5\text{-}22)$$

The right hand of eq (5-22), is also given the symbol R and called the crack resistance. The crack resistance indicates the minimum amount of energy required for crack extension. The enenrgy is called the “ work of fracture “, which is the measure of toughness.

Ductile materials are tougher than brittle materials because they can absorb energy in a plastic zone. By contrast, brittle material can only dissipate stored elastic strain energy surface which are created.

5-1-8. The K_{IC} – the critical value *o*f K_I

The stress intensity factor is K_I a “scale factor“, which charactertizes the magnitude of the stress at some coordinates ($\theta = 0$) near the crack tip (theoretically infinite for perfectly elastic materials but limited in practice by plastic deformation), the value of K_I at the of crack extension is called the critical value: K_{IC}, and defines the onset of the crack extension. It does not necessarily indicate fracture of specimen, this depends on the crack stability. Anyhow, catastrophic fracture may occur when the equilibrium condition is unstable.

5-2. The elastic-plastic fracture mechanics

Many of the engineering applications of fracture mechanics have been centred around linear-elastic fracture mechanics (LEFM). This concept become inappropriate when ductile material is used. Much experimention and analytical effort has been devoted to the development of the elastic plastic fracture mechanics (EPFM) concept. Many EPFM assess the toughness of metallic materials to predict failure of cracked structural components.

Two alternative parameters charactarizing the state at a crack tip are well established in elastic plastic fracture mechanics (EPFM). The first one is the J integral proposed by J.R.Rice, [14], which represents the intensity of stress or strain rather than the energy release rate. The second one is the crack tip opening displacement (CTOD) δ_t as a measure of the state of deformation at crack tip, which dates back to A.H.Cottrell and A.A. Wells, [20].

5-2-1. The crack tip opening displacement (CTOD)

This parameter of fracture toughness was developed by Wells, [20], who discovered that several structural steels could not be characterized by linear elastic fracture mechanics (LEFM), i.e. K_{IC} was not applicable. He also discovered while examining the fracture surface that the crack surface moves apart prior to fracture. Plastic deformation precedes the fracture and the initially sharp tip is blunted. The plastic deformation increase with increasing fracture toughness , and Wells proposed that the opening at crack tip asa fracture toughness parameter. The CTOD has no unique definition, so figure 5-8 shows two different definitions of the COTD.

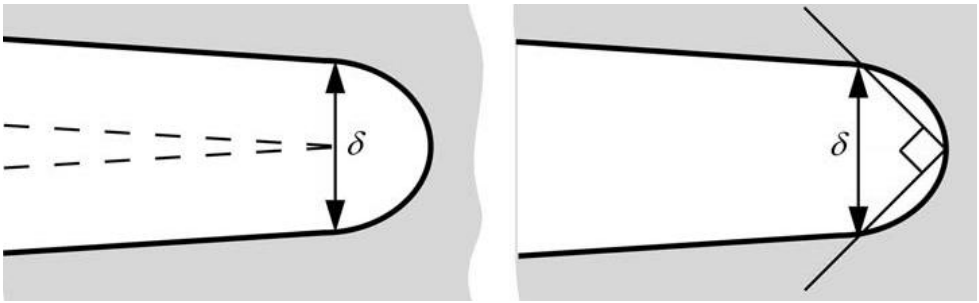

Figure 5-8. The alternative definition of CTOD, left - displacement at original crack tip right - displacement at the intersection of a 90º vertex with the crack flanks, [16]

When the crack tip is plastically deformed, the crack behaves as if it is longer than the actual crack tip. This is shown by Irwin, [17]. It possible to estimate the crack tip opening displacement in the small scale yielding (SSY), figure 5-9.

The plastic zone correction according to Irwin, as given by eq. (5.18), and combined with the elastic solution for the displacement of the crack surface in plane stress:

$$u_y = \frac{k+1}{\mu} K_I \sqrt{\frac{r_y}{2\pi}} \qquad (5\text{-}23)$$

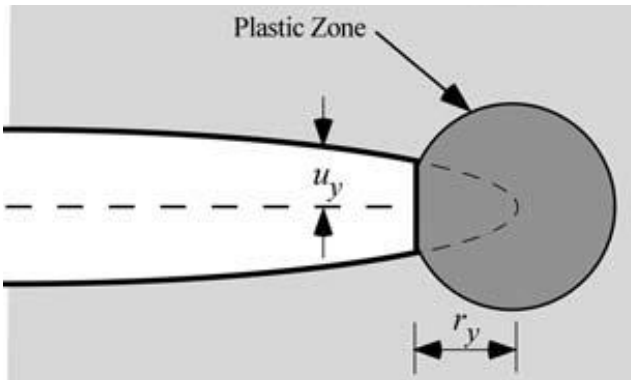

Figure 5-9. The CTOD in the Irwin plastic zone correction,[16]

This gives the CTOD for a stationary crack in small scale yielding

$$CTOD = 2u_y \frac{4K_I^2}{\pi\sigma_Y E} \tag{5-24}$$

The strip model provided an alternative analyzing for crack tip opening displacement, [21]. Crack tip opening can be defined at the end of strip-yield zone as illustrated in figure 5-10.

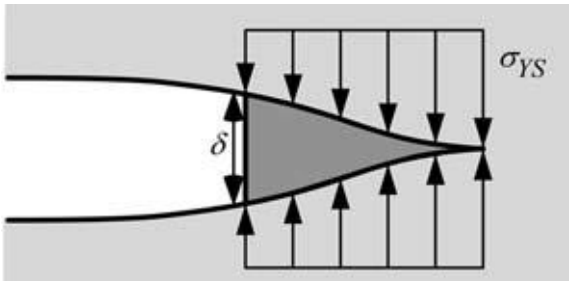

Figure 5-10. Estimation of CTOD from strip yield model, [16]

By choosing the plastic zone length such that, the stress intensity factor from the remote tension and closure stress cancel each other. This leads to already given expression r_p, namely eq. 5-21.

The CTOD from the strip model can be derived at the crack tip, by superposion of the crack surface displacement. The CTOD become:

$$CTOD = \frac{8\sigma_{YS}}{\pi E} \ln \sec\left(\frac{\pi\sigma}{2\sigma_{YS}}\right) \tag{5-25}$$

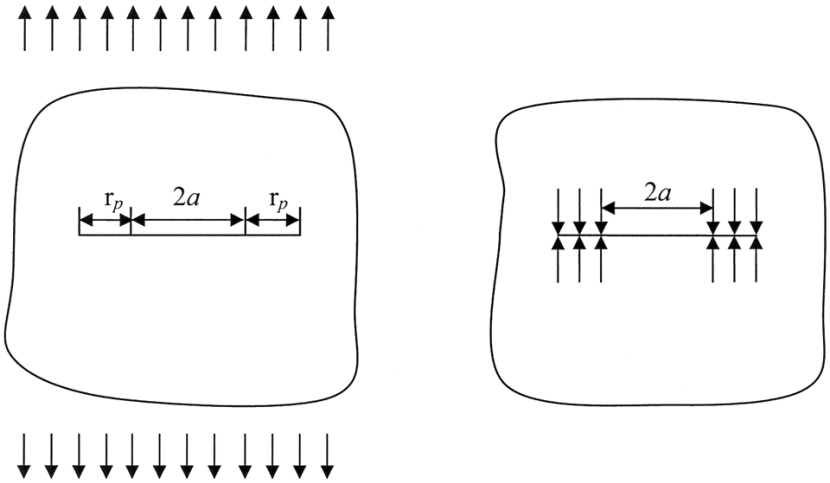

Figure 5-11. superposition of two load cases for the Dugdal model, [16]

A series expansion of the logarithmic term in eq. (5-25), and truncating all, but first two terms gives (zero will be obtained if only one term is included)

$$CTOD = \frac{\pi^2 \sigma^2 a^2}{8\sigma_{YS}} = \frac{K_I^2}{\sigma_{YS} E} \qquad (5\text{-}26)$$

the $CTOD$ from the strip model differs only slightly from eq (5-16), given by the Irwin model.

5-2-2. The J contour integral.

The J contour integral introduced by Rice [14]. As a fracture characterizing parameter for non-linear materials, figure 5-12 shows uniaxial stress-strain behavior of elastic-plastic material and nonlinear material.

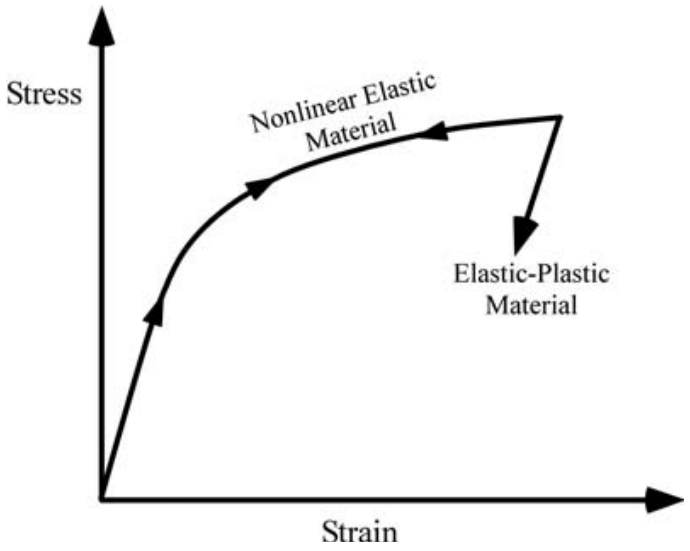

Figure 5-12. The stress-strain behavior of non-elastic material [16]

An analysis assumes that non-linear elastic behavior may be valid for elastic-plastic material. Rice applied deformation plasticity to the analysis of crack in a non-linear material. He showed that the non-linear energy release rate J could be written as a path-independent line integral. Hutchinson, [22], and Rice and Rosengren, [23], also showed that J uniquely characterizes crack tip stresses and strain in non-linear material. Other aspects of J integral application is given in [24-26].

5-2-3. J as path-independent line integral

Rice developed a powerful mathematical device, namely line J integral, to descrlbe the energy flow into the crack tip per unit fractured area, its given by:

$$J = \int_{\Gamma}(wdy - T_i \frac{\partial u_i}{\partial x} ds) \qquad (5\text{-}27)$$

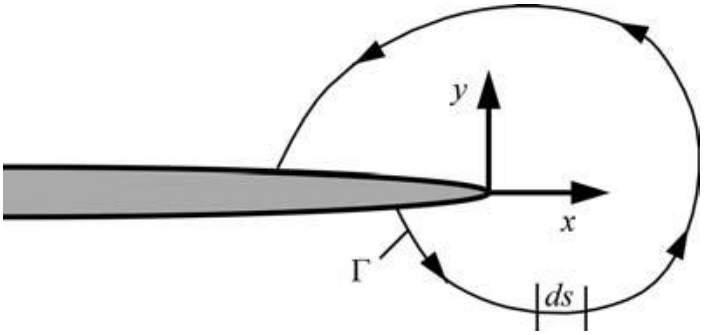

Figure 5-13. Arbitrary contour around the tip of crack

where w = strain energy density, T_i = components of the traction vector, u_i = displacement vector components, ds = length increment along the contour Γ.

The strain energy density is defined as:

$$w = \int_0^{\varepsilon_{ij}} \sigma_{ij} d\varepsilon_{ij} \qquad (5\text{-}28)$$

where $\sigma_{ij}$and ε_{ij} are the stress and strain respectively. The traction is a stress vector at a given point on the contour. That is, if we were to construct a free body diagram of material inside inside of the contour, T_i would define the stress acting at the boundaries. The components of traction vector are given by:

$$T_i = \sigma_{ij} n_j \qquad (5\text{-}29)$$

where n_j are the components of unit vector normal to Γ. Rice showed that the value of the J integral is independent of the path of integration around the crack tip.

5-3. Structural integrity assessment of the pressure vessel

Fracture mechanics-based structural integrity assessment or fitness-for service (FFS) is not a new concept. The nuclear and offshore oil and gas industries were the main drivers behind the development of the FFS procedure. Fracture mechanics methods have been used to assess the structural integrity of pressure equipment for many years. Fracture describes a failure mechanism that involves the propagation of a crack. How that crack propagates depends on three variables: flaw size, material properties and stress state at the region of the flaw.

Irwin‘s stress intensity approach fracture occurs when the stress intensity factor at the crack tip exceeds the material fracture toughness. Linear elastic fracture mechanics introduce the concept of a stress intensity factor K. For ductile materials, the local stress-state close to the crack tip is such that plasticity occurs, and when this is significant, then K is no longer appropriate and means to account for plasticity at crack tip. Additional parameters are required to characterize fracture toughness, such as the crack tip opening displacement (CTOD,δ) which is a strain based parameter, and the J-integral which is energy based parameter.

Fitness-for–service is performed after a defect or crack has been found following routine inspection, maintenance or safety check, or when the effect of an undetected crack needs to be considered. The assessment determines whether the pressure vessel is safe to operate with the defect or to establish inspection intervals for monitoring the defect. If the defect size is unacceptable, then the user must be decided whether to repair it, or replace the equipment.

5-3-1. Failure Assessment Diagram approach (FAD)

A failure assessment diagram represents a two-parameter approach. For fracture to occur the stress intensity factor at crack tip must be greater than the material toughness or critical stress intensity factor (K_{IC}). However, plastic collapse can also occur if the stress is high relative to the ultimate tensile strength (UTS) of material. A typical failure assessment diagram is shown in figure 5-14.

A vertical axis of the failure assessment diagram represents the criteria for brittle or ductile fracture, often known as the fracture toughness ratio (K_r) which is the ratio of stress intensity factor (K_I) to material fracture toughness (K_{IC}). The horizontal axis represents the likelihood of plastic collapse, often known as the load ratio (L_r).

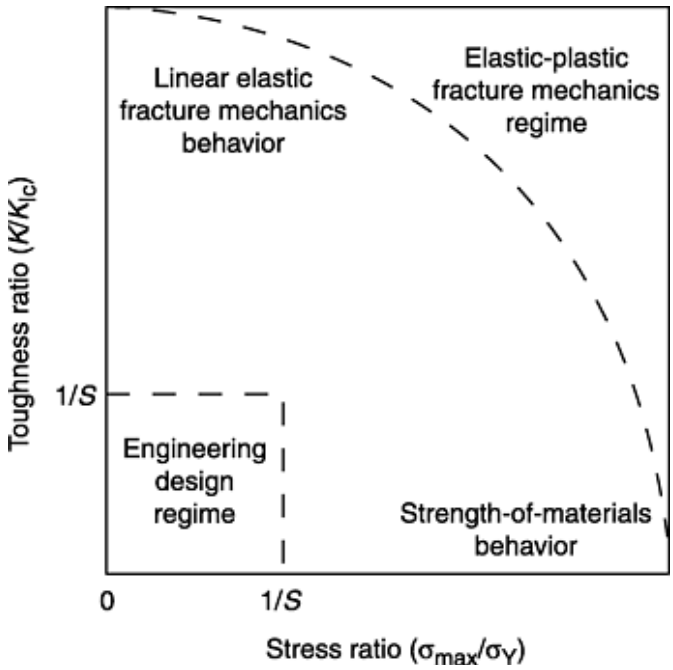

Figure 5-14. The failure assessment diagram FAD

5-3-2. R-Curve approach

In order to construct R-curve for a material, where a toughness parameter such as K, J, or (CTOD) is plotted against the crack extension, a fracture toughness test is performed to measure the resistance of material to a crack extension. A variety of organizations publish standardized procedures for fracture toughness measurement, including the American Society for Testing and Materials (ASTM) and the British Standards Institution (BSI).

There are five types of specimens that are permitted in ASTM standards which characterize fracture initiation and crack growth, the configurations that are currently standardized include the compact tension (CT) specimen, the single-edge notch bend (SEN (B)) geometry, the arc shaped specimen, the disk specimen and the middle tension (MT) panel. Figure 5-15 shows CT and SEN(B) specimen type.

5-3-3. The standard K_{IC} testing

When a material behaves in a linear elastic manner prior to fracture, such that the plastic zone is small compared to the specimen dimension, a critical value of the mode I stress intensity factor K_{IC} may be an appropriate fracture parameter. ASTM-399 [27] was the first standard test method for K_{IC} testing, other K_{IC} testing was British Standard 5447 [28], generally based on ASTM-399.

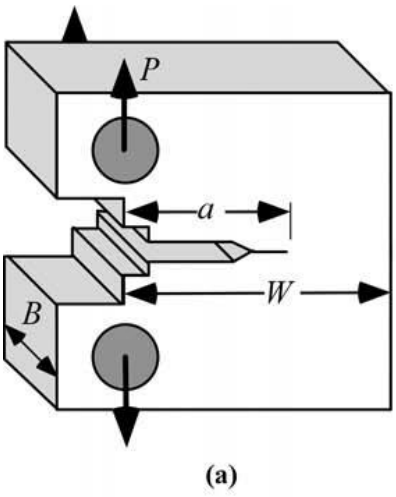

Figure 5-15a. The standard fracture mechanics compact specimen

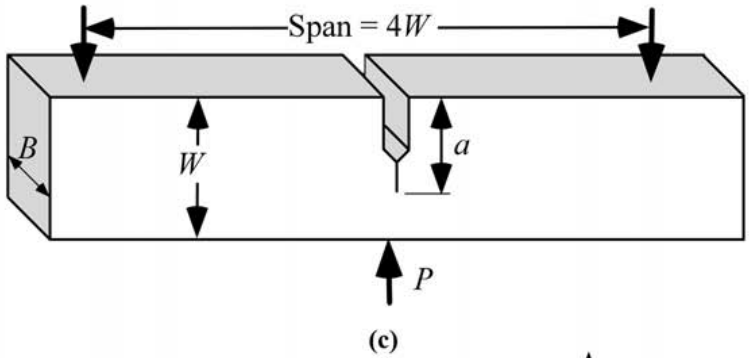

Figure 5-15b. The standard fracture mechanics single-edge-notch bend specimen

Displacement and load are monitored during the test of pre-cracked specimen until the fracture of specimen. The critical load P_Q was defined in several ways depending on the type of curve, Fig. 5-16:

- CurveI, load-displacement behavior is smooth and deviates slightly from linearity. This non-linearity could be caused by plasticity, or subcritical crack growth, or both.
- Curve II, a small amount of unstable crack growth occurs before the curve deviates from non- linearity.
- Curve III, behavior fails completely before achieving 5% of non-linearity.

The crack length must be measured from the fracture surface [5].

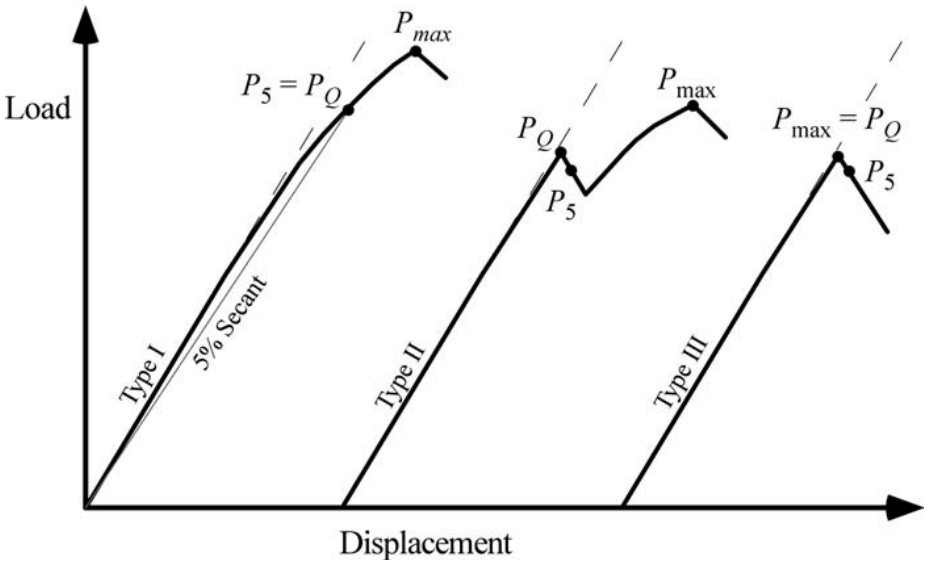

Figure 5-16. Three types of load- displacement behavior in K_{IC} test [5].

According to ASTM-399:

$$K_Q = \frac{P_Q}{B\sqrt{W}} f(a/w) \quad (5\text{-}30)$$

Where:

$f(a/w)$= dimensionless function of a/w

W= width of the specimen

B= thickness of specimen

a= crack length

The K_Q computed from equation (5-30) is a valid K_{IC} result if

$$0.45 \leq a/W \leq 0.55 \quad (5\text{-}31a)$$

$$B, a \geq 2.5\left(\frac{K_Q}{\sigma_{YS}}\right)^2 \quad (5\text{-}31b)$$

$$P_{max} \leq 1.1 P_Q \quad (5\text{-}31c)$$

5-3-4. The J_{IC} testing

In order to construct J-R curve, ASTM standard E 1820 [29], and the British standard BS 7448: part 1 [30] are suggested and they cover this test. There are two alternative methods of J testing provided by ASTM standard E 1820:

- Basic procedure: this method performs by monotonically loading the specimen until fracture or to a certain displacement.
- Resistance curve procedure: in this procedure the growth of crack monitored during the test.

To construct R-curve it is convenient to divide the J into elastic component and plastic as follows according to ASTM E1820:

$$J = J_{el} + J_{Pl} \quad (5\text{-}32)$$

$$J_{el} = K^2 \frac{(1-v^2)}{E} \quad (5\text{-}33)$$

$$K = \frac{P}{B\sqrt{W}} f(a/w) \quad (5\text{-}34)$$

If side groove specimen are used, then

$$K = \frac{P}{\sqrt{BB_N W}} f(a/w) \quad (5\text{-}35)$$

ASTM E 1820 including a simplified method for computing J plastic from area under load-displacement curve:

$$J_{pl} = \frac{\eta A_{pl}}{B_N b_o} \quad (5\text{-}36)$$

Where:

J_{el} = elastic component of J, J_{pl} = plastic component of J, K = stress intensity factor, v = Poisson‘s ratio, E = Young‘s modulus, b_o= the initial ligament length, η = dimensionless constant.

5-3-5. J-R Curve

The most common single-specimen test technique is the unloading compliance method, which is illustrated in figure 5-17. The crack length is computed at regular intervals during the test by partially unloading the specimen and measuring the compliance. As the crack grows, the specimen became more compliant (less stiff).

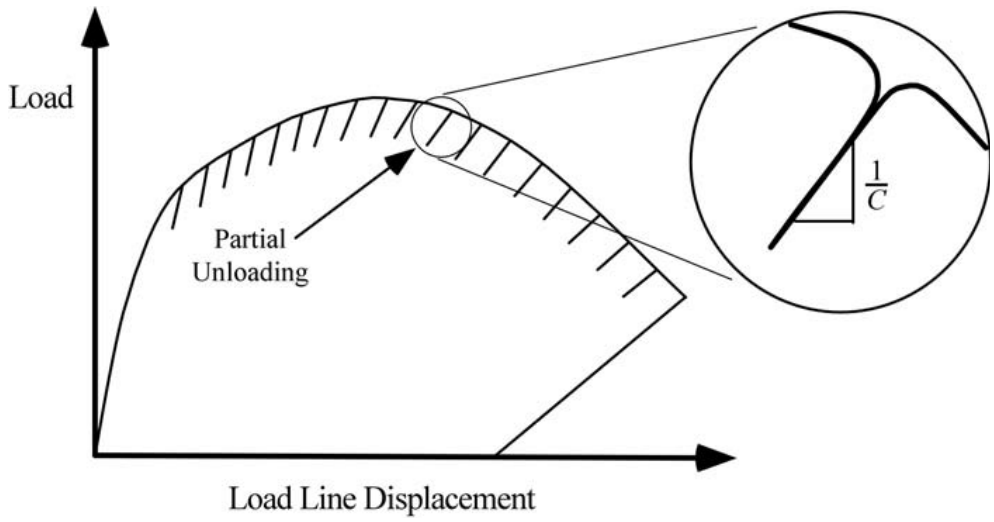

Figure 5-17. The compliance method for J-R curve

5-4. Residual strength prediction of penstock

Safe life prediction of structural components is the main consideration for designing; pressure vessel should be able to sustain the design load (inner pressure) during its life time, where most structural components contain defects (flaws).

A serious structural problem that arises in the pressure vessel is the delayed time failure of pressure vessel due to sustained pressurization, even with inert environments. Failure can occur after only a few operational pressure cycles. In some cases through-thickness cracks have formed, and the vessel leaked under pressure. In other cases, small surface cracks grow to a critical size prior to becoming through-thickness flaw, resulting in a catastrophic failure. The significant parameters affecting the critical flaw size are applying stress level, the properties of material (fracture toughness), and the wall thickness of pressure vessel and the location of flaw. In order to predict the growth of flaw in pressure vessel using fracture mechanics, elastic stress intensity factors for brittle material , or using J integral and crack opening displacement of ductile materials.

5-4-1. Evaluation of critical crack size of surface flaw (point of instability)

In order to predict the residual strength of surface flaw by using a resistance curve of material and crack driving force curve of structure, the following proposed procedures are used:

Consider surface flaw geometry as shown in figure 5-18, where: (d) the depth of crack at the center, (2a) the length of surface.

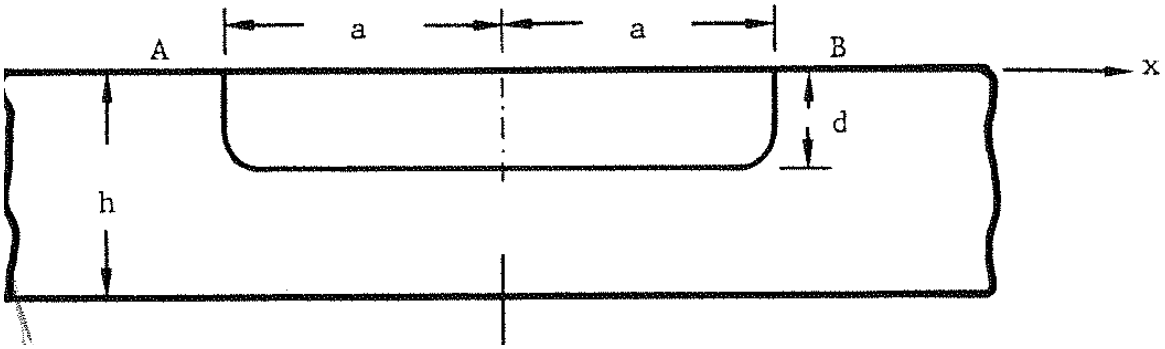

Figure 5-18. The surface flaw geometry

Procedure is as follows:

1 - Construct the $\sqrt{J_R}$ curve of the material of the structure using suitable specimen.

2 – Construct $\sqrt{J*}$ curves for the structure at various crack depths and applied stress using a suitable model.

3 - Determine the point of instability, which defined at the point of tangency between the crack driving force curves and J-R curve.

5-4-2. Experimental procedure

The approach to welded structure designs is that the weld metal strength under matches the strength of the base metal. This means that the yielding will start in weld joint, and the base metal will start to yield when the strength of weld joint reaches (strain hardening) a level of base metal yield strength.

In these experiments the Sumiten 80P (SM 80P) grade steel plate (16 mm thick) was butt welded (X-shaped preparation) by submerged arc welding using consumables of 80B wire and MF38 flux, where these combinations under-matched weld joints are obtained. Three tensile panels with surface cracks positioned in the base metal (BM), weld metal(WM),and heat-affected zone (HAZ) were tested at room temperature. A semi-elliptical small and large surface crack (SSF, d = 2.5 : 3 mm, LSF, d = 4.5 : 5 mm) was produced by electrical discharge machine at BM, WM, and HAZ.

The objective of this was to induce stable crack extension, and this test requires continuous measurement of force versus crack mouth opening displacement and crack extension was monitored during the test by the compliance method.

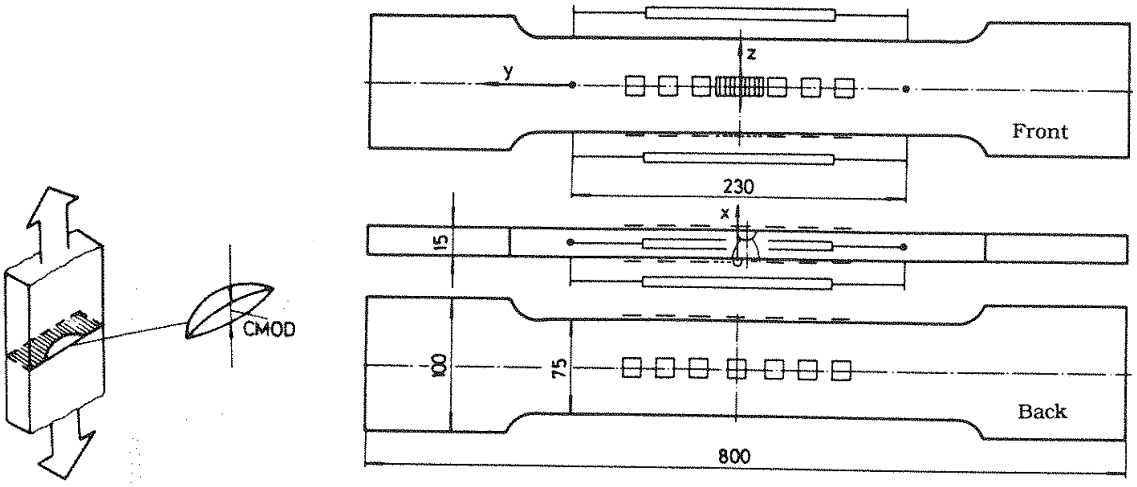

Figure 5-19. Preparation of samples for tensile panel test

5-4-3. Mechanical properties and chemical composition of materials

Under matched weldments are recommended for high strength low alloy steel (HSLA) with yield strength of above 700 MPa in order to avoid cold cracks. Tensile properties and chemical composition is given in Tab. 5-1 and 5-2, respectively.

Table 5-1.Mechanical properties of materials

Strength (MPa)	Base metal (BM)	Weld metal (WM)	Heat affected zone (HAZ)
Yield strength(σ_y)	750	718	734
Tensile strength(σ_{Ut})	820	791	800

Table 5-2.Chemical composition of materials

C	Si	Mn	P	S	Cr	Ni	Mo	V	Al
0.10	0.20	0.23	0.009	0.018	1.24	3.1	0.29	0.05	0.08

5-4-4. Crack driving force curves of BM, HAZ and WM

Crack driving forces are calculated for various values of crack depth ratio (d/h) for pressure vessels with the shell parameter equal to zero (λ=0). Crack driving force of cylindrical shell could be calculated using the model proposed by Ratwani, Erdogan and Irwin, [31], as shown in Fig. 5-20:

$$J^{\star} = \frac{JE}{4a\sigma_Y^2} \qquad (5\text{-}36)$$

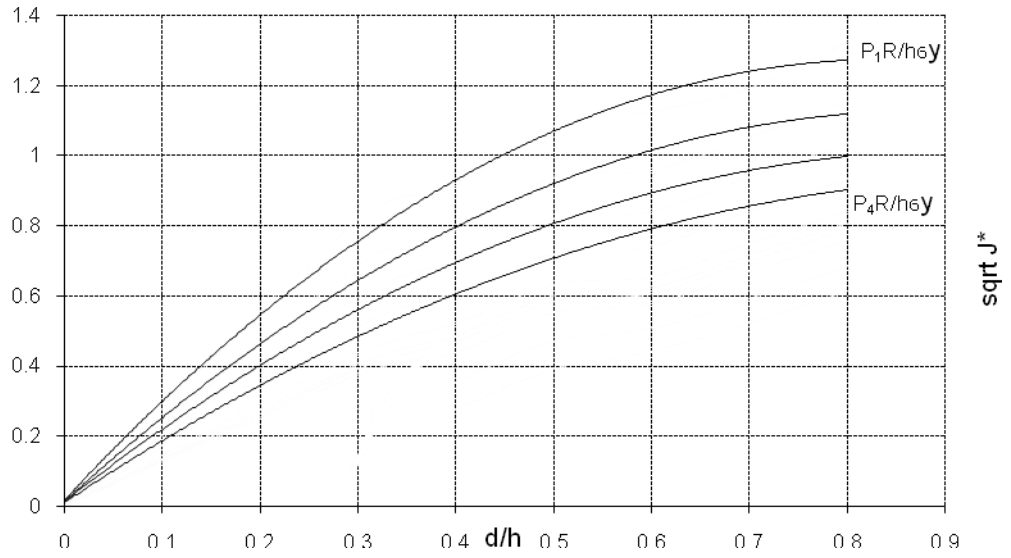

Figure 5-20. The CDF of the penstock model

One should notice that the crack driving force curves were determined for various values of stresses ratio ($PR/h\sigma_y$), in non-dimensional form, independent of material tensile properties.

5-4-5. The J-R curves of small and large surface flaw of BM, WM and HAZ

When the crack driving force equals or exceeds the fracture toughness of the material, the crack starts to grow, therefore the J-R curves for different components (BM , WM , HAZ) and different depth (SSF, LSF) were determined according to the previous method and got the following results, as indicated in figure 5-21.

The results of the procedure of J-R curves for large surface flaws as indicated in figure 5-21, the base metal showed higher resistance to propagation of the crack and heat affected zone which had lower resistance. The heterogeinity of microstructure in HAZ plays a main role in this behavior.

As indicated in figure 5-21, J-R curves for small surface flaw curve of weld metal showing lower resistance to the crack growth while the base metal with SSF shows higher resistance to the crack growth. This means the existing small surface flaw in the weld metal will grow faster than others and the leakage and failure is expected to happen in this location.

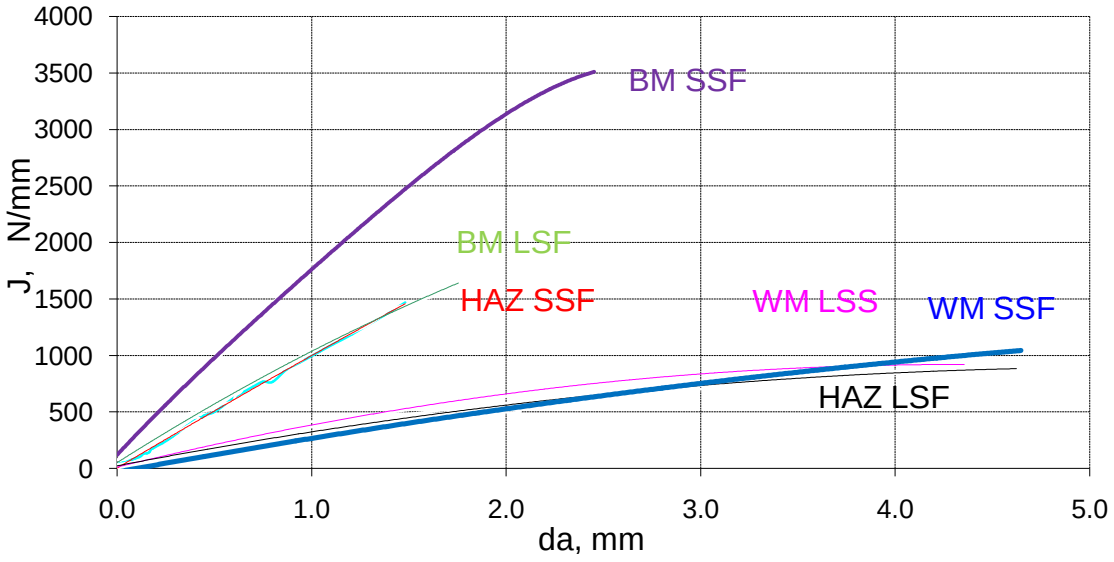

Figure 5-21. The J-R curves of WM, BM and HAZ (LSF, SSF)

5-4-6. Results of failure prediction of BM, WM and HAZ

The CDF curves, Fig. 5-20, are now plotted against J-R curves, Fig. 5-21, as shown in Figure 5-22, 5-23 and 5-24,for BM, WM and HAZ, respectively.

Figure 5-22 indicates that, for the measured length of surface crack with large surface flaw (depth of crack, d= 4.74 mm), the point of instability was reached at pressure 11.95 MPa, and for a small surface flaw (depth of crack, d = 2.38 mm), the point of instability reached a pressure of 15.77 MPa, and the crack will be stable up to: SSF (d/h) = 0.245 and da =1.54 mm; LSF (d/h) = 0.38 and da = 1.34 mm.

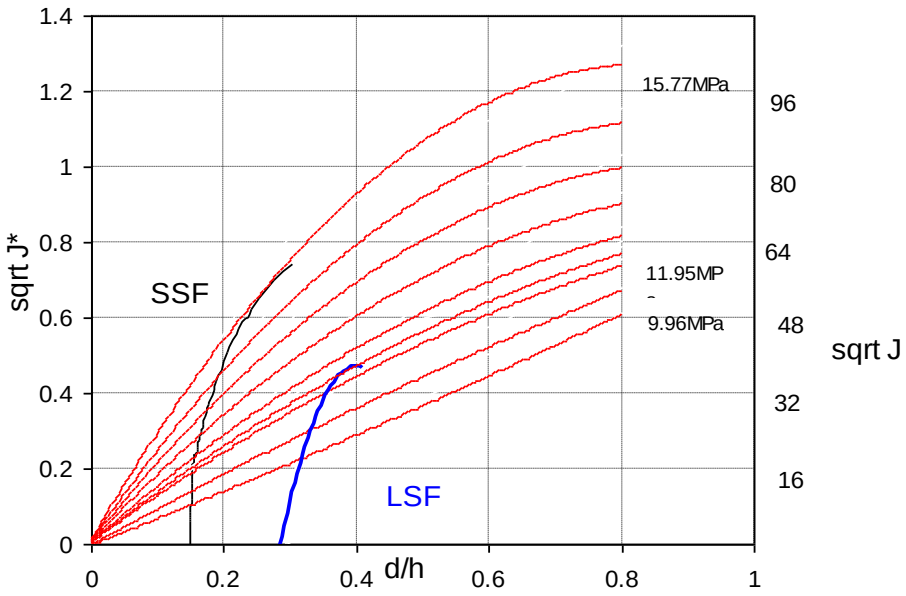

Figure 5-22. Determining the point of instability of BM of penstock

Figure 5-23 shows that, the point of instability of large surface flaw of weld metal reached a pressure of 11.16 MPa and crack growth will be stable up to a depth ratio of 0.46 and crack extension (da = 2.42 mm), while for a small surface flaw, the pressure of instability was 13.01 MPa and the crack will be stable up to a depth ratio of 0.31 and crack extension (da = 2.85 mm).

As indicated in figure 5-24, the point of instability of small surface flaw reached a pressure of 15.27 MPa and the crack will be stable up to a depth ratio of 0.23 and maximum stable crack extension was (da = 1.65 mm). For a large surface flaw the

pressure of instability was 10.23 MPa, and crack will be stable up to a depth ratio of 0.42 and crack extension (da = 1.56 mm).

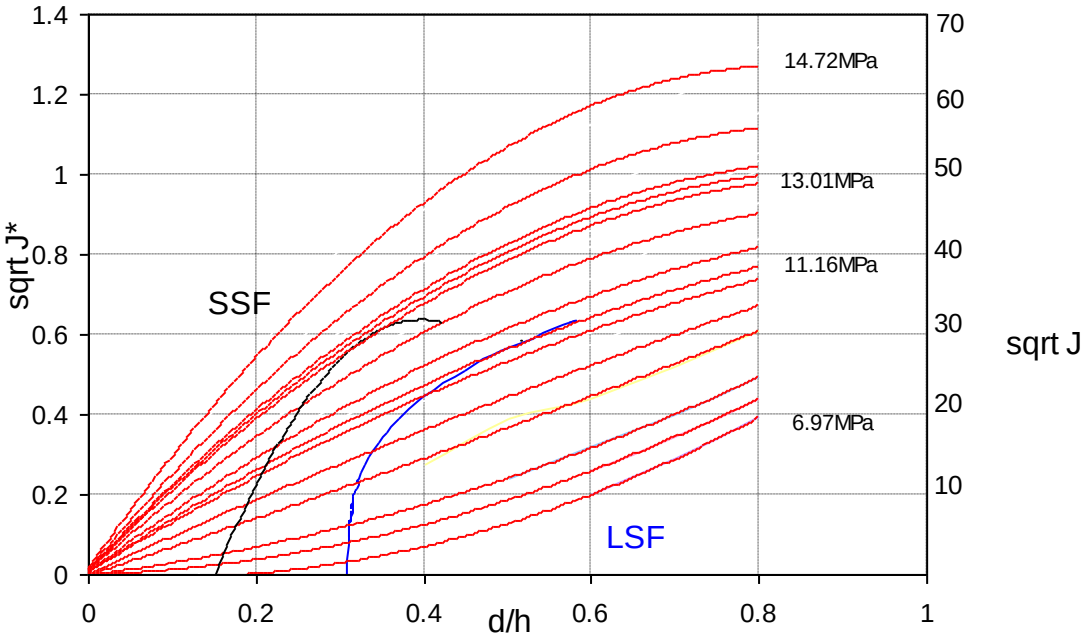

Figure 5-23. Determination the point of instability of WM of penstock

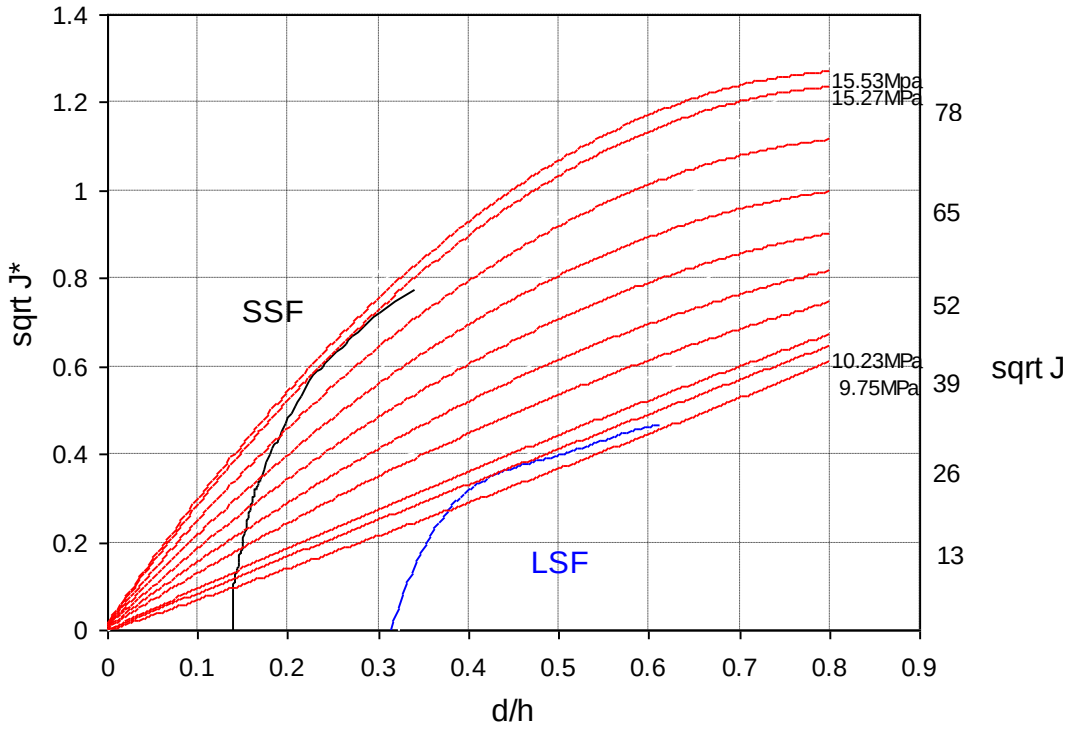

Figure 5-24. Determination the point of instability of HAZ of penstock

As it was shown in Ch. 5, the most critical case for full-scale model of pressure vessel is LSF in WM (Figure 5-23) with the point of instability when pressure reaches 11.16 MPa, and with stable crack growth up to a depth ratio of 0.46 and crack extension (da = 2.42 mm).

In order to investigate the effect of residual stresses and initial plastic deformation, a simple model was adopted. Namely, having in mind the eq. 5-36, and assuming that the yield stress is not only material property, but rather the stress at which the structure starts to yield, one can take into account both the residual stresses and initial plasticity simply by using the stress corresponding to experimentally obtained value or by using numerical values as obtained by the finite element method. Here, the experimental value has been used, σ_Y=500 MPa, which corresponds to the initiation of yielding in the full-scale model, as well as to the numerical simulations.

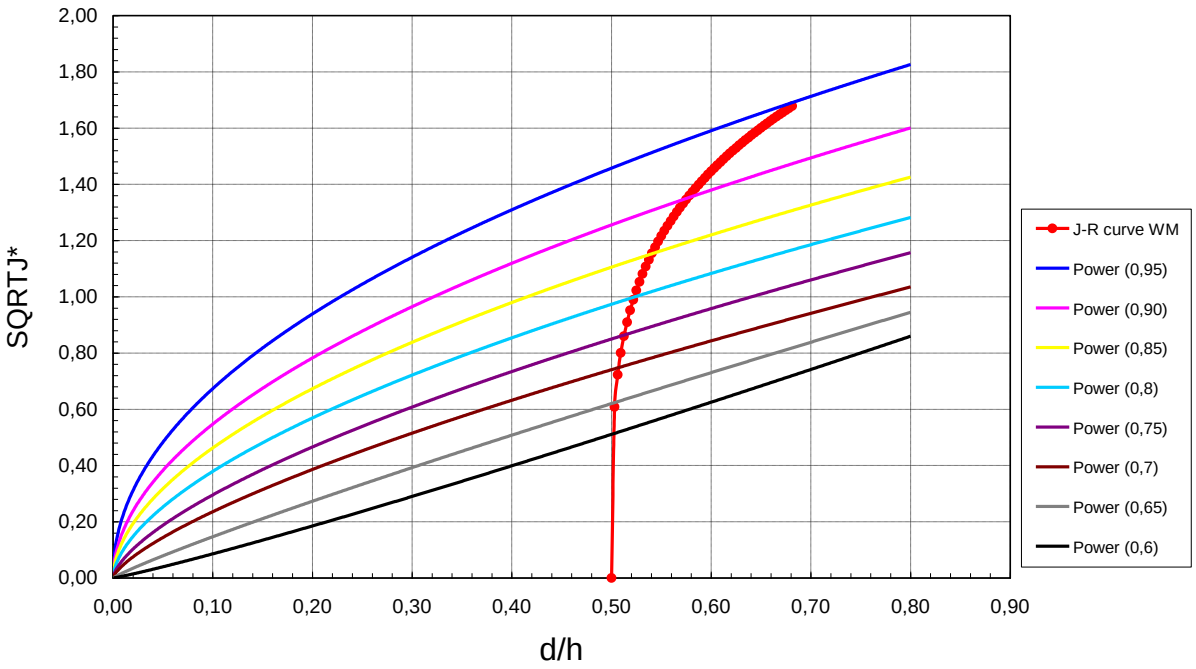

Figure 6-1. CDFs vs. J-R curve for LSF in WM

The crack driving forces obtained using this simple model are shown in Fig. 6 -1, together with the J-R curve for LSF in WM. As one can see, the critical pressure in this case is cca 9 MPa, which is significantly lower than 11.95 MPa, and in accordance with the experimental and numerical results.

Another important issue here is “strange” behavior of SG34, i.e. axial weld metal (the “loop”). As shown in Fig. 2-7, after usual elastic-plastic stress-strain behavior, there is unexpected “fast” growth of stress in plasticity with relatively small growth of strain, and then, during unloading, even more complicated to understand, release of strain which looks like being in plastic range. After extensive numerical investigation, as presented in Ch. 4, we offer the following explanation.

After initial elastic behavior, which was linear elastic, as usual, the weld metal started to deform plastically, as usual, but at the same time, there was a significant change in shape, i.e. large (nonlinear) elastic deformation due to local instability. It was this portion of total strain that has been released in the unloading process, producing “strange” stress-strain behavior and unusual “loop”, as observed experimentally. This is the consequence of mismatching and specific sequence of loading-unloading and has no significant meaning for the overall behavior and pressure vessel integrity. In this respect, only residual stresses and initial plastic deformation significantly affect overall stress-strain behavior and has to token into account when assessing pressure vessel integrity. The point here to be emphasized is that loading-unloading sequence used in this investigation actually followed so-called water proof testing, indicating problems which may appear.

7. CONCLUSIONS

Based on these results presented in this thesis, following general conclusions can be drawn:

- Water proof test is not always recommended, because it disregards possible stable growth of cracks, which might reach critical size for unstable growth, i.e. it does not prove that failure will not happen in future under the same conditions.
- Fracture mechanics, applied for structural integrity assessment, provides better approach for safety, because it can evaluate the significance of crack presence, predict its eventual growth and provide fitness-for-service as very important engineering tool. It can be used even for non-existing cracks in the design phase of pressure equipment.
- Engineers in charge for pressure equipment should learn how to live with cracks, rather than to assume that weldments are defect-free and provoke their growth.

Finite element analysis (ABAQUS software) for a full-scale model of penstock has been performed in order to simulate a hydrostatic test of the experimental model of the pressure vessel. Von Misses stress-strain distributions as calculated in ABAQUS, has been compared with stress-strain distribution of the ideal cylindrical model of a pressure vessel, and distribution obtained from strain gauge measurements in both loading – unloading regimes. For residual strength prediction and structural integrity assessment of penstock, the experiment investigation of specimens carried out by the notched tensile panel test of HSLA with under matched weld metal, to study the effect of the surface crack in each part of weld joint (BM, HAZ, WM) on fracture properties. This type of steel is recommended to avoid cold cracking, but due to heterogeneity of the microstructure and of mechanical properties of the weld joint, defects cannot be avoided completely. Therefore, adequate crack resistance properties are required in addition to tensile strength properties of the structure. Based on this study, the following specific conclusions are reached:

- The von Misses stresses distribution of the finite element model of penstock showed that, the highest stress level has been on the shorter side of the model (at a 5º angle), which represents the stress concentration region. This behavior is affected by the geometrical shape, which exerted more compression on that side in an axial direction.

- The upper segment of penstock on the shorter side represents the critical part of the structure. The experiment model and the finite element model have been shown the critical point of the penstock at that part (weld metal joint LS1SAW), where the plasticity started earlier than the other joint weld metal which has the same properties (yield strength).

- Good agreement between the strain gauge reading and finite element calculation, but higher levels of internal pressure are used for the finite element model in order to reach a closer level of stresses of the experimental test, due to the effect of residual stresses and geometrical imperfection.

- Using initial residual stresses of 40% of yield strength for weld metal joint in the finite element model reduces the level of internal pressure of the finite element model to reach a closer level of stresses of the experimental test. On the other hand, the stress distribution of finite element model with initial residual stresses was completely different compared to the finite element model without initial residual stresses. The highest stress levels have been in weld metal joints on the shorter sides of the model (LS1 SA, LS3 SAW, CM MAW).

- In general, the existence of cracks affects significantly behavior of welded joints. This influence is more pronounced for weld metal and heat affected zones compared to the base metal.

- Strange behavior of axial weld metal, i.e. stress-strain loop during loading-unloading sequence, has been explained by the local nonlinear elastic deformations, and has no significant effect on overall behavior and integrity of pressure vessel.

References

1. Nichols, R. (1984) The use of fracture mechanics as an engineering tool, in Adv In Fracture Research, ICF 6**,** New Delhi, vol. 6, p. 3717–3749
2. A. Sedmak, S. Sedmak, Lj. Milović, Pressure Equipment Integrity Assessment by Elastic-Plastic Fracture Mechanics Methods, published by DIVK, 2011
3. R. Jovičić, A. Sedmak, S. Sedmak, Lj. Milović, K. Jovičić, Leakage of an austenitic steel CO_2 storage tank, Structural Integrity and Life Vol. 12, No 2 (2012), pp. 105–108
4. A. Bređan, J.Kurai, European Pressure Equipment Directive (PED) and structural integrity, (in Serbian), Structural Integrity and Life, 3 (1): 31-42, 2003.
5. S. Petronic, Comparative Analysis of the Design Stress According to Different Regulations on Pressure Equipment, Structural Integrity and Life, Vol.12, No2, 2012, str. 143–148
6. T. Sedmak, E. Veg, Failure prevention of rotating equipment by vibrodiagnostics, Structural Integrity and Life, 12 (2), 2012 : 99-104.
7. P. Đorđević, S. Kirin, A. Sedmak, E. Džindo, „Risk analysis in Structural Integrity". Structural Integrity and Life, 11, 2(2011), pp. 135-138.
8. R. P. Reed, et al, Fitness-to-Service Criteria for Pipeline Girth Weld Quality, Final Report to the U.S.DOT, NBS, Boulder, USA, 1983
9. A. Mahdi, A.Sedmak, S. Kirin, B. Rakicevic, R. Bakic, Industrial safety of pressure vessels - structural integrity and risk assessment point of view, Hemijska Industrija, 2015
10. Somnath Chattopadhyaya, "Pressure Vessel Design and Pracise", Taylor & Francis Group, LLC, 2004
11. Abaqus, 2007 ABAQUS Users' Manuel, Hibbit, Karlson and Sorenson Inc., Pawtucket, RL
12. A. A. Griffith, " Phenomena of Rupture and Flow in Solids ", Philos. Trans. R. Soc. London. Ser. A221, 1920.

13. G. R. Irwin, “ Analysis of Stresses and Strains Near the end of Crack Transversing a Plate “, J. Appl. Mech. 24, 1957.

14. J. R. Rice, “A path Independent Integral and the Approximate Analysis of Strain Concentration by Notches and Cracks,” Journal of Applied Mechanics, 1968

15. C. E. Inglis,” Stress in a Plate Due to The Presence of Cracks and Sharo Corners”, Trans. Inst. Nav. Archit, London 55, 1913.

16. Anderson, T.L,” Fracture Mechanics: Fundamental and Application “, CRC Press, 2005

17. Irwin, G.R.,” Plastic Zone near a Crack and Fracture Toughness,” Sagamore Research Conference Proceeding, Vol. 4, 1961

18. Barenblatt, G. I., “The Mathematical Theory of Equilibrium Cracks in Brittle Fracture,” Advances in Applied Mechanics, Vol, VII, Academic Press, 1962

19. E. Orowan, “Energy Criteria of Fracture,” Weld. J. 34, 1955

20. A. A. Wells, “Unstable Crack Propagation in Metals: Cleavage and Fast Fracture,” Proceeding of the Crack Propagation Symposium, Vol 1, Cranfield, UK, 1961.

21. Burdekin, F. M. and Stone, “The Crack Opening Displacement Approach to Fracture Mechanics in Yielding Material,” Journal of Strain Analysis, Vol. 1, 1966

22. Hutchinson, J. W, “Singular Behavior at the End of Tensile Crack Tip in a Hardening Material,” Journal of the Mechanics and Physics of Solids, Vol. 16, 1968.

23. Rice, J. R. and Rosengren, G. F” Plane Strain Deformation near a Crack Tip in Power-Law Hardening Material,” Journal of the Mechanics and Physics of Solids, Vol. 16, 1968

24. C. F. Shih, “Relation between the J Integral and the Opening Displacement for Stationary end Extending Crack,” Journal of the Mechanics and Physics of Solids, 29(4), 1981

25. H. S. Lamba, “the J Integral Applied to Cyclic Loading,” Engineering Fracture Mechanics, 1975

26- J. R. Rice," Mechanics of Crack Tip Deformation and Extension by Fatigue," In ASTM, 415, 1967.

27- E399-90,"Standard Test Method for Plane Strain Fracture Toughness of Metallic Material," American Society for Testing and Materials, Philadelphia, PA, 1990 (Reapproved 1997).

28- BS 5447,"Methods of Testing for Plane Strain Fracture Toughness (K_{IC}) of Metallic Materials," British Standard Institution, London, 1974

29-E1820-01,"Standard Test Method for Measurement of Fracture Toughness," American Society for Testing and Materials, Philadelphia, 2001

30- BS 7448: Part 1," Fracture Mechanics Toughness Test, Part 1, Method for Determination of K_{IC}, critical CTOD and Critical J Values of Metallic Materials," British Standard Institution, London, 1991.

31- M. M Ratwani, F. Erdogan and G. P. Irwin," Fracture Propagation in Cylindrical Shell Containing an Initial Flaw," Lehigh University, Bethlehem, 1974

32. Radomir Jovičić, Mahdi Mohamed Ahmad Algool, Uroš Tatić, Olivera Popović, Uroš Lukić, Meri Burzić, Storage tank integrity assessment after the removal of weld cracks, Structural Integrity and Life, Vol. 14 (2014), 1, pp. 35-38

33. Ivica Čamagić, Zijah Burzić, Aleksandar Sedmak, Nemanja Vasić, Bogdan Ćirković, Mahdi Mohamed Ahmad Algool, Influence of mechanical properties and microstructural heterogeneity of welded joint constituents on tensile properties and fracture toughness at plane strain, Structural Integrity and Life, Vol. 14 (2014), 1, pp. 45-49

34. Algoul Mahdi, Aleksandar Sedmak, Blagoj Petrovski, Uros Tatić, Simon Sedmak, Andrijana Djurdjevic, Quality assurance of a large welded penstock manufacturing by means of full-scale model testing, Proceedings of the 2nd International Conference on manufacturing engineering & management - ICMEM 2012, Prešov 2012, pp. 107-108

Biography of the Author

Mahdi M. A. Algool was born on 7th of March 1972, in Libya, Libyan nationality. He finished his secondary school in Sirte, Libya. In 1997 he received his B. sc degree from Sirte University, faculty of mechanical engineering. In 2006, Mahdi received hisM.sc from Warsaw University of technology, faculty of production engineering. Since October 2010, he has been Ph.D. candidate at the University of Belgrade, faculty of mechanical engineering.

In the period 2006-2010, he worked as an assistant lecturer at the Sirte University, faculty of mechanical engineering and he taught some subjects: workshop, strength of materials and laboratory of fluid mechanics.

Прилог 1.

ИЗЈАВА О АУТОРСТВУ

Потписани-а Mahdi M. A. Algool

број уписа Д 69/10

Изјављујем

да је докторска дисертација под насловом

Initial plastic deformation and residual stress influencing the behavior of welding joint in the presence of a crack

Утицај иницијалне пластичне деформације и заосталих напона на понашање завареног споја у присуству прслине

Апсорпциона машина погоњена сунчевом енергијом за климатизацију пословне зграде у медитеранским климатским условима

- резултат сопственог истраживачког рада,
- да предложена дисертација у целини ни у деловима није била предложена за добијање било које дипломе према студијским програмима других високошколских установа,
- да су резултати коректно наведени и
- да нисам кршио/ла ауторска права и користио интелектуалну својину других лица.

Потпис докторанда

У Београду, . .2015

_____

Прилог 2.

ИЗЈАВА О ИСТОВЕТНОСТИ ШТАМПАНЕ И ЕЛЕКТРОНСКЕ ВЕРЗИЈЕ ДОКТОРСКОГ РАДА

Име и презиме аутора Mahdi M. A. Algool

Број уписа Д 69/10

Студијски програм _____

Наслов рада Initial plastic deformation and residual stress influencing the behavior of welding joint in the presence of a crack

Утицај иницијалне пластичне деформације и заосталих напона на понашање завареног споја у присуству прслине

Ментор Проф. др. Александар Седмак

Потписани Mahdi M. A. Algool

изјављујем да је штампана верзија мог докторског рада истоветна електронској верзији коју сам предао/ла за објављивање на порталу **Дигиталног репозиторијума Универзитета у Београду.**

Дозвољавам да се објаве моји лични подаци везани за добијање академског звања доктора наука, као што су име и презиме, година и место рођења и датум одбране рада.

Ови лични подаци могу се објавити на мрежним страницама дигиталне библиотеке, у електронском каталогу и у публикацијама Универзитета у Београду.

Потпис докторанда

У Београду, .2015.

_____

Прилог 3.

ИЗЈАВА О КОРИШЋЕЊУ

Овлашћујем Универзитетску библиотеку „Светозар Марковић“ да у Дигитални репозиторијум Универзитета у Београду унесе моју докторску дисертацију под насловом:

Initial plastic deformation and residual stress influencing the behavior of welding joint in the presence of a crack

Утицај иницијалне пластичне деформације и заосталих напона на понашање завареног споја у присуству прслине

која је моје ауторско дело.

Дисертацију са свим прилозима предао/ла сам у електронском формату погодном за трајно архивирање.

Моју докторску дисертацију похрањену у Дигитални репозиторијум Универзитета у Београду могу да користе сви који поштују одредбе садржане у одабраном типу лиценце Креативне заједнице (Creative Commons) за коју сам се одлучио/ла.

1. Ауторство
2. Ауторство - некомерцијално
3. Ауторство – некомерцијално – без прераде
4. Ауторство – некомерцијално – делити под истим условима
5. Ауторство – без прераде
6. Ауторство – делити под истим условима

(Молимо да заокружите само једну од шест понуђених лиценци, кратак опис лиценци дат је на полеђини листа).

Потпис докторанда

У Београду 2015.

_____

1. Ауторство - Дозвољавате умножавање, дистрибуцију и јавно саопштавање дела, и прераде, ако се наведе име аутора на начин одређен од стране аутора или даваоца лиценце, чак и у комерцијалне сврхе. Ово је најслободнија од свих лиценци.

2. Ауторство – некомерцијално. Дозвољавате умножавање, дистрибуцију и јавно саопштавање дела, и прераде, ако се наведе име аутора на начин одређен од стране аутора или даваоца лиценце. Ова лиценца не дозвољава комерцијалну употребу дела.

3. Ауторство - некомерцијално – без прераде. Дозвољавате умножавање, дистрибуцију и јавно саопштавање дела, без промена, преобликовања или употребе дела у свом делу, ако се наведе име аутора на начин одређен од стране аутора или даваоца лиценце. Ова лиценца не дозвољава комерцијалну употребу дела. У односу на све остале лиценце, овом лиценцом се ограничава највећи обим права коришћења дела.

4. Ауторство - некомерцијално – делити под истим условима. Дозвољавате умножавање, дистрибуцију и јавно саопштавање дела, и прераде, ако се наведе име аутора на начин одређен од стране аутора или даваоца лиценце и ако се прерада дистрибуира под истом или сличном лиценцом. Ова лиценца не дозвољава комерцијалну употребу дела и прерада.

5. Ауторство – без прераде. Дозвољавате умножавање, дистрибуцију и јавно саопштавање дела, без промена, преобликовања или употребе дела у свом делу, ако се наведе име аутора на начин одређен од стране аутора или даваоца лиценце. Ова лиценца дозвољава комерцијалну употребу дела.

6. Ауторство - делити под истим условима. Дозвољавате умножавање, дистрибуцију и јавно саопштавање дела, и прераде, ако се наведе име аутора на начин одређен од стране аутора или даваоца лиценце и ако се прерада дистрибуира под истом или сличном лиценцом. Ова лиценца дозвољава комерцијалну употребу дела и прерада. Слична је софтверским лиценцама, односно лиценцама отвореног кода.